Title
Mechatronic Considerations on the Development of an Upper Limb Exoskeleton for Rhesus Macaques

Author
Lu, Junkai

Publication Date
2016

Peer reviewed|Thesis/dissertation

Mechatronic Considerations on the Development of an Upper Limb Exoskeleton for Rhesus Macaques

by

Junkai Lu

A dissertation submitted in partial satisfaction of the

requirements for the degree of

Doctor of Philosophy

in

Engineering - Mechanical Engineering

in the

Graduate Division

of the

University of California, Berkeley

Committee in charge:

Professor Masayoshi Tomizuka, Chair
Professor J. Karl Hedrick
Professor Claire Tomlin
Professor Jose M. Carmena

Spring 2016

Mechatronic Considerations on the Development of an Upper Limb Exoskeleton for Rhesus Macaques

Abstract

Mechatronic Considerations on the Development of an Upper Limb Exoskeleton for Rhesus Macaques

by

Junkai Lu

Doctor of Philosophy in Engineering - Mechanical Engineering

University of California, Berkeley

Professor Masayoshi Tomizuka, Chair

Integrating an exoskeleton as the external apparatus for a brain-machine interface has the advantage of providing multiple contact points to determine body segment postures and allowing control to and feedback from each joint. Most current brain-machine interface studies use non-human primates, for example rhesus macaques (*Macaca mulatta*), as the research subjects. In order to develop an upper limb exoskeleton for macaques which can provide both data acquisition and motion actuation, this dissertation investigates the mechatronic considerations of developing such a device, including 1) the kinematic modeling and structural design, and 2) the actuator design and control.

An exoskeleton is a wearable robot, and is supposed to be attached to the user's body segments. Thus the kinematic structure needs to match the macaque's upper limb as closely as possible, which requires the exoskeleton to be compact and singularity free in workspace, as well as have biomorphic nature joints and firm attachments. In order to provide sufficient output torque and guarantee the user's safety, the actuators of the exoskeleton should be backdrivable, of high power-to-weight ratio, and capable of executing compliant actuation algorithms.

Based on the above design requirements, this dissertation presents the development process of an upper limb exoskeleton for macaques from kinematic modeling and analysis, passive exoskeleton prototyping and animal training, compliant actuator design and control, to completion of an actuated exoskeleton and system integration with a brain-machine interface. First an upper limb exoskeleton model is proposed with a redundant shoulder joint to achieve improved manipulability than conventional designs. The advantageous features of the proposed exoskeleton model are demonstrated by a series of kinematic analysis. Then a passive upper limb exoskeleton is fabricated for kinematic model validation, motion characterization and animal training purposes, and its effectiveness is demonstrated by the animal tests. In order to obtain a compact, powerful, backdrivable and torque-reflecting actuator for the actuated exoskeleton, a cable-driven series elastic actuator is designed, and an interactive impedance control algorithm is proposed and experimentally validated. On top

of the development of the passive exoskeleton and the impedance-controlled actuator, an actuated multi-degree of freedom upper limb exoskeleton is developed and integrated with a brain-machine interface, and the effectiveness of the proposed exoskeleton system is finally supported by pilot animal tests.

To my parents.

Contents

List of Figures

List of Tables

Nomenclature

2D	Two-Dimensional
3D	Three-Dimensional
ADL	Activities of Daily Living
BMI	Brain-Machine Interface
DH	Denavit-Hartenberg
DOB	Disturbance Observer
DOF	Degree of Freedom
NHP	Non-Human Primate
PD	Proportional-Derivative
PID	Proportional-Integral-Derivative
RMS	Root-Mean-Square
ROM	Range of Motion
SEA	Series Elastic Actuator

Acknowledgments

First of all, I would like to express my earnest gratitude and sincere respect to my research advisor, Professor Masayoshi Tomizuka, for the insightful instructions, persistent encouragement, and generous support he has offered to me, which has tremendously helped me to broaden my horizon and enhanced my ability to work independently. Your rigorous academic attitude, genuine enthusiasm on work, and optimistic character also have greatly influenced me, and I believe they will definitely benefit me for my entire life.

I would like to express my deepest love to my parents Min Lu and Lihua Su. You are always behind me and have been a constant source of unconditioned love and support during the many years of my education.

I am also very grateful to Professor J. Karl Hedrick, Professor Claire Tomlin, and Professor Jose M. Carmena for your willingness to serve as my Ph.D. dissertation committee and providing valuable suggestions which greatly helps to improve the quality of this dissertation.

Among all my collaborating team members, I would like to give my special thanks to Kevin Haninger. Kevin is an awesome teammate, and I am very impressed by his rigorous, energetic, and diligent personality. I enjoyed a lot working with him brainstorming together and sharing ideas. I also would like to give my special thanks to Dr. Wenjie Chen, without whose help, instructions and encouragement I cannot make so much progress in this research. I am also grateful to Dr. Joonbum Bae for his early effort on this project as well as his sincere encouragement to me. I am honored that I can work with Professor Jose M. Carmena and Professor Claire J. Tomlin and their teams, from whom I benefited a lot. I enjoyed working with Dr. Suraj Gowda, Dr. Young Hwan Chang, Mo Chen, and Dr. Simon Overduin, and I will always remember the countless discussions and experiments we did together. I also would like to thank Dennis Lee, Mick Franssen, Jesse Lopez and Scott McCormick from the Mechanical Engineering Department Student Machine Shop, without whose assistance and suggestion, we could not have completed all the hardware fabrication. My thanks also go to the assistance of the following undergraduates who ever participated in this project: Abishek Akella, Nolan Wagener, Sam Cohen, Piyush Prakash, and Kate Schweidel.

I am lucky to be able to join the Mechanical Systems Control (MSC) Laboratory, and work with so many talented fellows from all around the world. I would like to thank my peers Chung-Yen Lin, Minghui Zheng, and Chen-Yu Chan for their sharing my happiness as well as my hard times. I am also thankful to my upperclassman Wenlong Zhang for his generous help, encouragement and support over the years. I would also like to thank all the other current and previous members at the MSC Lab: Evan Chang-Siu, Sanggyum Kim, Pedro Reynoso, Michael Chan, Xu Chen, Kan Kanjanapas, Chi-Shen Tsai, Cong Wang, Yizhou Wang, Raechel Tan, Omar Abdul-hadi, Robert Matthew, Changliu Liu, Xiaowen Yu, Shuyang Li, Hsien-Chung Lin, Te Tang, Dennis Wai, Yu Zhao, Shiying Zhou, Daisuke Kaneishi, Cheng Peng, Liting Sun, Wei Zhan, Jianyu Chen, Yongxiang Fan, Kiwoo Shin, Zining Wang, and the others.

My time at Berkeley would not have been so enjoyable without all the great friends I have made here. Thank you Shuo-Yiin Chang, Chi-Pang Lam, Chang Liu, Xuance Zhou,

Yong Liang, Minsong Wei, Yow-Gwo and many others for your company and support. I will always treasure the wonderful moments we spent together.

This research was supported by the National Science Foundation (NSF) under Grant EFRI-M3C 1137267. I also would like to acknowledge National Instruments Corporation (NI) for the generous support of my research.

Chapter 1

Introduction

1.1 Background

Humans have long held a fascination for inventing a piece of technology that would let people control a device simply using their mind. To implement such a system as shown in Fig. 1.1, a neural interface needs to be implanted on the motor cortex to record the firing of neurons, and then input the neural signal to a computer program which is called a decoder. This decoder will translate the brain activity into a small number of output signals to control the external devices. In order to give the users not only the control of the device but also the ability to feel it, tactile sensors can also be installed on the device to send the sensing information back to the brain. This entire system is called a brain-machine interface (BMI), which can provide means to enable the communication between the brain and the outside world [10].

BMIs are often directed at assisting, augmenting, or repairing human cognitive or sensory-motor functions, specifically, for paralysis patients. Since the introduction of BMI, researchers around the world have been putting tremendous efforts into finding ways to enable the paralyzed people to move a prosthetic device with their mind. Researchers at the University of Pittsburgh have realized an able-bodied monkey to control a robotic arm by decoding the monkey's neural signals [83], and one study published in [26] has demonstrated that people suffering from brainstem stroke can also control a robotic arm to perform three-dimensional (3D) reach and grasp movements through a BMI system. These research breakthroughs have also helped promote a new paradigm of human-robot interaction. And the BMI system may also become a promising rehabilitation solution for people who suffer from loss or difficulty of mobility.

In terms of providing physical therapy training or assistive power to the upper limb rehabilitation, most of the existing therapy robots are either end-effector-based or exoskeleton devices [59]. Since an end-effector-based robot generally interacts with patients through only one point, it cannot fully determine the patient's arm posture or the interaction torques at each joint. Although a wearable exoskeleton has more complicated mechanical structures

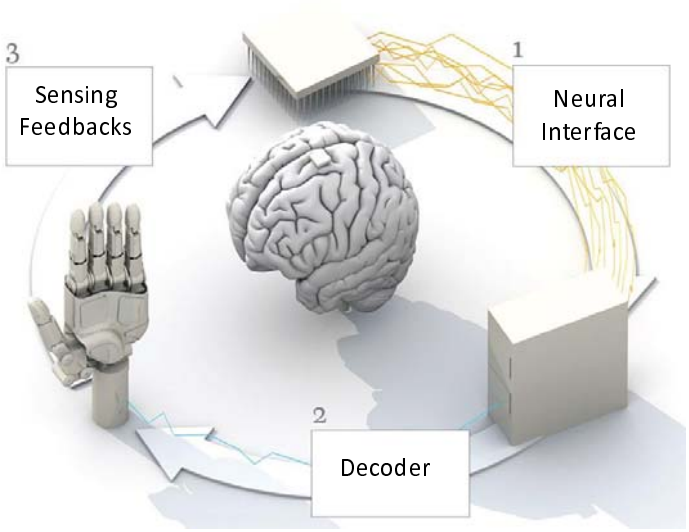

Figure 1.1: General structure of an invasive brain-machine interface system [15].

and system dynamics, the multiple contact points with the user's body allow control to and feedback from each joint individually.

Specifically, an exoskeleton solution can be useful to help restore the mobility of the affected upper limbs by allowing the shared control of the limb between the exoskeleton controller and the patient's residual motor control abilities. For paralyzed patients with some residual sensory abilities, it would be highly desirable for the assistive device to give them somatosensory and proprioceptive feedback that is consistent with their limb movements, which would be easy to achieve with an exoskeleton device, but not with an end-effector based robot. Even for completely paralyzed patients, an exoskeleton may offer better control than an end-effector based robot given that the patient should be better able to "embed" the movements of an exoskeleton into the patients' body schema since the device should follow their desired movements more precisely. And there are other motor disorders beyond the above yielding paralysis for which exoskeletons would be superior to end-effector based robots. In dystonia, for instance (which often co-occurs with Parkinson's disease), patients are typically able to initiate but not to complete their movements. In such situations, an exoskeleton is able to track their initial movement and then execute the remainder of the motion after decoding the desired goal (not from neural activity but just from the initial movement). Thus, an exoskeleton as an apparatus controlled by the BMI may more closely match natural motion, which may allow better study of the neural control of movement.

Based on the above discussions, this collaborating research effort at UC Berkeley exploring the integration of the BMI and the exoskeleton system has the potential to promote people's understanding of fundamental principles in the neural control of movement in scenarios involving physical interactions with the world, as well as to motivate a new generation

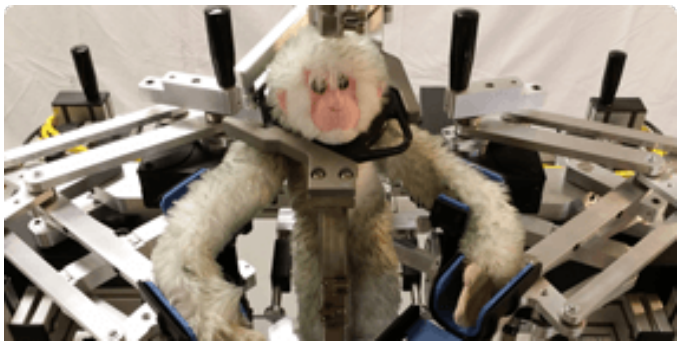

Figure 1.2: KINARM for non-human primates [30].

of rehabilitation or power augmentation exoskeleton systems. This project proposed an invasive BMI system with rhesus macaques (*Macaca mulatta*) as the study subjects, and the exoskeleton device involved provides both kinematic motion data acquisition and motion actuation.

1.2 Challenges and the Cutting Edge

Fig. 1.2 shows the well-known KINARM exoskeleton for upper limb motion sensing and actuation. By now the KINARM is the only upper limb exoskeleton that can be used by non-human primates (NHP) for BMI studies. It has five links, and two motors are installed on top of the frame to provide angular position of the joints and apply torques either to the shoulder or elbow, or both. The KINARM joints are designed to align with the NHP's shoulder and elbow, and allows the NHP to make arm motions in the horizontal plane. Thus it can be regarded as a two degrees of freedom (DOF) device which only allows movement in a two-dimensional (2D) task space. More details of this apparatus can be found in [78]. KINARM has been commercialized by BKIN Technologies, and the price is high.

One other exoskeleton-like device designed for NHPs is the lower limb exoskeleton developed by Dr. Nicolelis and his colleagues at Duke University, which is shown in Fig. 1.3. Its links are made of low-cost metal bars, and the motion is pneumatically powered. This NHP lower limb exoskeleton is also controlled by motion commands decoded from neural signals from the macaque's motor cortex.

Compared with the exoskeletons designed for NHPs, the exoskeleton systems for humans have been much more widely investigated in applications of power augmentation and rehabilitation. Although their target functions and design requirements are different from what we would like to achieve, they can still serve as pilot examples to investigate. The development of an exoskeleton consists of the kinematic structural design and the actuation system design. Next, the state of the art of human upper limb exoskeleton design and the motion actuation for subject-robot interaction will be discussed in this section.

Figure 1.3: Lower limb exoskeleton for non-human primates [31].

1.2.1 Kinematic Modeling and Structural Design

There are many design difficulties for developing an appropriate mechanism of an upper limb exoskeleton. Most of the difficulties result from the anatomy of the upper limb, especially from the shoulder complex, one of the most anatomically complicated areas in the human body, whose center of rotation is changing with its motions [21]. Specifically, the elevational rotation movement of the humerus can also cause the scapular to move, and this joint movement is called *scapulohumeral rhythm* [44]. Next, we will give a brief explanation about this phenomenon.

It can be noticed in Fig. 1.4 that the shoulder complex actually consists of four joints that function in a precise and coordinated manner: the sternoclavicular (SC) joint, the acromioclavicular (AC) joint, the glenohumeral (GH) joint, and the scapulothoracic (ST) joint [64]. Therefore, the shoulder complex is a highly-coupled mechanism of great complexity due to the fact that each of the four joints also possesses multiple DOFs (refer to [86] for more information).

A non-redundant 5-DOF mathematical model of the shoulder complex is introduced in [87], including three rotational DOFs (correspond to abduction/adduction, flexion/extension, and internal/external rotation movement) and two translational DOFs (correspond to elevation/depression, and protraction/retraction motion), with the thorax as the fixed base, as shown in Fig. 1.5. And it is exactly the two translational DOFs that cause the position

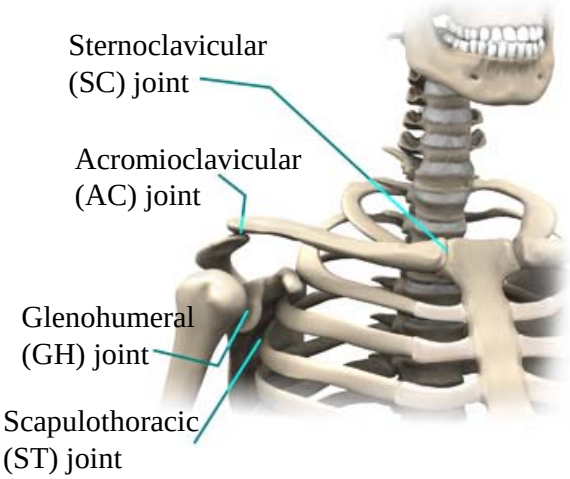

Figure 1.4: Joints located at the shoulder complex [32].

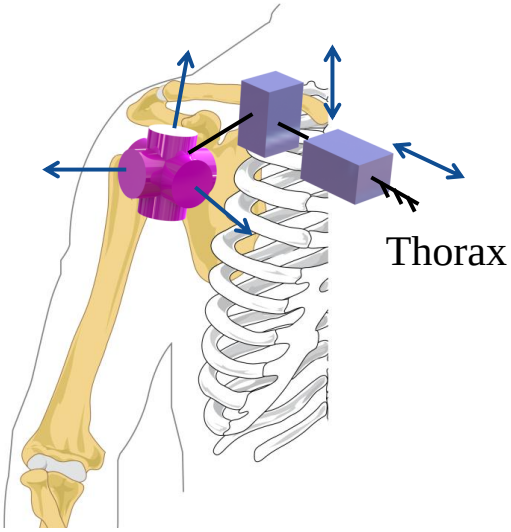

Figure 1.5: Non-redundant 5-DOF shoulder complex model.

change of the center of the GH joint.

Anatomical Joint and Exoskeleton Joint Alignment

Since the exoskeleton will be directly attached to the user's upper limb, if the motion is generated by the exoskeleton (i.e., user's limb moves passively, which is most of the cases in upper limb rehabilitation application), a shoulder complex design which has a shoulder joint center with translational DOFs would be of great importance. More generally speaking,

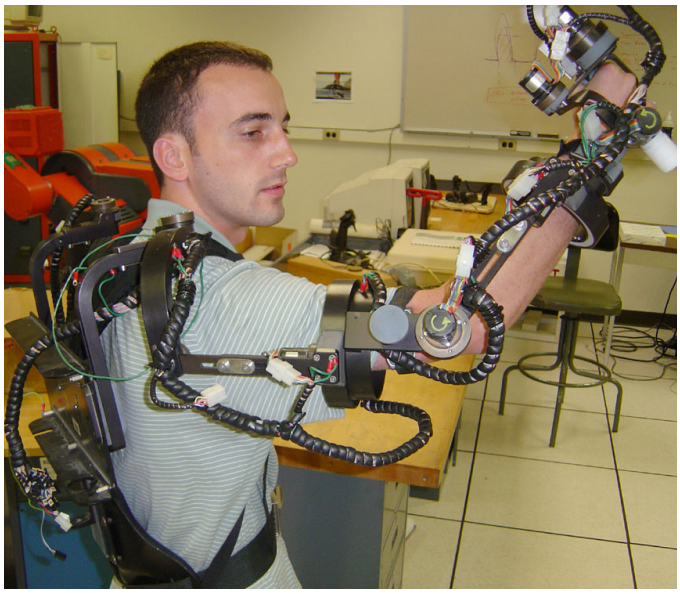

Figure 1.6: MGA exoskeleton proposed in [9].

this can be classified as the alignment problem between the user's anatomical joint and the mechanical joint of the exoskeleton's. If the exoskeleton axes cannot coincide with the user's anatomical rotation axes, the user's range of motion (ROM) will be reduced, which will also cause discomfort to the users [41].

The importance of the scapulohumeral rhythm in designing an upper limb exoskeletons was first emphasized in [7], and a passive exoskeleton was designed with two DOFs at the scapulothoracic joint dealing with this issue. Another design that has incorporated the scapulothoracic joint motion is the MGA exoskeleton shown in Fig. 1.6 [9], which allows for active adjustment to scapula rotation by using an extra actuated revolute joint in series with three actuators to form a spherical joint.

ARMin I [55], II [56], and III [58] are a series of well-known designs of rehabilitation-oriented exoskeletons (shown in Fig. 1.7). The shoulder complex of ARMin I just uses a 3-DOF spherical joint model, which cannot impose ergonomic movements to the user; ARMin II manages to come up with a design that has an extra vertical translational DOF to the shoulder joint corresponding to shoulder elevation/depression movement, which accordingly increases system kinematic complexity; ARMin III features its design of achieving the ergonomic movement by a circular shoulder joint motion, which has simplified system structure, but consequently reduced mechanism's ergonomy compared with ARMin II.

MEDARM [4] is a rehabilitation exoskeleton 5 DOFs at the shoulder complex composed of two at the sternoclavicular joint and three at the glenohumeral joint (shown later in Fig. 1.11). In particular, the two DOFs mimicking the sternoclavicular joint is actuated and can assist elevation/depression and protraction/retraction of the shoulder girdle. However,

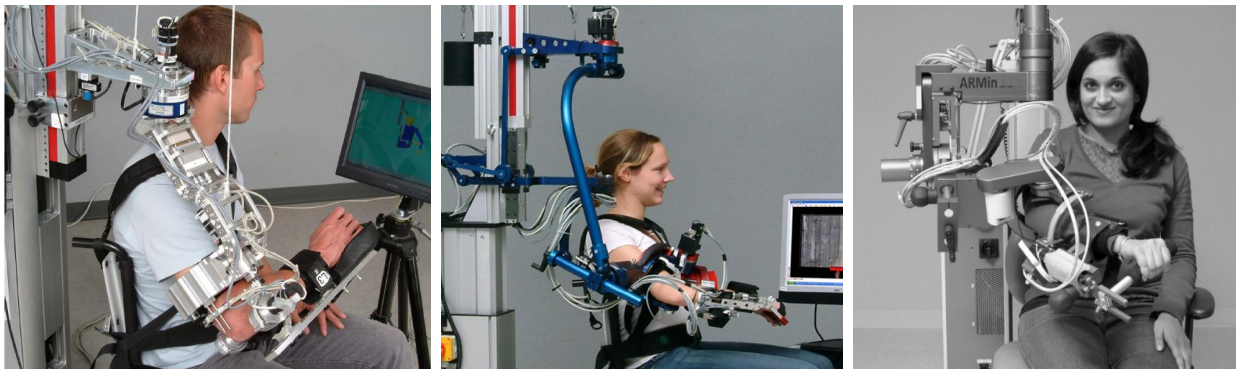

(a) ARMin I (b) ARMin II (c) ARMin III

Figure 1.7: Three generations of the ARMin exoskeletons.

in addition to its complexity, the design suffers from joint misalignment since the shoulder girdle mechanism approximates the path of the center of the glenohumeral joint as a circle at the sternoclavicular joint [18].

IntelliArm [63] is an exoskeleton design with seven actuated and two passive DOFs. In order to address the alignment issue of the shoulder center, two passive and one active DOFs are assigned at the shoulder complex, among which the two passive joints are implemented using linear slides, and the elevation/depression movement of the shoulder is tracked by a linear motor. This design allows for the ergonomic movements of the shoulder, in spite of lacking shoulder protraction/retraction movement, but with higher system complexity due to its possession of nine DOFs.

Another design with six DOFs at the shoulder complex is proposed in [41]. Thanks to its novel arrangement of the sequence of joints, this design enjoys the ability of providing both elevation/depression and protraction/retraction movement of the shoulder, and also manages to have increased the workspace of the exoskeleton. However, since five DOFs of the six are motorized, system complexity is also greatly increased.

The design in [18] proposes a 7-DOF exoskeleton with six active joints and one passive joint. This design features a 3-DOF self-aligning module for adjusting the alignment of human joint axes and the device axes for exoskeletons, which is a planar parallel mechanism with high position accuracy and large range of rotations (shown in Fig. 1.8). This module is quite generic, and can also be applied to types of exoskeleton designs, even to the designs that already exist.

Kinematic Singularity

Another design difficulty of the shoulder joint that is not discussed as widely as the mechanism alignment problem is the *kinematic singularity* issue.

The physical meaning of a kinematic singularity refers to the configurations in which

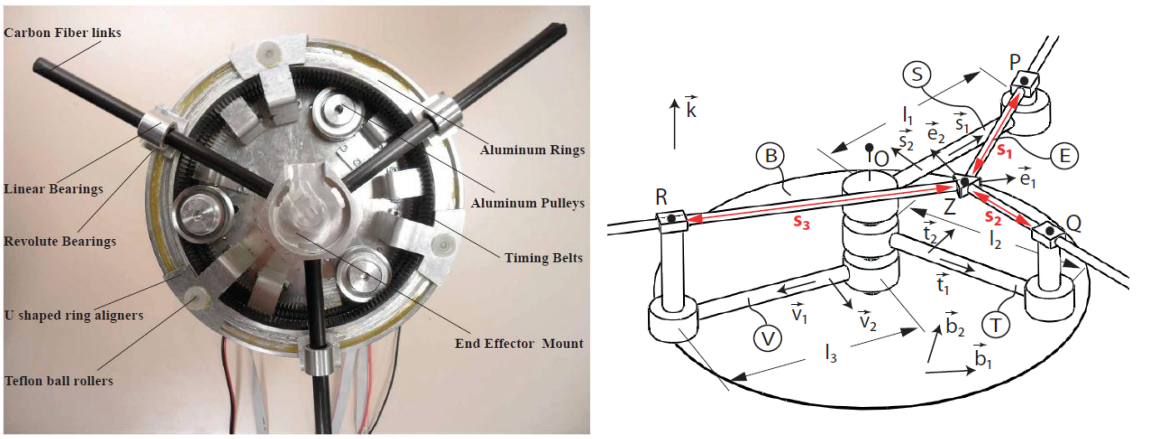

(a) Hardware design of the self-aligning joint (b) Schematic model of the self-aligning joint

Figure 1.8: The 3-DOF self-aligning module of [18].

there is a change in the expected or typical number of instantaneous degrees of freedom [17]. When singularity occurs, at least one DOF of motion is lost, and the mechanism cannot move arbitrarily, which is highly undesirable for a motion tracking system. Meanwhile, in the vicinity of a singularity for a motorized design, small desired velocities in the task space will require very large joint motions if the task space velocities have components along the degenerated directions. These large joint motions may damage the motors or even result in severe injuries to the user.

Apart from the translational DOFs at the shoulder complex, the shoulder can be basically modeled by a ball-and-socket joint (or spherical joint), which consists of three rotational DOFs. Therefore, it is intuitive to use three serial revolute single joints to mimic the shoulder joint. However, for any mechanism that uses a series of revolute joints to mimic the ball-and-socket joint, singularities always exist. Fig. 1.9 shows the singular configuration of a three serial joint model where Axis 1 and Axis 3 are collinear, making this mechanism lose the rotational DOF about the defined z_0 axis.

In spite of the singularity problem, engineers prefer utilizing the "canonical" form of a triad model to characterize the shoulder joint for system simplicity, as shown in Fig. 1.10. The "canonical" here means that the three axes are perpendicular to each other at its home posture, and the axis directions are in accordance with those of the world coordinate system. It can be noticed that no matter how this mechanism reach the posture with entire arm pointing to the user's front direction, the axis of Joint 1 will always be collinear with that of Joint 3, and the singularity occurs. The exoskeletons proposed in [33, 52, 72, 82] all use this model with their should joint designs.

To reduce the occurrence of singularities, some researchers revised the canonical triad model with different approaches based on different reasons and assumptions. Typical designs that have taken this issue into consideration are MEDARM [4], (CADEN)-7 [65], and SAM

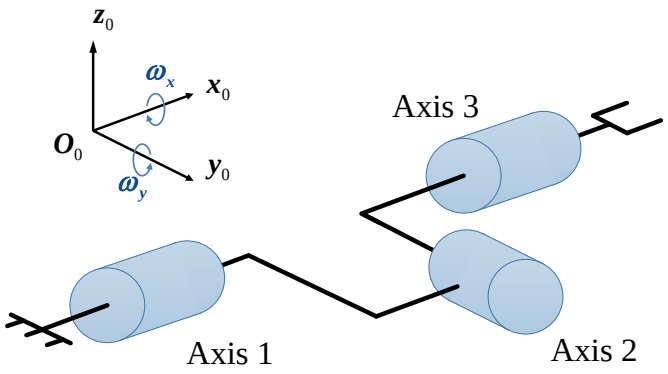

Figure 1.9: Singular configuration of a three serial joint ball-and-socket model.

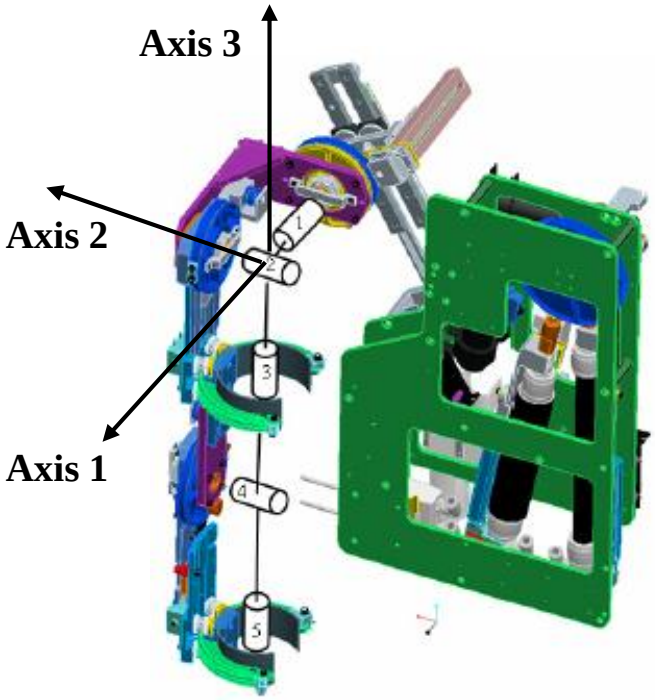

Figure 1.10: The shoulder model of IKO [52].

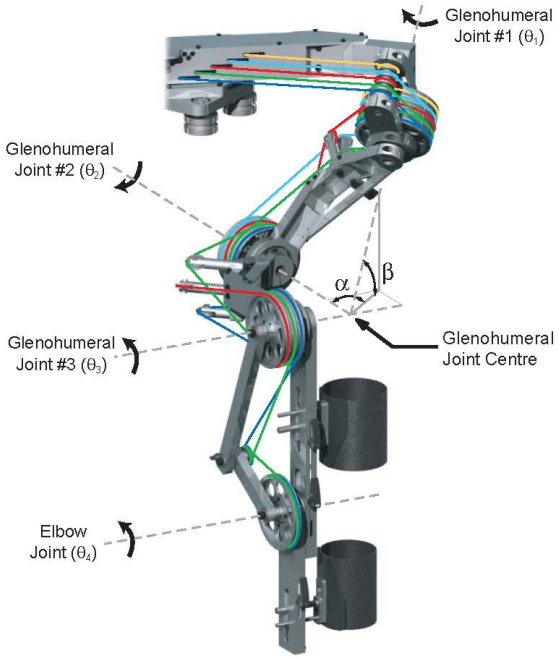

Figure 1.11: Relationship illustration of the shoulder axes of the MEDARM model [4].

[45].

MEDARM deals with the singularity issue using an optimization-based approach. The relative angle between its first axis and the second axis is obtained by maximizing a metric (the box product of the unit direction vectors of three axes) which the authors utilize to evaluate mechanism's manipulating ability, as well as avoiding configurations where there exist collisions between the exoskeleton and the user body. Using the parameters they proposed, the authors claim there is no singularities in their prescribed workspace.

(CADEN)-7 uses a strategy of assigning the system's singular posture to a direction that is rarely (in the sense of statistics, which can be found in [66]) reached by people in their activities of daily living (ADL), or anthropometrically hard to reach, as shown in Fig. 1.12. In this way, the authors claim that the majority of the exoskeleton workspace is free of singularities [65]. Note, unlike MEDARM, the first joint axis of (CADEN)-7 and its second joint axis are still perpendicular to each other.

SAM is designed in a way that is more like between MEDARM and (CADEN)-7. Similar to (CADEN)-7, the first joint axis is designed to have two successive rotation angles about two task space reference coordinate axes, which results in its singular direction being at the frontier of the workspace. However, the design principle is based on analyzing the system's manipulating ability, which is similar to what the authors have done for MEDARM, but with the metric being the ratio of the extreme singular values of the Jacobian matrix (isotropic index).

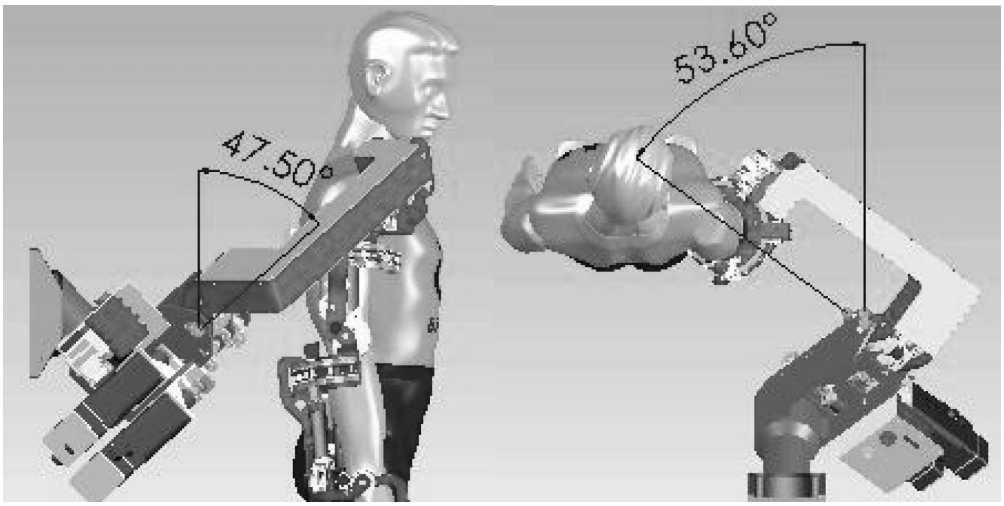

Figure 1.12: Singular posture of the shoulder joint design of (CADEN)-7 [66].

1.2.2 Actuation System Development

The actuation system of an exoskeleton robot is also of significant importance since it should be designed to provide sufficient drive force for motion actuation as well as to guarantee the safety of the users. The development of such actuation system consists of the hardware level actuator design and the software level control algorithm development.

Control Algorithms

Generally depending on the applications, an exoskeleton can be operated in at least one of the following three control modes: 1) torque control; 2) position control; and 3) impedance control.

The position control mode is commonly used to make sure that the exoskeleton joints rotate to the desired angles. For instance in the rehabilitation application, position control can be used to complete the tasks that are specified by certain trajectories. One typical example is the ARMin II in [60].

The torque control mode is generally used in applications where assistive torque or force needs to be provided by the exoskeleton to help augment the user's power. Examples of these applications could be on industrial assembly lines to share the loads with the workers in assembly activities, or in rehabilitations to help the patient with some residual mobility to finish the tasks. Typical examples can be found in [39] and [70]. In this case, an upper-level controller is need to decide how much assistive torque is needed to command the torque controller.

The impedance controller is an extension of the torque control and position control. It neither only controls the torque nor the position, but controls the relation of the two and

regulate the interaction force between the exoskeleton and the user to a target impedance. Both the position controller and the torque controller can be used as the low-level controllers. In the torque based impedance controller, the desired impedance model in the outer loop receives the position error between the desired position reference and the actual joint position, and then generates the torque reference for inner loop torque controller. The torque controller will enforce the torques exerted by the exoskeleton to be close to the torque references. Impedance controllers allow motion to deviate from the reference, and thus for rehabilitation applications, it is a desirable safety feature of exoskeleton systems which helps to release the patient in the cases of power loss or therapist-triggered cut-off [58]. Typical examples are the MGA in [8] and the ARMin III in [58].

Actuator Design

In order to achieve satisfactory control performance, which are typically based on the impedance control architectures, the exoskeleton should have low friction and negligible backlash, and the actuator also should be backdrivable [58]. And passive backdrivability helps to achieve good performance of the impedance controller [42].

Most upper limb exoskeleton designs utilize electric motors to produce the drive force for motion actuation. A number of these designs use gear and cable/tendon drive as their power transmission [20, 55, 56, 58, 73]. The drawback of this type of actuator is that the friction and backlash inherent with the gearbox could be significant, and the backdrivability of the actuator would decrease as the gearbox reduction ratio gets large. The authors of [24] use the direct drive approach to reduce the nonlinearity of the actuator, but as a result, the magnitude of the output force is greatly reduced, and the motor inertia is large. The (CADEN)-7 proposed in [65] uses brushed motors and cable-driven systems with two-stage pulley reductions as its actuators. Most brushed motors are mounted on a stationary base to reduce the exoskeleton weight and inertia. Moreover, compared with gear transmissions, cable and pulley system has the advantage of transmitting loads with extremely low friction and backlash which is desirable. However, the cable routing increases the mechanical design complexity. To obtain a backdrivable actuator which can also produce sufficient output force, some researchers choose the series elastic actuator (SEA) for their upper or lower limb exoskeleton designs [38, 39, 70, 84]. The SEA has an elastic component connecting its motor side and load side, and thus can be regarded as backdrivable even if the motor is geared with a high reduction reducer. Another merit of the SEA is that its output force can be evaluated by Hooke's law based on position sensor measurements on both sides, which means that the SEA can also work as a low-cost force/torque sensor.

Apart from electric motors, pneumatic muscles and hydraulic power have also been adopted by researchers due to their unique characteristics. Pneumatic muscles are lightweight, and simultaneously strong and compliant. The low impedance feature comes from the inherent compliance of air. The disadvantages of pneumatic muscles include nonlinearities in both force and airflow dynamics, and the requirement of an external source of compressed air [85]. Typical upper limb exoskeletons use actuators of this kind are [3, 37, 74, 82]. Hydraulic

actuators have compact size, low weight, and high force capabilities. Since hydraulic fluid is generally incompressible, the hydraulic actuator also has a relatively high-control bandwidth [89]. Their drawbacks include relatively low accuracy, leaking fluid, and the requirement of many companion parts. Typical design examples can be found in [57, 89].

1.3 Motivation and Contributions

As we have discussed in the previous sections, the integration of BMI study and exoskeleton technique can help to promote our understanding of fundamental principles in the neural control of movement in scenarios involving physical interactions with the world, as well as to motivate new generation of rehabilitation or power augmentation exoskeleton systems. In order to serve as the external apparatus that can help establish a closed-loop BMI and enable the macaque's proprioceptive feedbacks, the exoskeleton to be developed should be able to work in several different control modes to realize both data acquisition and motion actuation of the macaque's upper limb, which means the target functions of the proposed macaque exoskeleton are different from most of the existing human rehabilitation-oriented designs.

Per the previous discussions of the state of the art upper limb exoskeletons for both NHPs and humans, a list of requirements of developing such an apparatus for the macaques is summarized as follows:

- Biomorphic nature joints: exoskeletons are wearable devices and should match and capture the motion of each individual joint.
- Shoulder joint design with unlikely singularity in workspace: the shoulder joint of an upper limb exoskeleton should be designed with unlikely internal singularities (i.e., singular configurations not due to reaching joint limits) in the workspace for both large joint ROM and safety considerations.
- Compact: compactness is a necessity of an upper limb exoskeleton that is designed for macaques. Since the body dimensions of macaques are much smaller than those of humans, the mechanical components of the exoskeleton should be kept sufficiently compact.
- Firm attachment: considering that the two internal/external rotation joints of the upper arm and the forearm also serve as the attachment joints of the exoskeleton to the user's body segments, and that the macaque's body is furry, firm attachments are required.
- High power-to-weight ratio: the exoskeleton should be lightweight while capable of providing sufficient output torque to complete the designed tasks, which means that the exoskeleton should have a high power-to-weight ratio.

- Backdrivability: considering that the target users in this project are macaques which cannot explicitly communicate with the researchers during operations, backdrivability would allow the ease of subject-induced motion when the device is unpowered or reaching to a posture that is not safe or comfortable to the subject.
- Safe and comfortable: the exoskeleton should be designed safe and comfortable for the subject. Safety needs to be guaranteed on both hardware level and software level.

The requirements of biomorphic nature joints, singularity free in workspace, compactness and firm attachment need to be addressed during the kinematic modeling and structural design process, and the features of high power-to-weight ratio, backdrivability, and safe and comfortable motion actuation should be included in the actuator design and control stage.

This dissertation focuses on the mechatronic considerations on the development of an upper limb exoskeleton for macaques. In order to handle the challenges mentioned above, investigations have been made on both the kinematic modeling and structural design, and the actuator design and control aspects. The specific contributions of this work are listed here.

1. *A kinematic upper limb exoskeleton model which has a redundant shoulder joint and exhibits high manipulability.*
2. *A passive upper limb exoskeleton which enables macaque kinematic motion sensing and characterization, as well as safe animal training.*
3. *A compact, backdrivable and torque-reflecting cable-driven series elastic actuator which is impedance-controlled to achieve compliant motion actuation for subject-robot interactions.*
4. *An actuated upper limb exoskeleton which is driven by series elastic actuators and realizes data acquisition and motion actuation of the macaque upper limb in a BMI system.*

1.4 Dissertation Outline

The details of each chapter are as follows.

Chapter 2: Kinematic Design and Analysis of an Upper Limb Exoskeleton Model for Rhesus Macaques

A 6-DOF upper limb exoskeleton model with 4 DOFs at the shoulder complex is proposed in this chapter to achieve better manipulability than conventional shoulder models. The advantageous features of the proposed exoskeleton model are demonstrated by a series of kinematic analysis. Singularity and manipulability analysis is first investigated, and then a

gradient projection based joint space trajectory planning approach is provided as one way to utilize the redundancy of the proposed shoulder joint to avoid system unsafe regions. The effectiveness of the proposed shoulder joint model is evaluated by simulation studies.

Chapter 3: Development of a Passive Upper Limb Exoskeleton for Rhesus Macaques

The development of a passive upper limb exoskeleton for macaques is presented based on the kinematic exoskeleton model proposed in the Chapter 2. The mechanical design is introduced in terms of biomorphic joints and joint ranges of motion. Then real-time motion data acquisition and motion capture system based system kinematic calibration are discussed. The experimental results of the animal test are finally provided to demonstrate the effectiveness of the proposed passive exoskeleton.

Chapter 4: Design and Control of a Cable-Driven Series Elastic Actuator

In order to obtain a compact, backdrivable, high power-to-weight ratio, and torque-reflecting actuator for the actuated exoskeleton, a cable-driven SEA is proposed in this chapter. Both the mechanical design and the development of an interactive impedance controller are provided. The cable-driven mechanism of the proposed actuator helps achieve a compact and high power-to-weight ratio design, and the interactive impedance control algorithm helps realize a safe motion actuation when the user is in the loop. The effectiveness of the proposed actuator is verified by a series of experiments.

Chapter 5: Development of an Actuated Upper Limb Exoskeleton for Rhesus Macaques

On top of the development of the passive exoskeleton and the cable-driven SEA, the development of an actuated multi-DOF upper limb exoskeleton for macaques is presented in this chapter. Compared with existing 2D non-human primate exoskeleton KINARM, the proposed exoskeleton allows for freedom of movement in additional dimensions. The mechanical design is discussed in terms of kinematic structural design and actuation system development. Finally the system integration of the BMI with a macaque subject is introduced, and pilot animal test results are provided.

Chapter 6: Concluding Remarks and Open Issues

The concluding remarks of this dissertation are summarized in this chapter, and some open issues are also discussed as future work.

Chapter 2

Kinematic Design and Analysis of an Upper Limb Exoskeleton Model for Rhesus Macaques

2.1 Introduction

An exoskeleton generally refers to an external structural mechanism with joints and links that corresponds to those of the users [65]. It is a wearable device which is attached to the user's body segments for motion actuation. Kinematic design is one of the key aspects for developing an upper limb exoskeleton, and matching a mechanical exoskeleton to a biological structure faces difficulties, especially in the shoulder complex. Specifically, two major problems are axis alignment between the anatomical and device joints and the kinematic singularity of mechanical models, as has been discussed in Chapter 1. Compared with the axis alignment problem, the singularity issue in the shoulder complex design has not drawn the same amount of attention since rehabilitation-oriented exoskeletons typically do not require large ROM, and the training motions for patients are expected to be within certain patterns. Thus mechanism singularities can be intentionally avoided. However, for an exoskeleton designed for macaques, when operated in the passive tracking mode where the macaque's arm is free to do arbitrary motion, a shoulder joint design with unlikely singularity is of significance for allowing precise tracking and addressing safety concerns, considering macaques are generally non-cooperative.

The shoulder complex can be basically modeled by a ball-and-socket joint consisting of three rotational DOFs, which can be mechanically implemented using three serial revolute joints. The two conventions shown in Fig. 2.1 are widely used to describe the rotation sequence [72]. However, since both conventions use a triad model, singularities cannot be avoided if their postures require an alignment of their first joint axis with the third. To reduce the occurrence of kinematic singularities, several research groups revised the aforementioned standard triad models based on different concerns and assumptions. Typical designs are

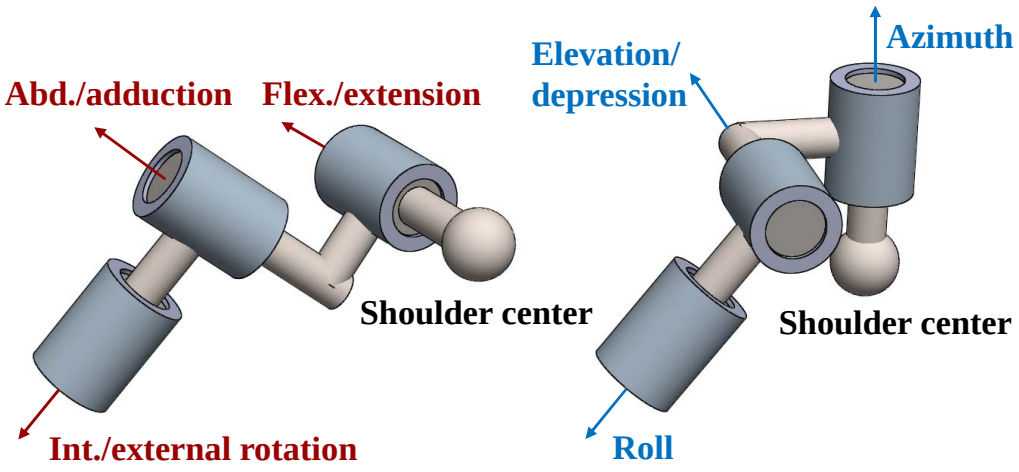

(a) flexion-abduction-rotation (b) azimuth-elevation-roll

Figure 2.1: Two rotation conventions for glenohumeral joint model.

(CADEN)-7 [65], MEDARM [4], and SAM [45]. Details of their design strategies has been detailed in Chapter 1. However, all these designs use a triad joint model to mimic the shoulder complex, making each task space posture correspond to a unique inverse solution for the joint space realization, therefore a singularity always exists.

In this chapter, a 6-DOF upper limb exoskeleton model with 4 DOFs at the shoulder complex is proposed to achieve better manipulability than conventional shoulder models. The advantageous features of the proposed exoskeleton model will be demonstrated in this chapter by a series of kinematic analysis. Singularity and manipulability analysis will be first investigated. Then a gradient projection based joint space trajectory planning approach will be provided as one way to utilize the redundancy of the proposed shoulder joint to avoid system unsafe regions. Simulation results will be provided to demonstrate the effectiveness of the proposed shoulder joint model.

2.2 Upper Limb Joints and an Exoskeleton Model

The functionality of primate upper limbs is determined by the shoulder complex, elbow complex, wrist, and hand.

The shoulder complex is one of the most difficult structures to model for an upper limb. Although [14] and [11] point out that the morphology of the macaque shoulder joint is not exactly the same as a human's, human upper limb structure can still serve as a reference for developing the kinematic design of an exoskeleton in the absence of macaque shoulder joint models in existing literature. [87] introduces a non-redundant 5-DOF mathematical model of the shoulder complex for humans including three rotational DOFs (abduction/adduction, flexion/extension, and internal/external rotation) and two transla-

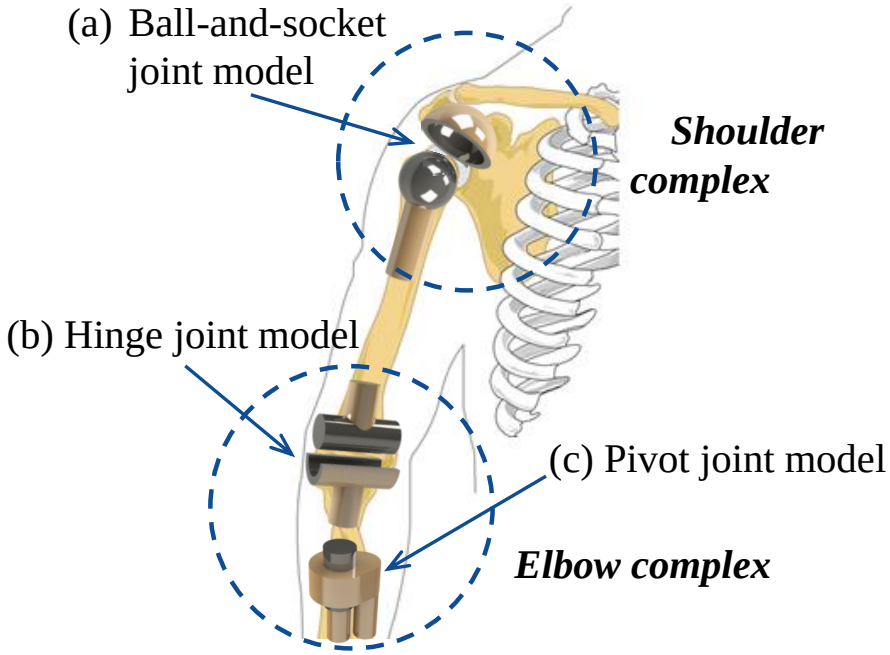

Figure 2.2: Mechanical models of the upper limb joints.

tional DOFs (elevation/depression, and protraction/retraction) with the thorax as the fixed base. However, in the engineering world, for simplicity, mostly only the glenohumeral joint (Fig. 1.4) is modeled for the shoulder complex using a ball-and-socket joint model, as shown in Fig. 2.2a. The elbow complex mainly consists of the elbow joint and the radioulnar joint. The former is commonly modeled using a hinge joint as shown in Fig. 2.2b, and the latter is generally regarded as a pivot joint corresponding to pronosupination of the forearm as shown in Fig. 2.2c. This DOF can be included either with the elbow or the wrist, and serves as a revolute joint connecting the elbow and the wrist. Considering the upper limb motion of interest in the BMI study, the wrist and the hand motions and their modeling are not investigated in this dissertation.

Fig. 2.3 shows a kinematic model of the proposed 6-DOF upper limb exoskeleton. Details of the mechanical design will be presented in Chapter 3. Based on the mechanical models for each joint illustrated in Fig. 2.2, four DOFs are assigned at the shoulder complex, one DOF is assigned at the elbow, and one DOF is assigned at the radioulnar joint. All joints are serially linked rotational joints. Compared with conventional 3-DOF shoulder joint models, the proposed 4-DOF model has more flexibility for positioning and trajectory tracking due to its possession of one more DOF than required.

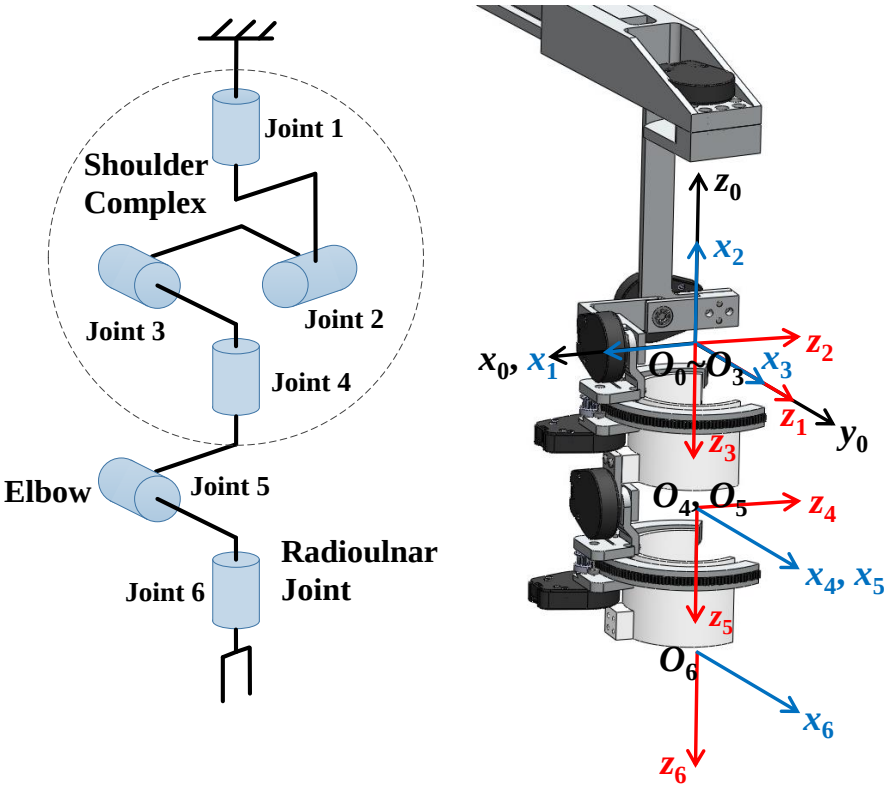

Figure 2.3: Proposed 6-DOF upper limb exoskeleton model.

2.3 Kinematic Modeling and Analysis

To evaluate the effectiveness of the proposed shoulder joint model to avoid kinematic singularities in future actuated exoskeleton designs, the kinematic properties of the proposed 4-DOF shoulder model will be investigated in this section.

2.3.1 System Kinematic Model

Denavit-Hartenberg (DH) parameters can fully define the kinematic model of a mechanism. Let $\boldsymbol{\theta} \in \mathbb{R}^6$ be the joint variable, then the DH parameters of the proposed exoskeleton model are as shown in Table 2.1 following the frame definition in Fig. 2.3, where L_1 and L_2 are the distance from the shoulder center to the elbow, and the distance from the elbow to the palm, respectively. The posture at $\boldsymbol{\theta} = [\pi/4,\ -\pi/2,\ \pi/2,\ 0,\ 0,\ 0]^\top$ is defined as the *home posture* of the exoskeleton.

Table 2.1: DH parameters of the proposed upper limb exoskeleton.

Joint	θ	d	a	α
1	θ_1	0	0	$-\frac{\pi}{2}$
2	θ_2	0	0	$\frac{\pi}{2}$
3	θ_3	0	0	$-\frac{\pi}{2}$
4	θ_4	L_1	0	$\frac{\pi}{2}$
5	θ_5	0	0	$-\frac{\pi}{2}$
6	θ_6	L_2	0	0

Forward Kinematics

Forward kinematics defines the subject's wrist position and orientation in the base frame as a function of the joint variables. The wrist position vector $\boldsymbol{p}^0$ and the orientation vectors $(\boldsymbol{n}^0, \boldsymbol{s}^0, \boldsymbol{a}^0)$ can be obtained by calculating the coordinate transformation matrix $\boldsymbol{T}_6^0(\boldsymbol{\theta})$ describing the wrist Frame 6 with respect to the base Frame 0

$$\boldsymbol{T}_6^0(\boldsymbol{\theta}) = \boldsymbol{A}_1^0\boldsymbol{A}_2^1\boldsymbol{A}_3^2\boldsymbol{A}_4^3\boldsymbol{A}_5^4\boldsymbol{A}_6^5 = \begin{bmatrix} \boldsymbol{n}^0 & \boldsymbol{s}^0 & \boldsymbol{a}^0 & \boldsymbol{p}^0 \\ 0 & 0 & 0 & 1 \end{bmatrix} \tag{2.1}$$

where $\boldsymbol{\theta} = \begin{bmatrix} \theta_1 & \theta_2 & \theta_3 & \theta_4 & \theta_5 & \theta_6 \end{bmatrix}^{\mathrm{T}}$ denotes the joint space angles, and $\boldsymbol{A}_i^{i-1}$ is the transformation matrix from Frame i to Frame $i-1$.

Jacobian Matrix

A linear mapping between the task space velocity $\boldsymbol{v}_e$ and the joint space velocity $\dot{\boldsymbol{\theta}}$, i.e., *differential kinematics*, can be established via the Jacobian matrix as

$$\boldsymbol{v}_e = \boldsymbol{J}(\boldsymbol{\theta})\dot{\boldsymbol{\theta}} \tag{2.2}$$

where $\boldsymbol{v}_e = \begin{bmatrix} \dot{\boldsymbol{p}}_e^{\mathrm{T}} & \boldsymbol{\omega}_e^{\mathrm{T}} \end{bmatrix}^{\mathrm{T}}$ and $\boldsymbol{J}(\boldsymbol{\theta}) = \begin{bmatrix} \boldsymbol{J}_p(\boldsymbol{\theta})^{\mathrm{T}} & \boldsymbol{J}_o(\boldsymbol{\theta})^{\mathrm{T}} \end{bmatrix}^{\mathrm{T}}$. The end point linear velocity $\dot{\boldsymbol{p}}_e$ and the angular velocity $\boldsymbol{\omega}_e$ can be then expressed as

$$\dot{\boldsymbol{p}}_e = \boldsymbol{J}_p(\boldsymbol{\theta})\dot{\boldsymbol{\theta}}, \quad \boldsymbol{\omega}_e = \boldsymbol{J}_o(\boldsymbol{\theta})\dot{\boldsymbol{\theta}} \tag{2.3}$$

2.3.2 Singularity Analysis

Since the designs of the elbow joint and the forearm rotation joint are following the subject's anatomical structure, the subject's natural actuation DOFs should be preserved at these two joints. Thus, we are only interested in the motion realization by the other four joints (the shoulder complex model), in particular, the singularity and joint limits avoidance of these four joints.

In order to analyze mechanism singular configurations, the Jacobian matrix is usually the first tool to be used, since it is a function of the joint space configuration $\boldsymbol{\theta}$, and when a mechanism is at its singularities, the Jacobian matrix $\boldsymbol{J}(\boldsymbol{\theta})$ will become rank-deficient [80].

Table 2.2: Ranges of the joint space angles.

Angle	θ_1	θ_2	θ_3	θ_4
ADL range (°)	170	145	110	150
DH convention range (°)	$-50 \sim 120$	$-205 \sim -60$	$-55 \sim 55$	$-75 \sim 75$

For this spherical shoulder complex model with fixed upper arm length, the end point is moving on a spherical surface. Thus the orientation Jacobian $\boldsymbol{J}_o(\boldsymbol{\theta})$[1] will be investigated, and can be expressed as

$$\boldsymbol{J}_o(\boldsymbol{\theta}) = \begin{bmatrix} 0 & -s_1 & c_1 s_2 & -c_1 c_2 s_3 - s_1 c_3 \\ 0 & c_1 & s_1 s_2 & -s_1 c_2 s_3 + c_1 c_3 \\ 1 & 0 & c_2 & s_2 s_3 \end{bmatrix} \tag{2.4}$$

where $s_i = \sin(\theta_i)$, and $c_i = \cos(\theta_i)$.

Using (2.4) we can find that the orientation Jacobian matrix $\boldsymbol{J}_o(\boldsymbol{\theta})$ will lose rank (i.e., singularity will occur) for the following four cases:

1. $\theta_2 = -\pi$, $\theta_3 = 0$, θ_1 and θ_4 are arbitrary;
2. $\theta_2 = -\pi$, $\theta_3 = \pi$, θ_1 and θ_4 are arbitrary;
3. $\theta_2 = 0$, $\theta_3 = 0$, θ_1 and θ_4 are arbitrary;
4. $\theta_2 = 0$, $\theta_3 = \pi$, θ_1 and θ_4 are arbitrary.

Note that not all of these four configurations are the actual singularities of this 4-DOF shoulder complex model. The ranges of the first four joint angles are listed in Table 2.2[2]. Thus among the aforementioned four potential singularities, there is only one singular configuration within the defined joint angle ranges, i.e., when $\theta_2 = -\pi$ and $\theta_3 = 0$, corresponding to the situation where Axis 1 is collinear with Axis 3, and Axis 2 is collinear with Axis 4, respectively, as shown in Fig. 2.4. The rotational DOF about the x_0 axis in the task space is lost.

2.3.3 Manipulability Analysis

To quantitatively evaluate the mechanism's manipulation ability, the measure of *manipulability* [88] can be defined as

$$c_m(\boldsymbol{\theta}) = \sqrt{\det(\boldsymbol{J}(\boldsymbol{\theta})\boldsymbol{J}(\boldsymbol{\theta})^\top)}, \tag{2.5}$$

[1]Hereafter, $\boldsymbol{\theta} = [\ \theta_1 \quad \theta_2 \quad \theta_3 \quad \theta_4\ ]^{\mathrm{T}}$ and $\boldsymbol{J}_o(\boldsymbol{\theta}) \in \mathbb{R}^{3\times 4}$ due to the emphasis on the 4-DOF shoulder complex model.

[2]Note, angles in first row are defined in the way commonly used in the biomechanics world, while angles in the second row are defined following the DH parameter convention in Fig. 2.3, with the home position of $\theta_1 = \pi/4$, $\theta_2 = -\pi/2$, $\theta_3 = \pi/2$, and $\theta_4 = 0$.

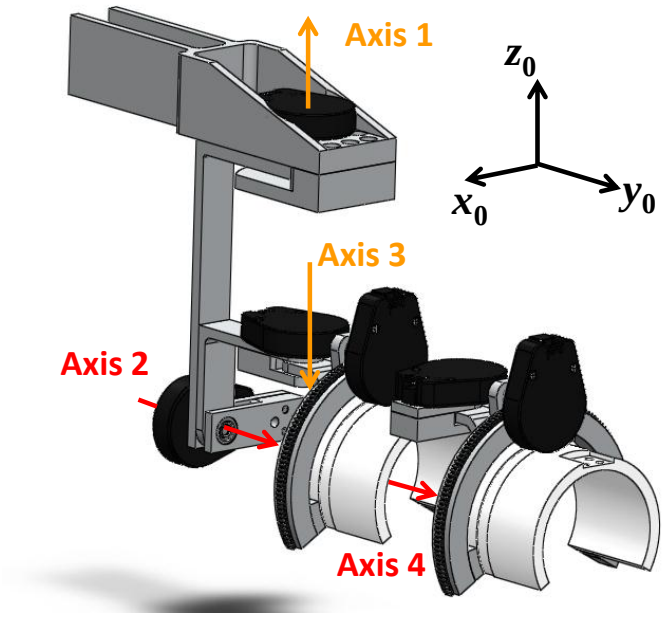

Figure 2.4: Singular posture of the proposed 4-DOF shoulder complex model.

where $\boldsymbol{J}(\boldsymbol{\theta})$ is a general Jacobian matrix.

The manipulability of a mechanism depends on its link lengths, number of joints, and the dimension of its task space. In order to compare manipulabilities of different manipulators working in different workspaces, [36] proposed the concept *relative manipulability* which is independent of scales and dimension orders:

$$c_{rel}(\boldsymbol{\theta}) = \frac{\sqrt[m]{\det(\boldsymbol{J}(\boldsymbol{\theta})\boldsymbol{J}(\boldsymbol{\theta})^\top)}}{\sqrt{\sum_{i=1}^{n}(a_i^2 + d_i^2)}}, \tag{2.6}$$

where n is the number of joints, m is the dimension order of the task space, and a_i and d_i are the i-th link length and joint offset defined in the DH parameters convention, respectively.

The manipulability or relative manipulability provides a measure of the dexterity of the exoskeleton given a joint space configuration. The mapping from the joint space to the task space may not be unique, in particular, for redundant mechanisms or scenarios where only partial task space constraints are considered (e.g., positions without orientations). Then the manipulability of a particular task space point may take multiple values. Thus we introduce the terminology *manipulability distribution* here. As an example to demonstrate the advantage of the proposed design, the manipulability distributions of the rotational degrees of freedom on the task space transverse plane (i.e., the $x_0O_0y_0$ plane defined in Fig. 2.3) are investigated for the following four models: the conventional standard triad model (IKO, [52]), the triad models with rarely-reached singular direction ((CADEN)-7),

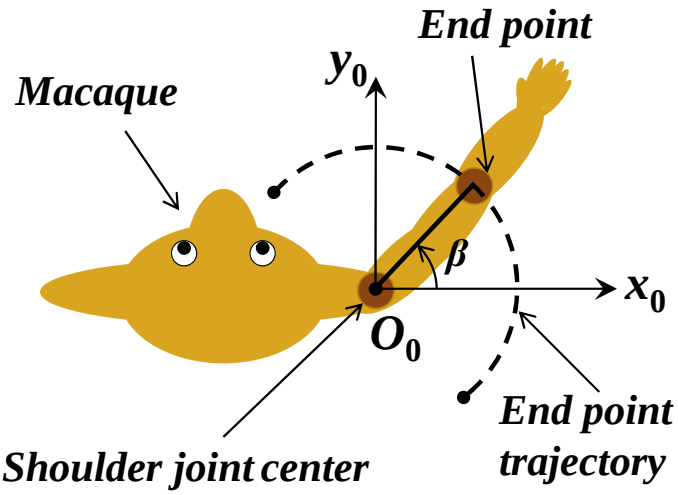

Figure 2.5: Top view of macaque on the transverse plane. Macaque is plotted with its shoulder joint center fixed and its elbow as the end point.

and with optimized axis relative angles (MEDARM), as well as the proposed model. The performance of the exoskeleton on this horizontal plane is important considering the designed BMI tasks previously discussed. An illustration of the manipulability study is shown in Fig. 2.5 with the elbow position as the investigated end point.

Fig. 2.6 plots the manipulability distributions of the four models with their end points at different directions ($\beta = -50° \sim 140°$, defined in Fig. 2.5) on the horizontal plane. Fig. 2.6a shows the manipulability distribution of the IKO shoulder joint model. It uses rotation convention (a) with the strict forward direction ($\beta = 90°$) as its singular direction on the horizontal plane. Each posture is uniquely determined by one joint space realization due to its possession of only three DOFs, which means the singularity will always occur (i.e., the manipulability vanishes) in the vicinity of the strict forward direction and one rotational DOF (either shoulder flexion/extension, or abduction/adduction) will be lost.

Fig. 2.6b presents the manipulability distribution of the shoulder joint of (CADEN)-7. This design is also an orthogonal triad model using the rotation convention (a). But with the first joint axis having an acute angle about the vertical direction, the singularity of this model was designed in a direction that is rarely (statistically) reached by the subject. Thus compared with the IKO shoulder joint model, there is no "hard" singularities within the feasible workspace (in the horizontal plane), and the average manipulability is improved. However, singularities still exist in some other regions of the workspace (outside the horizontal plane). Therefore, it is still possible for the subject to enter the vicinity of the singular region, resulting in limited feasible workspace.

Fig. 2.6c plots the manipulability distribution of the MEDARM shoulder joint. It features the first two revolute axes with an optimized angle rather than an orthogonal relationship. By inclusion of an "azimuth" (not a full azimuth) axis, the ROM on the horizontal plane is

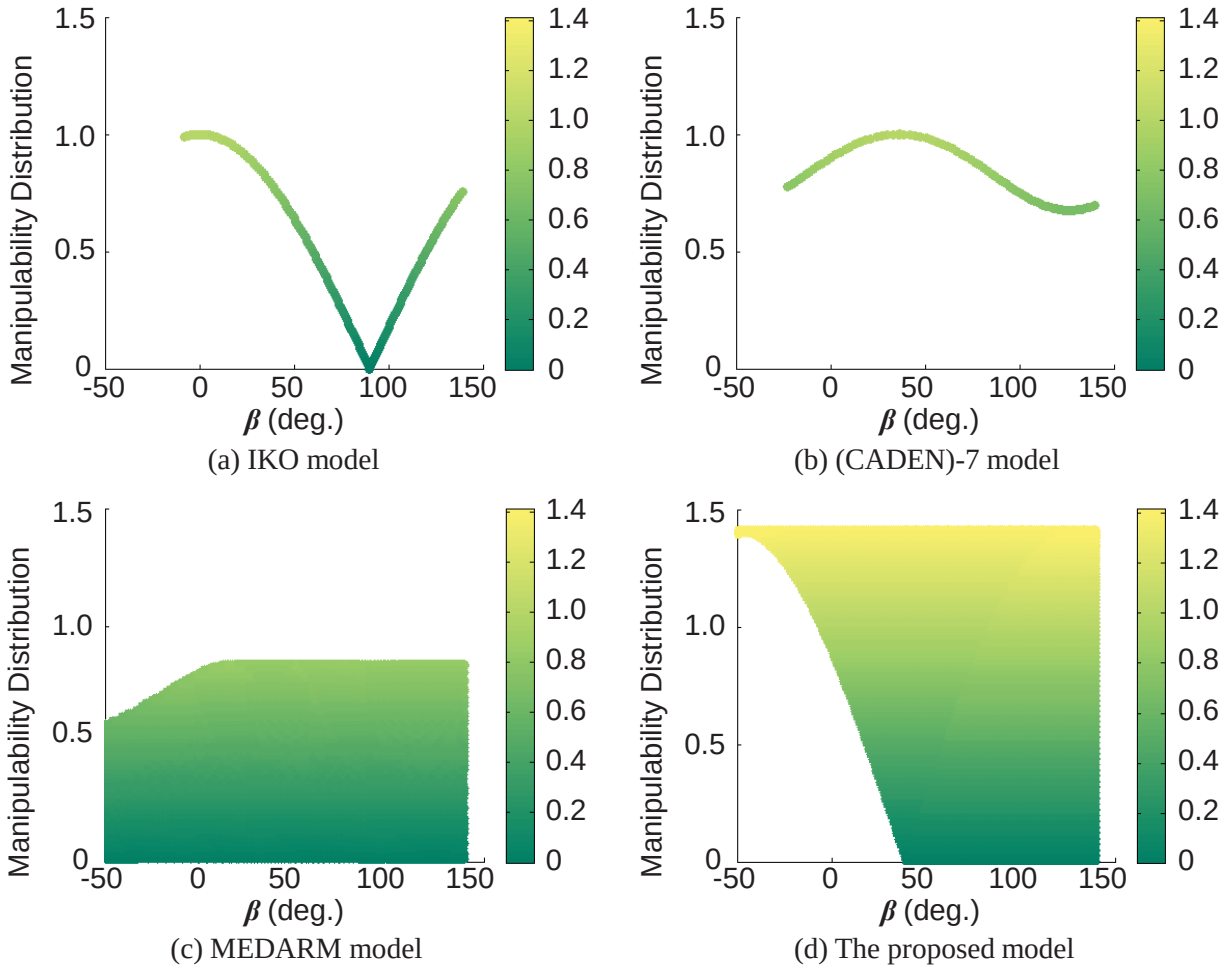

(a) IKO model

(b) (CADEN)-7 model

(c) MEDARM model

(d) The proposed model

Figure 2.6: Manipulability distributions of four models on the horizontal plane.

extended, though some regions are physically unable to be reached by a macaque. Besides, the non-unique inverse kinematic solutions lead to multiple joint space realizations since only task space positions (not orientations) are considered in this example. Thus it has more flexibility regarding the upper arm's motion on the horizontal plane. However, its average manipulability is relatively low due to its lack of a dedicated internal/external rotation joint for the upper arm.

Fig. 2.6d shows the manipulability distribution of our proposed model with four DOFs combining both of the two glenohumeral joint rotation conventions (convention (a) and (b)). From Fig. 2.6a to Fig. 2.6d, the improvement of the manipulabilities is evident. With an azimuth axis, this model enjoys the similar multiple joint space realizations as the MEDARM model on the horizontal plane. The inclusion of a standard triad model following the azimuthal DOF makes it possible to obtain the maximal manipulability value in all directions

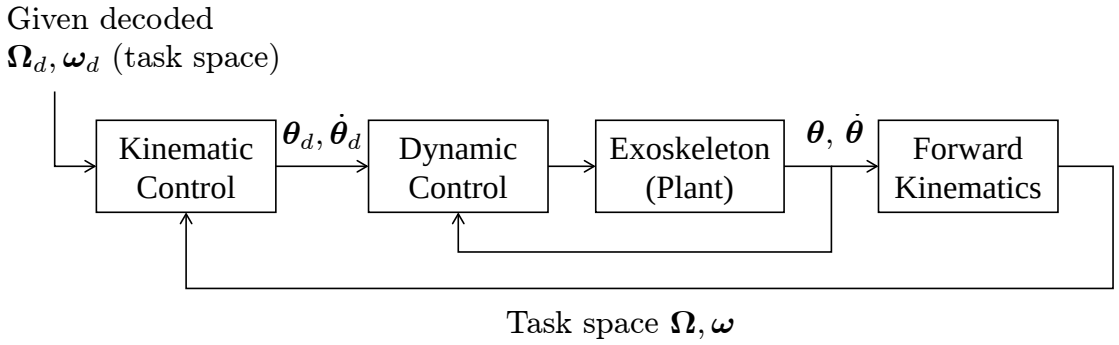

Figure 2.7: Block diagram of the task space trajectory tracking of the shoulder joint.

(i.e., the feasible workspace is the whole horizontal plane). In fact, each posture of the proposed shoulder joint model possesses different levels of manipulabilities. Thus it is possible for an actuated mechanism with the same kinematic structure to avoid the singular configuration by properly selecting the joint space trajectories, and one approach is the gradient projection control [80] which will be presented in Section 2.4. Similar manipulability advantages can also be found in other regions of the workspace.

2.4 Joint Space Trajectory Planning of the Redundant Shoulder Model

Our goal is to design an actuated upper limb exoskeleton with several control modes, to realize both passive data acquisition and active control of the macaque's upper limb motion for the BMI study. This actuated exoskeleton may follow the structure of the current passive version. Thus it is of interest to verify whether the designed exoskeleton kinematic model is able to avoid undesired workspace (i.e., singularity and joint limits) when given the actuation ability to follow the desired task space trajectory.

2.4.1 Overview of Task Space Trajectory Tracking

As mentioned above, we are particularly interested in the four shoulder complex joints which are essential to realize 3D orientation of the upper arm. Normally, the desired task is given in the task space (i.e., task space orientation $\boldsymbol{\Omega}_d$ and/or angular velocity $\boldsymbol{\omega}_d$ for the 4-DOF glenohumeral joint exoskeleton). To achieve the desired task, two control loops are typically utilized as shown in Fig. 2.7 – one inner dynamic control loop and one outer kinematic control loop.

Kinematic Control

The kinematic control loop generates the desired joint space trajectory (e.g., $\boldsymbol{\theta}_d$ and $\dot{\boldsymbol{\theta}}_d$) from the desired task space motion (e.g., $\boldsymbol{\Omega}_d$ and $\boldsymbol{\omega}_d$). A simple first-order inverse kinematic solution is given as [5]

$$\dot{\boldsymbol{\theta}}_d = \boldsymbol{J}_o^{\dagger}(\boldsymbol{\omega}_d + \boldsymbol{K}_o \boldsymbol{e}_o) + (\boldsymbol{I} - \boldsymbol{J}_o^{\dagger}\boldsymbol{J}_o)\dot{\boldsymbol{\theta}}_N \tag{2.7}$$

where $\boldsymbol{J}_o^{\dagger} = \boldsymbol{J}_o{}^T(\boldsymbol{J}_o\boldsymbol{J}_o{}^T)^{-1}$ is the *pseudo-inverse* of $\boldsymbol{J}_o$, $\boldsymbol{K}_o$ is a positive definite matrix, $(\boldsymbol{I} - \boldsymbol{J}_o^{\dagger}\boldsymbol{J}_o)$ is a projector into the null space of $\boldsymbol{J}_o$, and $\dot{\boldsymbol{\theta}}_N$ is an arbitrary vector to be designed. $\boldsymbol{e}_o$ is the task space *orientation error*, and the method to calculate $\boldsymbol{e}_o$ is well documented in [51] and will not be detailed here. Note that, (2.7) provides infinite solutions due to the redundant exoskeleton design, whereas $\dot{\boldsymbol{\theta}}_N$ is the free variable to be designed to shape the final inverse kinematic solution to avoid reaching singularities and joint limits, which can thus be regarded as the control action to be designed.

Dynamic Control

The dynamic control loop is used to control the exoskeleton joints to track the desired joint space trajectory. The general form of robot dynamics is given by

$$\boldsymbol{M}(\boldsymbol{\theta})\ddot{\boldsymbol{\theta}} + \boldsymbol{N}(\boldsymbol{\theta}, \dot{\boldsymbol{\theta}}) = \boldsymbol{\tau}, \tag{2.8}$$

where $\boldsymbol{M}(\boldsymbol{\theta})$ is the mass matrix, $\boldsymbol{N}(\boldsymbol{\theta}, \dot{\boldsymbol{\theta}})$ is a vector of Coriolis and gravity terms, and $\boldsymbol{\tau}$ is a vector of joint torques. To realize joint space trajectory tracking, either centralized or decentralized control approaches can be used. Typical methods are PD control and computed torque control.

2.4.2 Unsafe Region Description

On one hand, obviously the singularity issue should be taken into consideration. As previously discussed, the manipulability defined in (2.5) can serve as the metric to evaluate system's singularity condition. Fig. 2.8 plots the distribution of this metric over different configurations of (θ_2, θ_3). We can notice that this value will decrease as system approaches to the singularity, and will stay relative large when system is away from the singular configuration. Thus we rewrite Eq. (2.5) as the manipulability metric as

$$\ell_m(\boldsymbol{\theta}) := \sqrt{\det(\boldsymbol{J}_o(\boldsymbol{\theta})\boldsymbol{J}_o^{\intercal}(\boldsymbol{\theta}))} \tag{2.9}$$

On the other hand, when we do the joint space trajectory planning, only the realizations with all the joint space variables located within the joint limits are feasible. Therefore, it is of practical significance to also take the joint limits issue into consideration. There are many metrics to describe mechanism's distance to the joint limits, and one candidate is

$$\ell_l(\boldsymbol{\theta}) := 1 - e^{-k \prod_{i=1}^{4} \frac{(\theta_i - \theta_{i,\min})(\theta_{i,\max} - \theta_i)}{(\theta_{i,\max} - \theta_{i,\min})^2}} \tag{2.10}$$

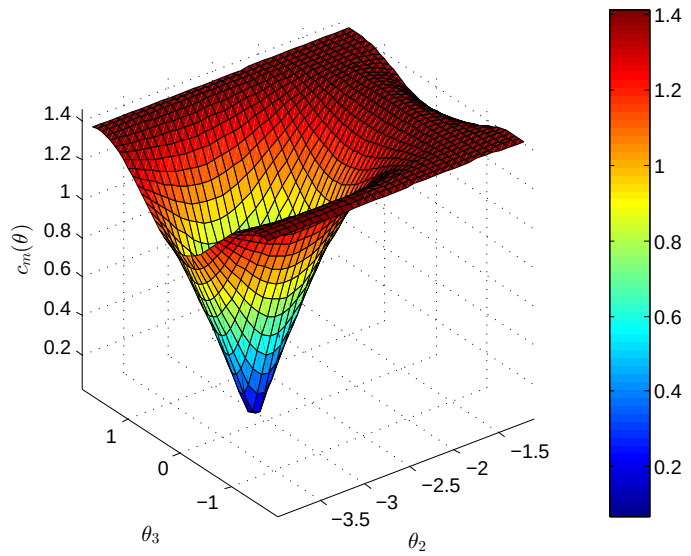

Figure 2.8: System singularity metric.

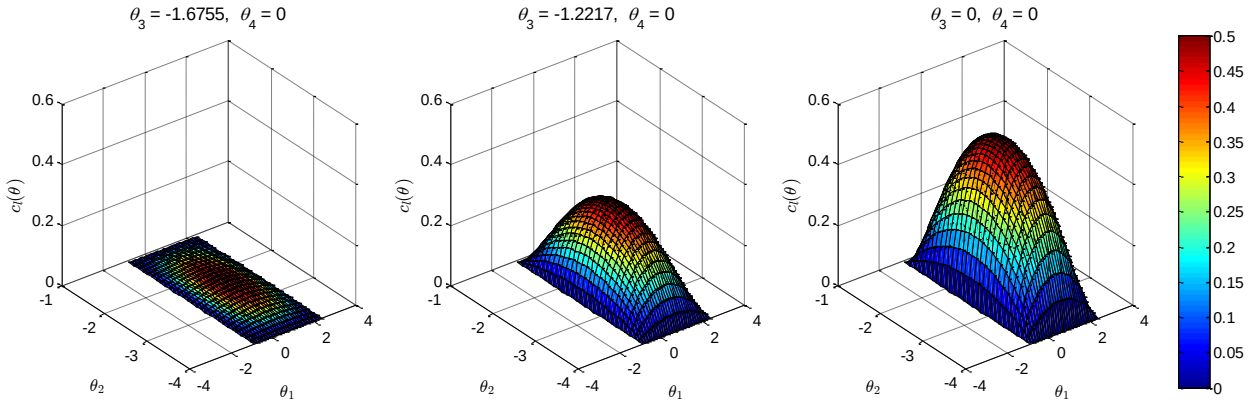

Figure 2.9: System joint limits metric.

where $\theta_{i\,\min}$ and $\theta_{i\,\max}$ are the minimum and maximum position limits for the i-th joint, respectively. k is a customary positive scalar. Fig. 2.9 shows three clips of the distribution evolution of this metric over (θ_1, θ_2) when θ_3 increases from a neighborhood around its limits to the middle value of the joint range while θ_4 remains at its center of joint range. As we expect, this metric gets to its maximum when all the joint variables are at their middle values, and tends to vanish if any of them reaches to their joint limits.

To this end, we can define the universe set of the joint variables as

$$\Omega_{\boldsymbol{\theta}} := \{\boldsymbol{\theta} : \ \theta_{i\,\min} \leq \theta_i \leq \theta_{i\,\max}, \ i = 1, \ 2, \ 3, \ 4.\}. \tag{2.11}$$

With the help of the singularity metric and the joint limits metric, system's safe set of the joint variables can be defined as

$$S := \{\boldsymbol{\theta} : \ \ell_m(\boldsymbol{\theta}) \geq K_m, \ \ell_l(\boldsymbol{\theta}) \geq K_l, \ \boldsymbol{\theta} \in \Omega_{\boldsymbol{\theta}}\}, \tag{2.12}$$

where K_m and K_l are two threshold constant scalars. And accordingly, system joint variable's unsafe set will be

$$U := \{\boldsymbol{\theta} : \ \boldsymbol{\theta} \notin S, \ \boldsymbol{\theta} \in \Omega_{\boldsymbol{\theta}}\}. \tag{2.13}$$

2.4.3 Gradient Projection Method

When the manipulability metric and the joint limit metric are considered simultaneously, the objective function to be maximized is

$$c(\boldsymbol{\theta}) := \rho \ell_m^0(\boldsymbol{\theta}) + (1-\rho)\ell_l^0(\boldsymbol{\theta}), \tag{2.14}$$

where $\rho \in (0, 1)$ is a weighting factor, and $\ell_m^0(\boldsymbol{\theta})$ and $\ell_l^0(\boldsymbol{\theta})$ are the normalized metrics of manipulability and joint limits, respectively.

A typical choice of $\dot{\boldsymbol{\theta}}_N$ is [80]

$$\dot{\boldsymbol{\theta}}_N = K_u \frac{\partial c(\boldsymbol{\theta})}{\partial \boldsymbol{\theta}}, \tag{2.15}$$

where $K_u > 0$. This approach is called *gradient projection method*, and $\dot{\boldsymbol{\theta}}_N$ in this form locally maximizes the objective function $c(\boldsymbol{\theta})$.

To investigate the stability of this approach, the following assumptions are worth considering:

- The dynamic control loop can be simplified as

$$\boldsymbol{\theta} = \boldsymbol{\theta}_d. \tag{2.16}$$

- The time derivative of the orientation error can be defined as

$$\dot{\boldsymbol{e}}_o = \boldsymbol{\omega}_d - \boldsymbol{\omega} \tag{2.17}$$

In reality, the first simplification is reasonable since this study focuses on the kinematic control for singularity and joint limit avoidance, and the dynamic control bandwidth is generally much higher than the kinematic control. Besides, the animal-exoskeleton system normally does not require fast motions or rapid accelerations. For the second assumption, although there are different ways of defining orientation errors under different assumptions, Eq. (2.17) is one reasonable way when the orientation error is small [80].

Based on the above assumptions, the following proposition investigates stability with this approach.

Proposition 2.1. *Under the above assumptions, the desired joint space trajectory generated by Eq.* (2.7) *and Eq.* (2.15) *guarantees that the task space orientation tracking error converges to zero asymptotically.*

Proof. Since $\boldsymbol{\theta} = \boldsymbol{\theta}_d$, by Eq. (2.7) we have

$$\dot{\boldsymbol{\theta}} = \boldsymbol{J}_o^{\dagger}(\boldsymbol{\omega}_d + \boldsymbol{K}_o \boldsymbol{e}_o) + (\boldsymbol{I} - \boldsymbol{J}_o^{\dagger}\boldsymbol{J}_o)\dot{\boldsymbol{\theta}}_N.$$

Premultiply $\boldsymbol{J}_o(\boldsymbol{\theta})$ on both sides we have

$$\boldsymbol{J}_o(\boldsymbol{\theta})\dot{\boldsymbol{\theta}} = \boldsymbol{\omega}_d + \boldsymbol{K}_o \boldsymbol{e}_o.$$

Since $\boldsymbol{\omega} = \boldsymbol{J}_o(\boldsymbol{\theta})\dot{\boldsymbol{\theta}}$, we then have

$$\boldsymbol{\omega} = \boldsymbol{\omega}_d + \boldsymbol{K}_o \boldsymbol{e}_o.$$

Noting Eq. (2.17), this equation means

$$\dot{\boldsymbol{e}}_o + \boldsymbol{K}_o \boldsymbol{e}_o = \boldsymbol{0}.$$

Hence, with a proper choice of $\boldsymbol{K}_o$, for example, $\boldsymbol{K}_o = k_o \cdot \boldsymbol{I}$ and $k_o > 0 \in \mathbb{R}$, the orientation error $\boldsymbol{e}_o$ converges to zero asymptotically. □

2.4.4 Simulation Study

Consider the following sequence of the shoulder motion which may enter the singular configuration with the proposed shoulder joint model: home position → 90° abduction → 90° horizontal rotation → 90° extension → 90° internal rotation.

After having executed an abduction of 90°, Axis 1 and Axis 3 are collinear. For the next move, there are two ways of doing the 90° horizontal rotation motion, as shown in Fig. 2.10. One strategy is to rotate Axis 3 which will result in Fig. 2.10b. Since Axis 2 aligns with Axis 4, the mechanism enters the singular posture, losing the DOF of conducting the next 90° extension motion. This is not desirable. However, if Axis 1 is selected to achieve the second move, before executing the 90° extension in the next step, the mechanism still possesses three rotational DOFs, as shown in Fig. 2.10c, which means that by using appropriate joint space trajectory planning strategy, the kinematic singularity of the mechanism can be avoided.

Next, the kinematic control law by Eq. (2.7) and Eq. (2.15) will be utilized to track the aforementioned task space motion. Fig. (2.11) shows the joint space trajectories of the 4-DOF shoulder model during kinematic control. The values of $\theta_1 \sim \theta_4$ follow the DH rule introduced in Section 2.3.1. It can be noticed that at the onset time of the horizontal rotation motion (i.e., $t = 2.5$sec), Axis 1's motion is much more significant than Axis 3's, which is the result of using Eq. (2.15) to locally maximize the manipulability metric defined in Eq. (2.9). The task space motion is shown in Fig. 2.12. This result matches the nonsingular strategy in Fig. 2.10c well, and the reason why Axis 3 also slightly moved is because Eq. (2.15) is

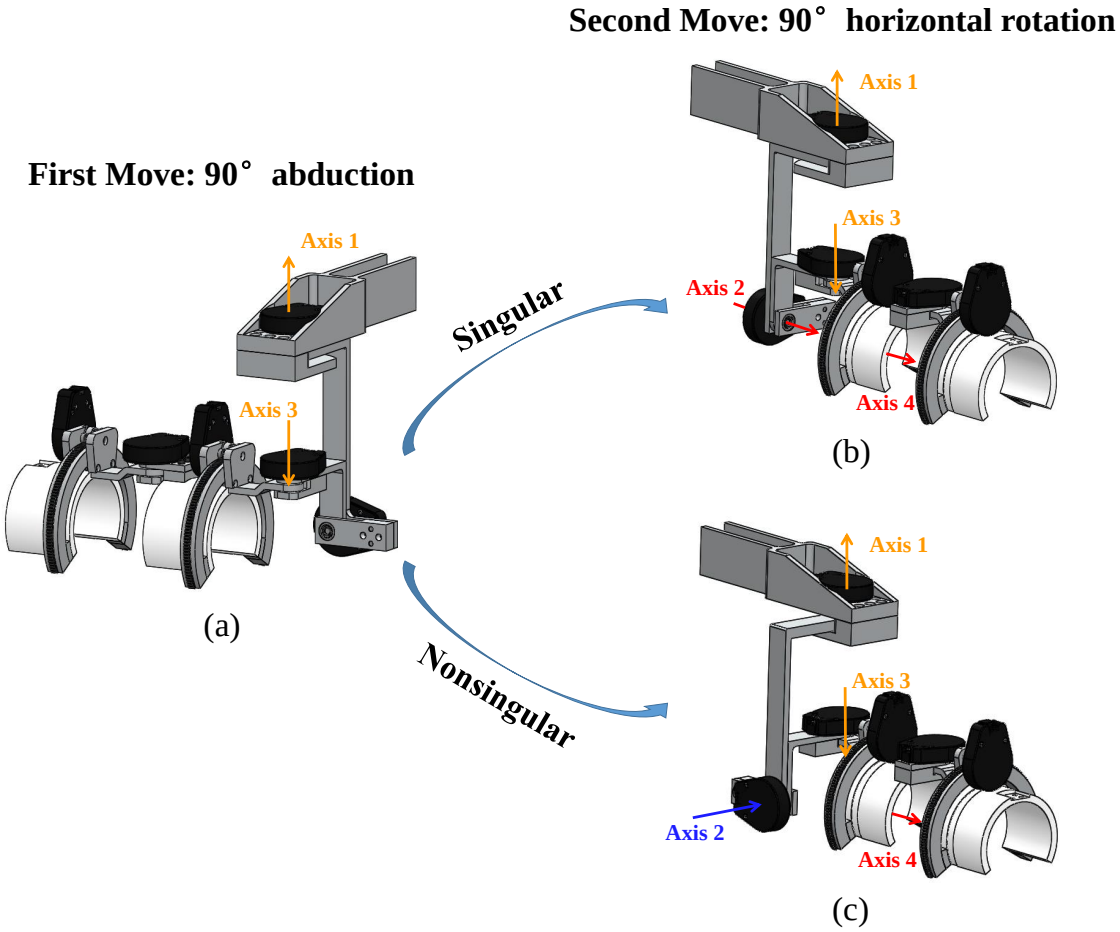

Figure 2.10: Singular and nonsingular joint space trajectories for one same shoulder joint motion in task space.

maximizing the joint limit metric defined in Eq. (2.10) to avoid θ_1 reaches its limit. The behaviors of the normalized manipulability metric and the joint limit metric are shown in Fig. 2.13, from which we can see that tradeoffs between the manipulability metric and the joint limit metric were made during the kinematic control which was adjusted by the weighting factor in Eq. (2.14), but the values of two metrics were kept at a relatively high level due to the selection of Eq. (2.15) to adjust the null space motion to prevent the mechanism from entering into the unsafe region. The corresponding orientation error is plotted in Fig. 2.13c, which demonstrates the convergence of the orientation error by the kinematic control.

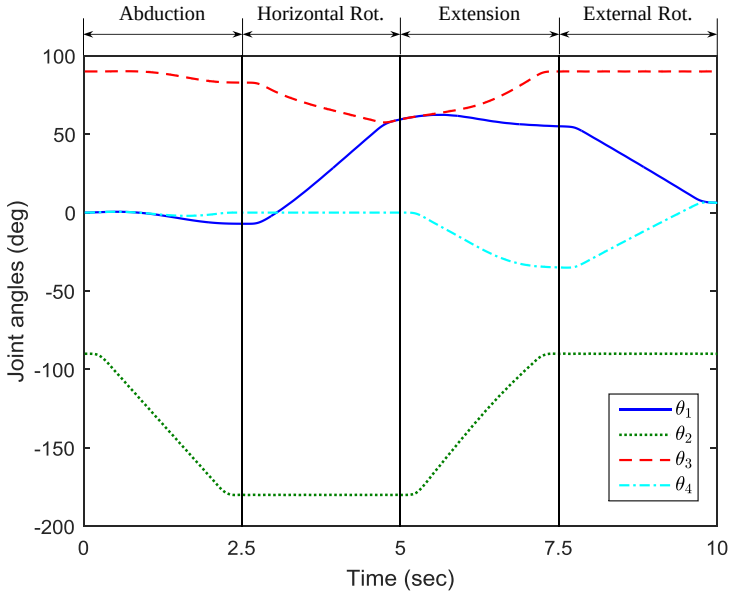

Figure 2.11: Joint space trajectories during kinematic control.

2.5 Chapter Summary

This chapter presented the kinematic design and analysis of a 6-DOF upper limb exoskeleton model for macaque monkeys. The anatomical structure of the primate upper limb was first introduced based on existing literature on human upper limb extremity. The commonly used upper limb models in both biomechanics world and the engineering world were presented. Then a 6-DOF upper limb exoskeleton model with four DOFs at the shoulder complex was proposed to achieve more flexible manipulation of the mechanism. The kinematic singularity of the proposed shoulder complex model was discussed and quantitatively investigated based on the manipulability metric. The manipulabilities of four different shoulder complex designs were compared, and the results indicated that the proposed model had the ability to avoid entering the vicinity of system singularity by appropriately planning joint space trajectories. Finally gradient projection method based kinematic control was proposed for joint space trajectory planning of the redundant should joint model. Simulation study of one task space motion tracking which may result in the singular configuration was investigated to demonstrate how the redundancy can be utilized to avoid system unsafe region.

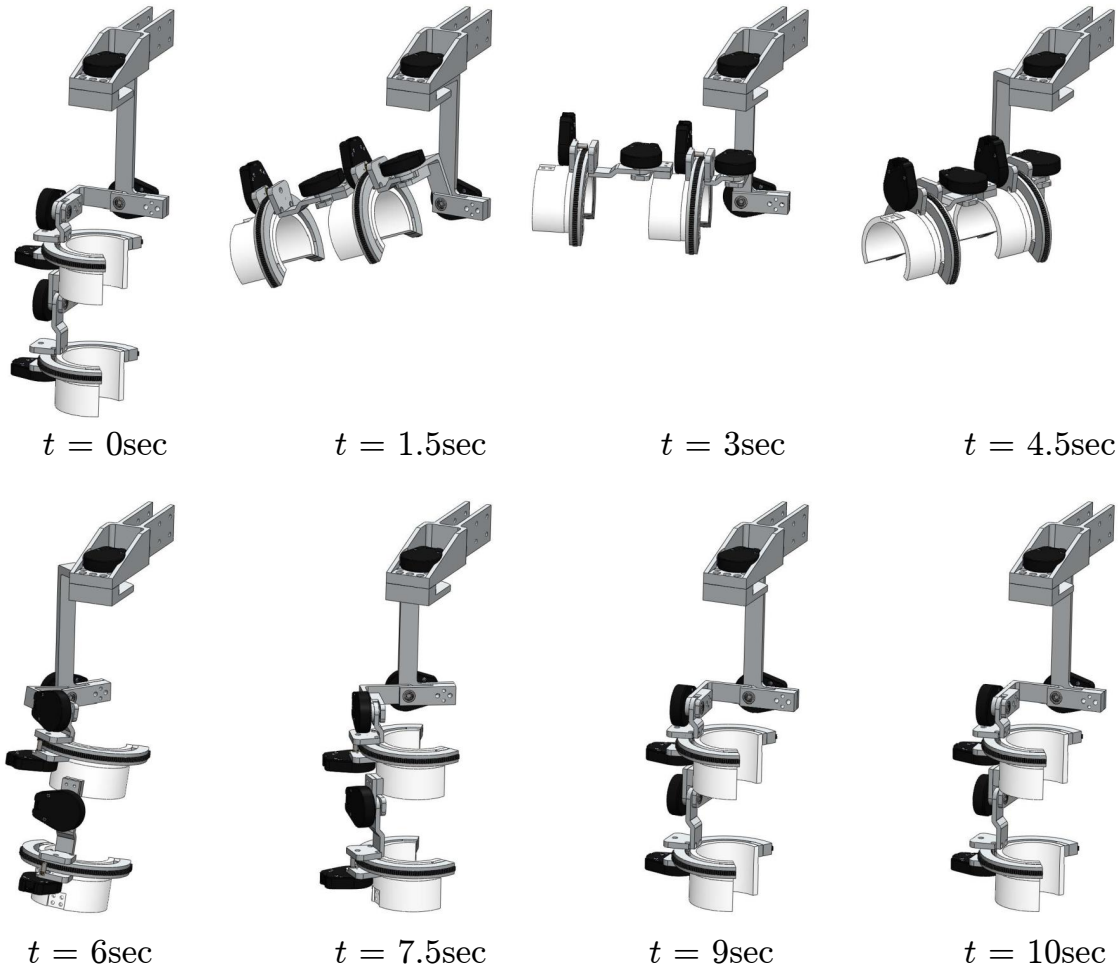

Figure 2.12: Task space motion during kinematic control.

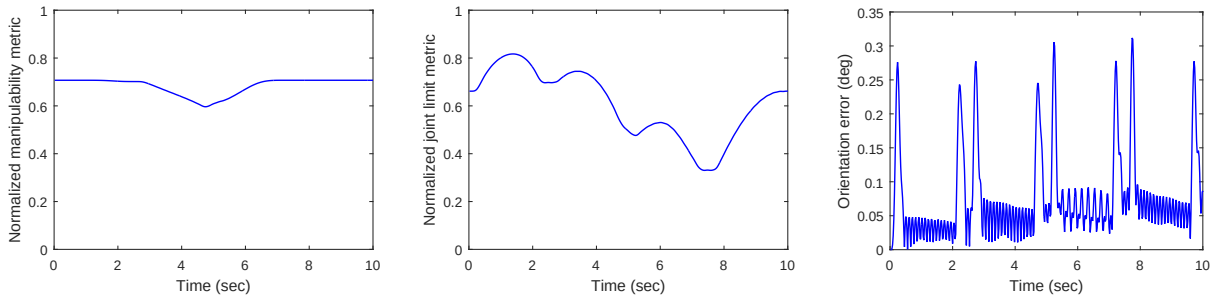

(a) Manipulability metric (b) Joint limit metric (c) Orientation error

Figure 2.13: Performance metrics during kinematic control.

Chapter 3

Development of a Passive Upper Limb Exoskeleton for Rhesus Macaques

3.1 Introduction

Based on the kinematic design and analysis presented in the previous chapter, this chapter presents the development of a non-motorized/passive upper limb exoskeleton for macaques. This passive exoskeleton prototype is first built for the purpose of kinematic motion sensing and animal training. Passive kinematic motion data acquisition needs to be investigated to directly characterize the motion of each macaque local joint (e.g., range of motion and joint speed limit), which will provide guidance to the actuation system design for the actuated exoskeleton development. Besides, an entirely passive training apparatus is also safe to operate for the animal subjects which have not ever been exposed to an exoskeleton-like wearable robot.

Since the device should be wearable and will be attached to the user's body segments, a list of requirements of developing such an apparatus is summarized as follows:

- Biomorphic nature joints: exoskeletons are wearable devices and should capture the motion of each individual joint.
- Compact: compactness is a necessity of an upper-limb exoskeleton that is designed for macaques. Since the body dimensions of macaques are much smaller than those of humans, the mechanical components of the exoskeleton should be kept sufficiently compact.
- Lightweight: since a passive device does not have actuators to compensate its gravity and inertia, the structures of the passive exoskeleton should be lightweight to avoid interfering the natural motion of the subjects.
- Firm attachment: considering that the two internal/external rotation joints of the upper arm and the forearm also serve as the attachment joints of the exoskeleton to

the user's body segments, and that the macaque's body is furry, firm attachments are required.

In this chapter, the development of a passive upper limb exoskeleton for macaques will be presented based on the above requirements. The mechanical design will be first introduced in terms of biomorphic joints and joint ranges of motion. Then real-time motion data acquisition and motion capture system based system kinematic calibration will be discussed. Finally experimental results of the animal test with the proposed passive exoskeleton will be provided.

3.2 Mechanical Design

The kinematic structural design of the passive exoskeleton follows the kinematic model proposed in Chapter 2, and the supporting and motion guidance mechanisms need to be carefully designed to accommodate the biological joint motion with the mechanical joint motion, i.e., to meet the anthropomorphic joints requirement. Fig. 3.1 shows the hardware design of the proposed passive upper limb exoskeleton.

3.2.1 Biomorphic Joints

Exoskeletons are supposed to be wearable, and thus the prosthetic joints of an upper limb exoskeleton can be classified into two types: one with rotation axis being perpendicular to the arm segments (Joint 1, 2, 3, and 5, Fig. 3.2a), and the other one with rotation axis being along the longitude of the arm segments (Joint 4 and 6, Fig. 3.2b). Two cuffs 3D-printed following macaque arm morphology are used to attach the exoskeleton to the macaque arm. In order to guarantee tight attachment, blood pressure cuffs are glued on the inner surface of the 3D-printed cuffs to prevent slippery motion between the exoskeleton and the user's body segments. An opening is left for each cuff for easy attachment as well as avoiding collision between the exoskeleton cuff and macaque body. A curved guide rail, a sliding roller with bearing groups, and a timing belt with pulley are mounted on the cuff to transmit the rotation motion of the upper arm and the forearm to the sensors.

3.2.2 Joint Ranges of Motion

Compared with human ADL ROM, most designed mechanical joint limits (listed in the last column of Table 3.1) meet the design requirements. The designed ROM of the elbow joint is restricted by the spacial limitations due to the mechanical collision between forearm and upper arm cuffs, but since the interested BMI task is prescribed as always in front of the macaque's coronal plane and generally does not involve elbow flexion of over 90°, the designed ROMs of each joint satisfy the specified requirements.

Human physiological and ADL ROMs are referenced (in the third and the fourth column of Table 3.1, averaged from [18, 65, 16]), which are sufficient to cover the workspace (in

Figure 3.1: Design of the proposed 6-DOF passive exoskeleton.

front of the coronal plane of macaque body) in the proposed BMI tasks. Additionally, it is assumed that the elevation/depression and protraction/retraction of the macaque shoulder are negligible during BMI task motions.

3.3 Real-Time Motion Data Acquisition

For real-time motion data acquisition, a target PC consisting of an NI FPGA board (NI 7851R) running real-time and FPGA modules is used for collecting the measurements of the encoders, and a host PC serves as a terminal for monitoring and analyzing the data acquisition process, as shown in Fig. 3.3.

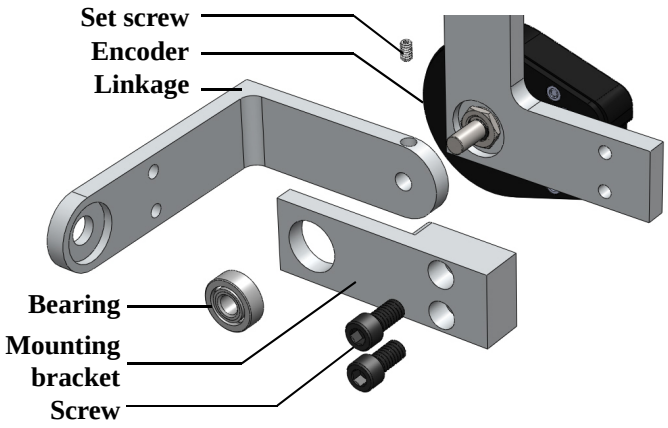

(a) Joint type I

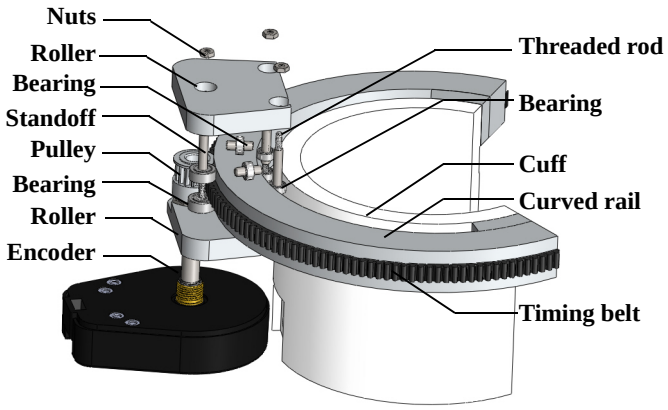

(b) Joint type II

Figure 3.2: CAD design of two types of joints.

Table 3.1: Human ROM and the designed mechanical limits.

Joint	Motion	Physical ROM	ADL ROM	Mechanical limit
1	Shoulder horizontal rotation	–	170°	191.0°
2	Shoulder adduction/abduction	182°	145°	276.6°
3	Shoulder flexion/extension	249°	110°	196.2°
4	Shoulder internal/external rotation	187°	150°	160.0°
5	Elbow flexion/extension	142°	140°	96.8°
6	Forearm internal/external rotation	190°	135°	160.0°

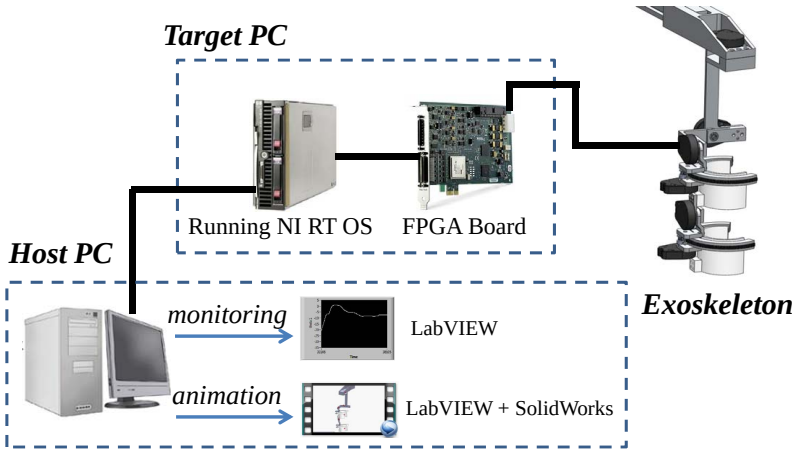

Figure 3.3: Structure of the real-time motion data acquisition of the passive exoskeleton system.

3.4 System Kinematic Calibration

Encoders are mounted on the proposed passive exoskeleton as the position sensors. Here the US Digital S6 incremental optical encoders are selected with 2500 counts per round for each joint, and encoder indices are utilized to indicate the reference positions.

For the current setup, position measurement error comes from two major sources – the unknown encoder value offsets at exoskeleton home posture and the kinematic model uncertainties. Kinematic calibration needs to be conducted to reduce the position measurement error. An external optical tracking system is a nice candidate for providing 3D position information as the reference values. By comparing the position data in the tracking system frame and the exoskeleton frame, the unknown variable values can be identified using an optimization-based approach. Note, this is an offline process, which only needs to be completed once before the exoskeleton is put into use.

3.4.1 Calibration Setup

Our optical tracking setup is the *PhaseSpace IMPULSE X2 Motion Capture System* consisting of ten cameras with a sampling rate of 480 Hz. This system can track its active LED markers and has sub-millimeter accuracy [67]. To acquire the position information of the exoskeleton, one marker was rigidly attached to the end point of the last link (Fig. 3.4). The end point was moved along some arbitrary trajectory in the task space during which all six joints were involved as much as possible. The positions of the marker were recorded by the motion capture system, and the joint space motions by each encoder. The sampling rate of the encoder reading is 1 kHz, and the two data acquisition systems were synchronized via the Network Time Protocol (NTP).

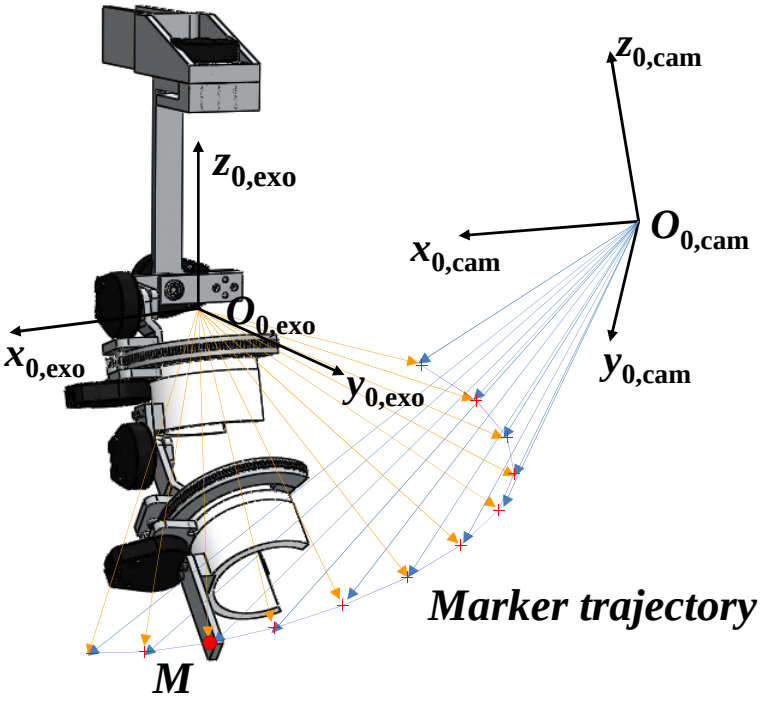

Figure 3.4: Illustration of synchronized data acquisition of the exoskeleton system and the motion capture system.

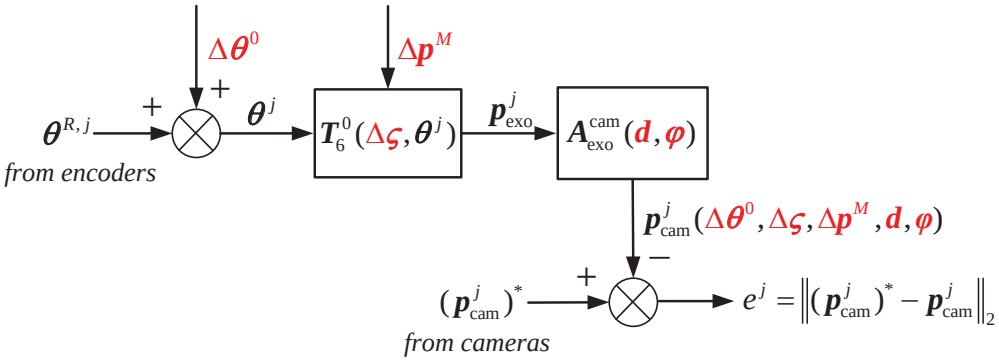

Figure 3.5: Block diagram of the calibration algorithm.

3.4.2 Calibration Algorithm

Calibration algorithm for the j-th sampling point is shown in Fig. 3.5 (variables in red are to be identified). Define $\Delta\boldsymbol{\theta}^0 \in \mathbb{R}^6$ as the vector of all six encoder offsets at exoskeleton's home posture. Together with the encoder readings $\boldsymbol{\theta}^{R,j}$, the joint space variable $\boldsymbol{\theta}^j$ can be

expressed as

$$\boldsymbol{\theta}^j = \Delta\boldsymbol{\theta}^0 + \boldsymbol{\theta}^{R,j}. \tag{3.1}$$

Introduce $\Delta\boldsymbol{p}^M \in \mathbb{R}^3$ as the marker's coordinates deviation from its nominal and actual value in the O_6-$x_6y_6z_6$ frame (following the definition in Fig. 2.3). Then the marker position in the exoskeleton's frame $\boldsymbol{p}^j_{\text{exo}}$ can be obtained via the coordinate transformation matrix $\boldsymbol{T}^0_6(\Delta\boldsymbol{\zeta}, \boldsymbol{\theta}^j)$ by forward kinematics, where $\Delta\boldsymbol{\zeta} := [\Delta d_2, \Delta d_3, \Delta d_5, \Delta a_3, \Delta a_5]^\top \in \mathbb{R}^5$ represents the vector of the concerned deviations of the exoskeleton nominal DH parameters from their actual values. Besides, as shown in Fig. 3.4, the relative posture between the camera frame and the exoskeleton frame is not exactly known, and thus two additional variables $\boldsymbol{d} \in \mathbb{R}^3$ and $\boldsymbol{\varphi} \in \mathbb{R}^3$ are introduced to represent the relative translations and rotations (Euler angles) between the two frames, respectively. The marker's coordinates in the camera frame $\boldsymbol{p}^j_{\text{cam}}(\Delta\boldsymbol{\theta}^0, \Delta\boldsymbol{\zeta}, \Delta\boldsymbol{p}^M, \boldsymbol{d}, \boldsymbol{\varphi})$ can be calculated through the frame transformation matrix $\boldsymbol{A}^{\text{cam}}_{\text{exo}}(\boldsymbol{d}, \boldsymbol{\varphi})$ with knowledge of the encoder information. On the other hand, the marker's coordinates in the camera frame $(\boldsymbol{p}^j_{\text{cam}})^*$ can be directly acquired by the cameras, which serve as the reference in this calibration process. Thus the position error is

$$e^j = ||(\boldsymbol{p}^j_{\text{cam}})^* - \boldsymbol{p}^j_{\text{cam}}(\Delta\boldsymbol{\theta}^0, \Delta\boldsymbol{\zeta}, \Delta\boldsymbol{p}^M, \boldsymbol{d}, \boldsymbol{\varphi})||_2. \tag{3.2}$$

Select N calibration points along the trajectory, and define

$$\boldsymbol{x} := [(\Delta\boldsymbol{\theta}^0)^\top, (\Delta\boldsymbol{\zeta})^\top, (\Delta\boldsymbol{p}^M)^\top, \boldsymbol{d}^\top, \boldsymbol{\varphi}^\top]^\top$$

as the parameter vector to be identified. Then the calibration algorithm can be cast as the following optimization problem

$$\begin{aligned} \min_{\boldsymbol{x}} \quad & \textstyle\sum_{j=1}^N ||(\boldsymbol{p}^j_{\text{cam}})^* - \boldsymbol{p}^j_{\text{cam}}(\boldsymbol{x})||_2^2 \\ \text{s.t.} \quad & x_i^L \le x_i \le x_i^U, \quad i = 1,\ 2, \ldots,\ 20, \end{aligned} \tag{3.3}$$

where x_i^L is the lower bound of the corresponding element, and x_i^U the upper bound. This is a typical nonlinear least squares problem, and can be solved using the `lsqnonlin` command in the MATLAB Optimization Toolbox [53].

3.4.3 Parameter Calibration and Analysis

Parameter Identification

400 data points are sampled in one experiment session for parameter training. Figure 3.6 shows the comparison between data fitting results before and after calibration with the blue lines representing the position errors. The identification results and initial guesses (nominal mechanical design values for system dimensions, and manually tested values for encoder offsets) are listed in Table 3.2. Before kinematic calibration, the root-mean-square (RMS) position error of the training dataset was 13.6 mm with the mean of 13.6 mm and standard deviation of 1.35 mm; and after kinematic calibration, the RMS position error of the same training dataset became 1.05 mm with the mean of 0.95 mm and standard deviation of 0.44 mm, which demonstrates the effectiveness of the proposed kinematic calibration approach.

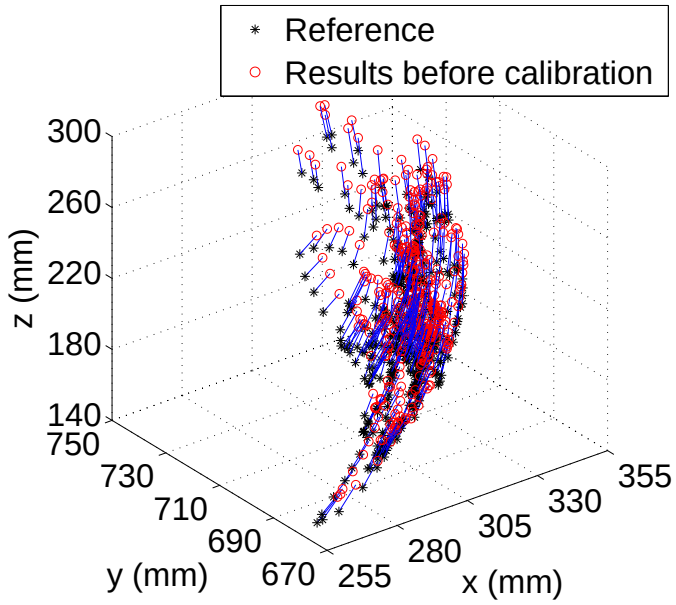

(a) Before calibration

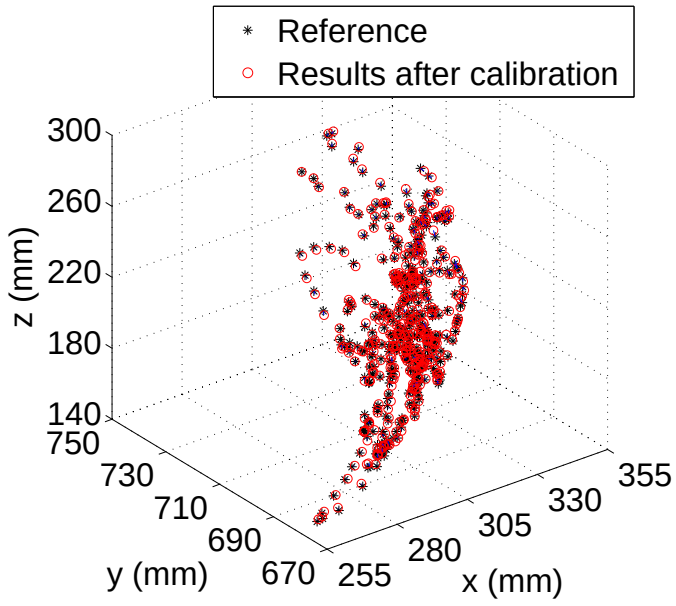

(b) After calibration

Figure 3.6: Sampled marker positions in the camera frame for reference data and generated data before/after calibration.

Table 3.2: Kinematic calibration results.

Parameter	Guess	Result	Parameter	Guess	Result
$\Delta\theta_1^0$ (deg)	30.7	31.85	Δa_5 (mm)	0	0.03
$\Delta\theta_2^0$ (deg)	−16.3	−17.60	Δp_x^M (mm)	0	−0.10
$\Delta\theta_3^0$ (deg)	−15.2	−13.45	Δp_y^M (mm)	0	−0.16
$\Delta\theta_4^0$ (deg)	−17.1	−17.19	Δp_z^M (mm)	0	−8.46
$\Delta\theta_5^0$ (deg)	−25.5	−22.11	d_x (mm)	203.2	203.29
$\Delta\theta_6^0$ (deg)	−2.3	−2.39	d_y (mm)	852.1	849.31
Δd_2 (mm)	0	−1.79	d_z (mm)	216.8	224.30
Δd_3 (mm)	0	−0.48	φ_x (deg)	−90.0	−89.01
Δd_5 (mm)	0	2.80	φ_y (deg)	0	−0.10
Δa_3 (mm)	0	−4.01	φ_z (deg)	−135.0	−135.52

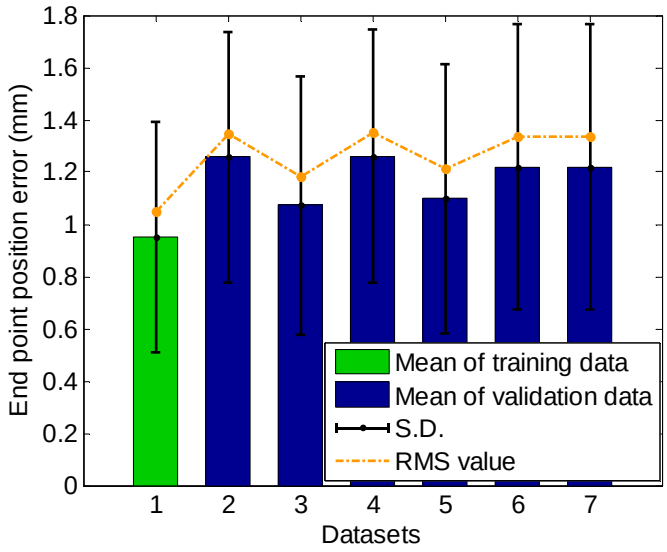

Figure 3.7: Position errors of both training and cross-validation datasets.

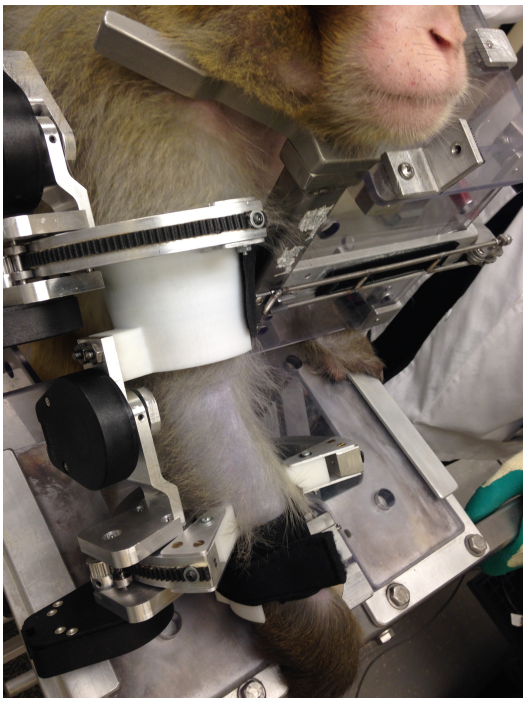

Figure 3.8: Experiment scene of a macaque wearing the proposed exoskeleton.

Cross-Validation

To evaluate the results, cross-validations were conducted using six datasets of 300 data points downsampled from other experimental sessions. Position errors of the cross-validation and the training datasets are given in Fig. 3.7. It can be noticed that the position errors of the cross-validation datasets are approximately the same level as the training dataset. Considering the accuracy levels of state-of-the-art neural decoders with virtual cursors [19, 79], the positioning accuracy of this exoskeleton is within acceptable levels.

3.5 Experimental Results of Animal Test

In order to verify the effectiveness of the proposed exoskeleton system, animal tests of a self-feeding task were performed with one adult male rhesus macaque. All procedures were conducted in compliance with the National Institute of Health Guide for Care and Use of Laboratory Animals and were approved by the University of California, Berkeley Institutional Animal Care and Use Committee. Fig. 3.8 shows the experiment scene of an able-bodied macaque wearing the proposed exoskeleton. Some food was presented in front of the macaque, and the macaque voluntarily performed the reaching, grasping, and finally self-feeding motion. The linkages of the exoskeleton were made of thin aluminum bars and the cuffs were 3D-printed using acrylonitrile butadiene styrene (ABS). Thus it is considered

Table 3.3: Measured macaque ROM in reach-grasp-feed task.

Joint	Motion	ROM
1	Shoulder horizontal rotation	30.9°
2	Shoulder adduction/abduction	5.1°
3	Shoulder flexion/extension	75.3°
4	Shoulder internal/external rotation	39.9°
5	Elbow flexion/extension	84.7°
6	Forearm internal/external rotation	54.9°

that the entire passive exoskeleton is light enough for the macaque to operate, which can be observed during the animal's self-feeding motion. Besides, a compression spring was used to connect the second linkage and the beam of the exoskeleton frame to help the exoskeleton maintain in its home position (gravity compensation) when no subject was attached.

A total of twenty-five trials were performed within seven minutes. Fig. 3.9 shows the joint space trajectories of all six joints for a period of 150sec. Table 3.3 lists the measured ROMs of all six DOFs during the twenty-five trials, which indicates that the ROM of each joint provided by the exoskeleton (see Table 3.1) is sufficient for the designed task. Fig. 3.10 shows the time series of the normalized manipulability metric of the shoulder joint for six trials within 150 seconds. Notice that the normalized manipulability metric remained at a high level, which demonstrates the manipulation flexibility of the proposed shoulder joint during the animal training tasks.

Fig. 3.11 and Fig. 3.12 plot the joint space position and speed trajectories of all six joints for one trial, and a 3D task space trajectory of the macaque palm is presented in Fig. 3.13 for more intuitive visualization by performing the forward kinematics to the joint space motion measurements (assuming rigid wrist joint), which matched the actual motion well and supported the effectiveness of the proposed exoskeleton system.

3.6 Chapter Summary

This chapter presented the development of a passive upper limb exoskeleton for macaques which serves as a kinematic motion sensing and a safe animal training device prior to the development of an actuated exoskeleton system.

The mechanical design and the fabricated exoskeleton was first introduced, and the design requirements of biomorphic joints, compactness, light weight, and firm attachment were also addressed. Real-time data acquisition of the exoskeleton system was set up, and approximately 2mm end point position sensing accuracy was achieved by kinematic calibration, which is sufficient for the neurophysiology applications. Animal tests were conducted in the scenario of a reach-grasp-feed task. The effectiveness of the proposed exoskeleton system was demonstrated by both joint space measurements and task space trajectory visualiza-

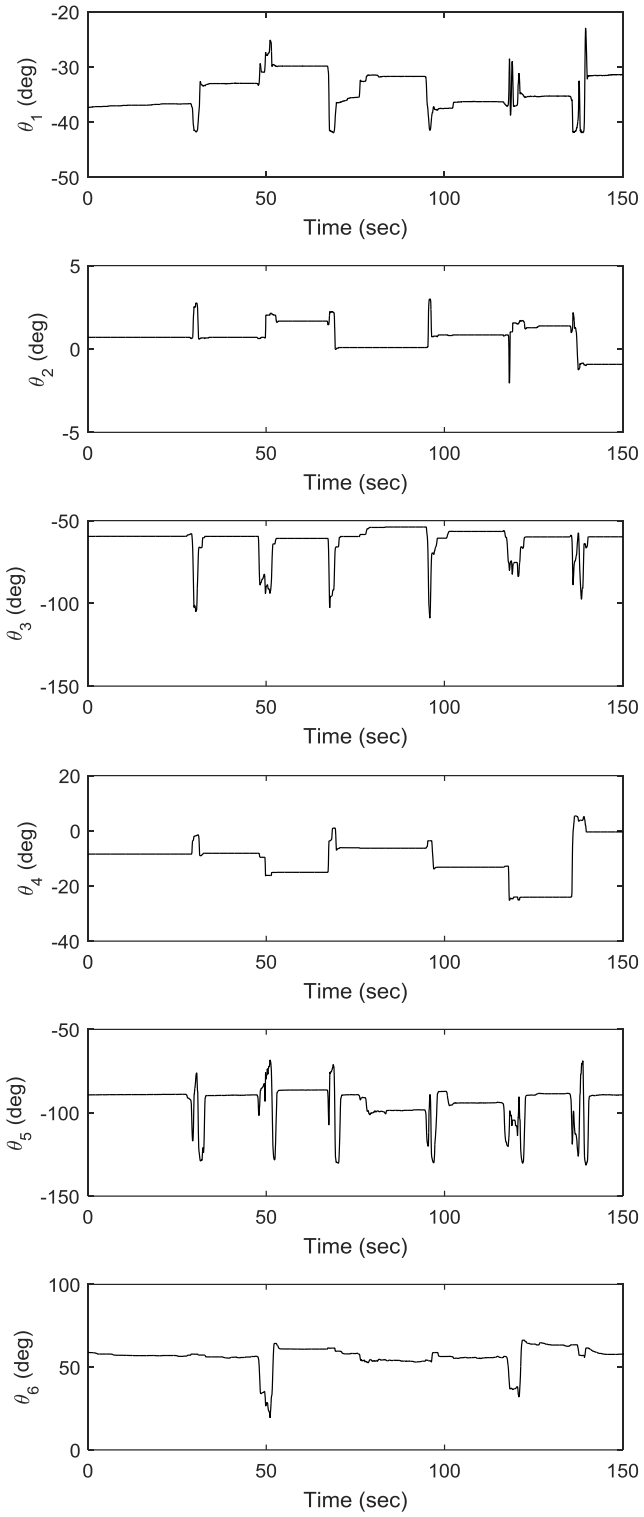

Figure 3.9: Joint space trajectories of six trials within 150 seconds.

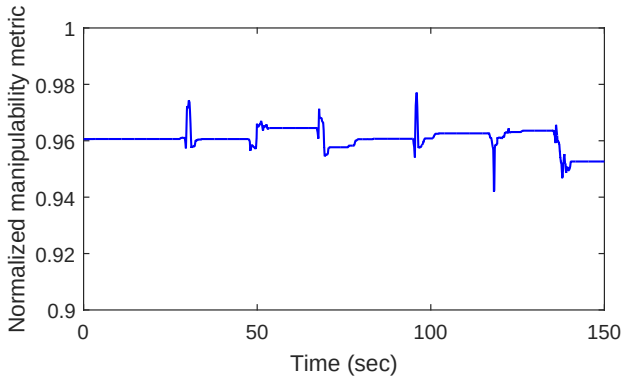

Figure 3.10: Normalized manipulability metric of the shoulder joint for six trials within 150 seconds.

tion. The motion sensing functionality of the proposed exoskeleton helps analyze the motion characteristics in the sense of each individual joint of the upper limb, which will provide guidance for the actuated exoskeleton design in Chapter 5.

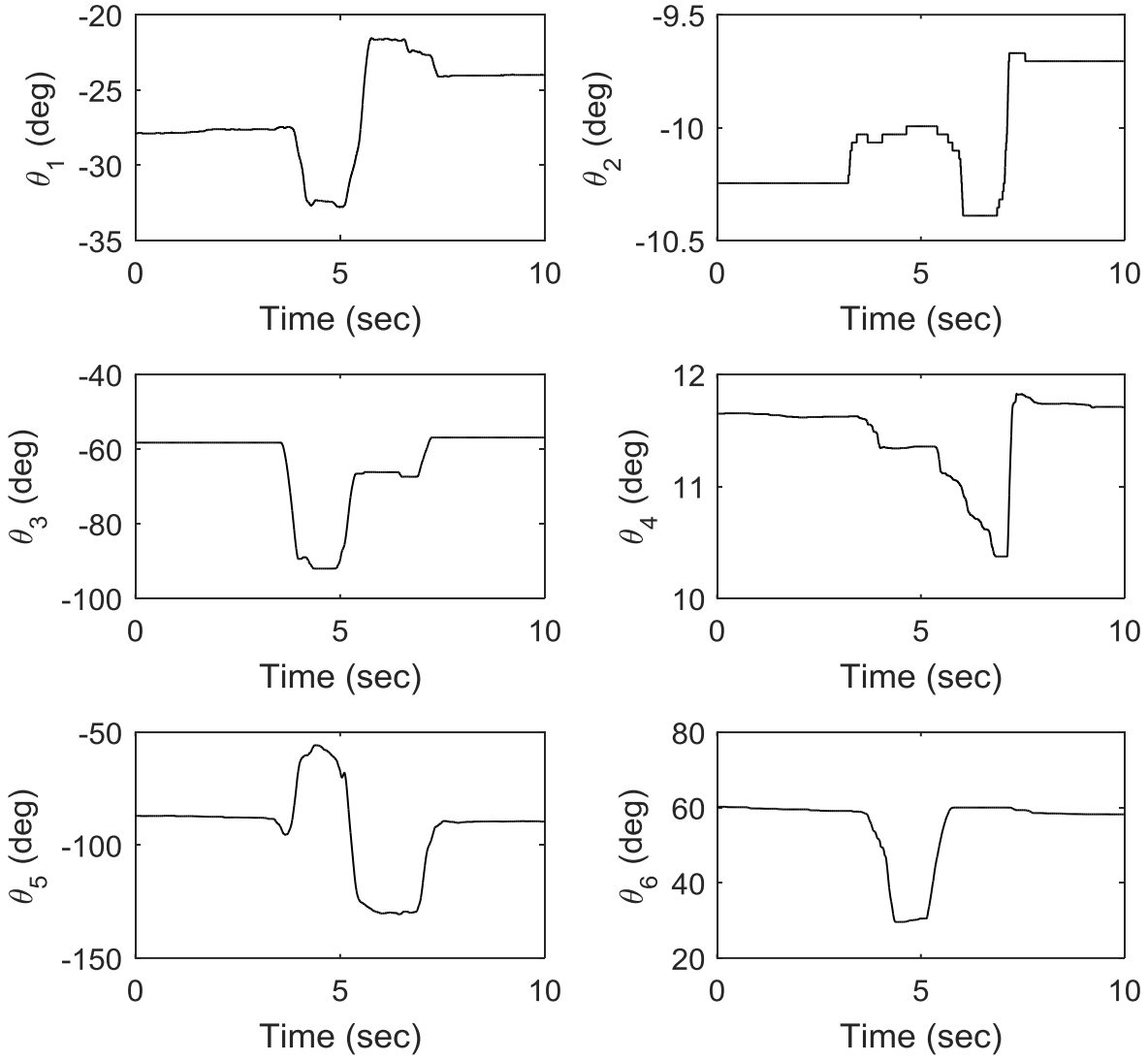

Figure 3.11: Joint space trajectory of the reach-grasp-feed task for one trial.

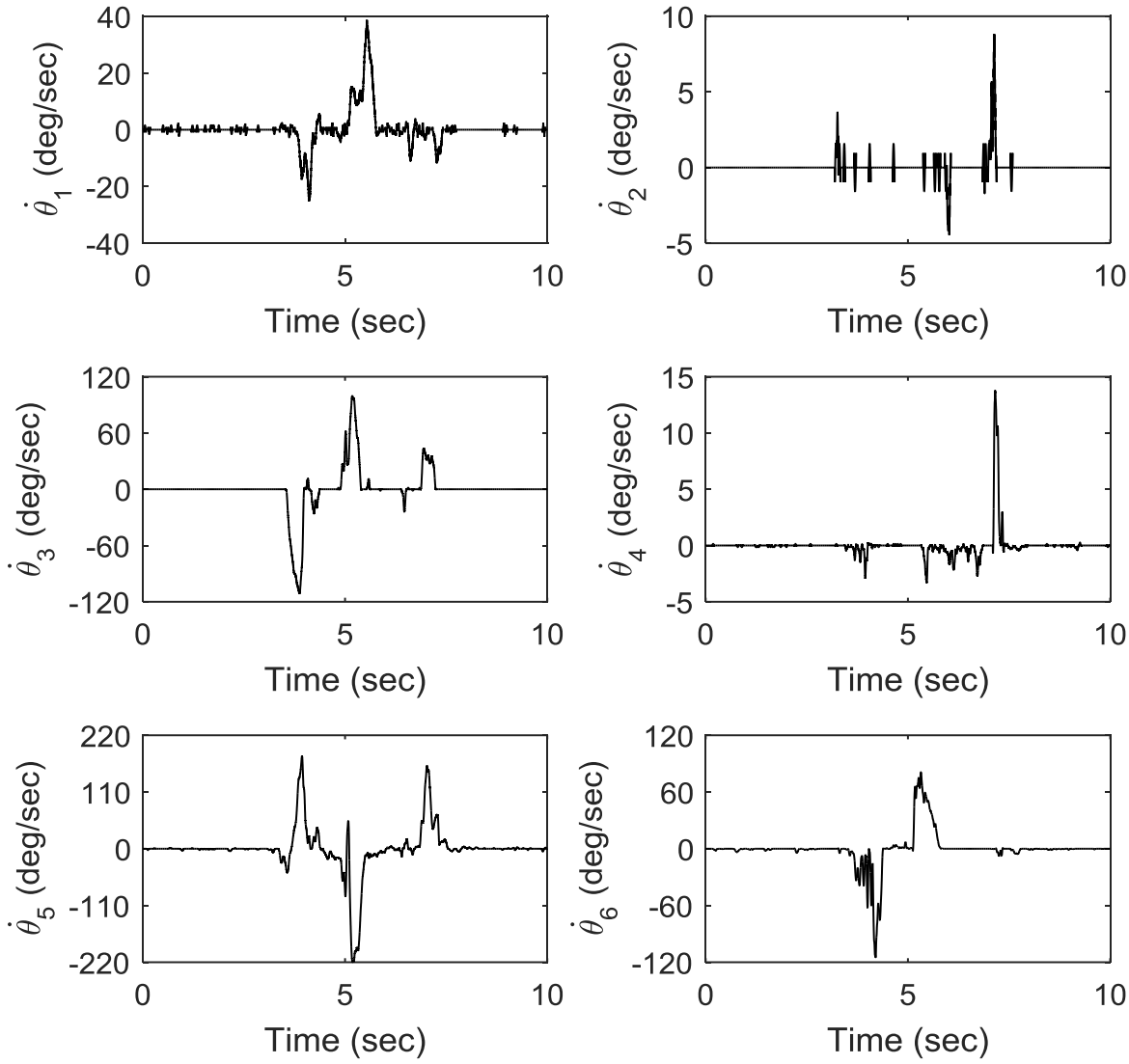

Figure 3.12: Joint space speed of the reach-grasp-feed task for one trial.

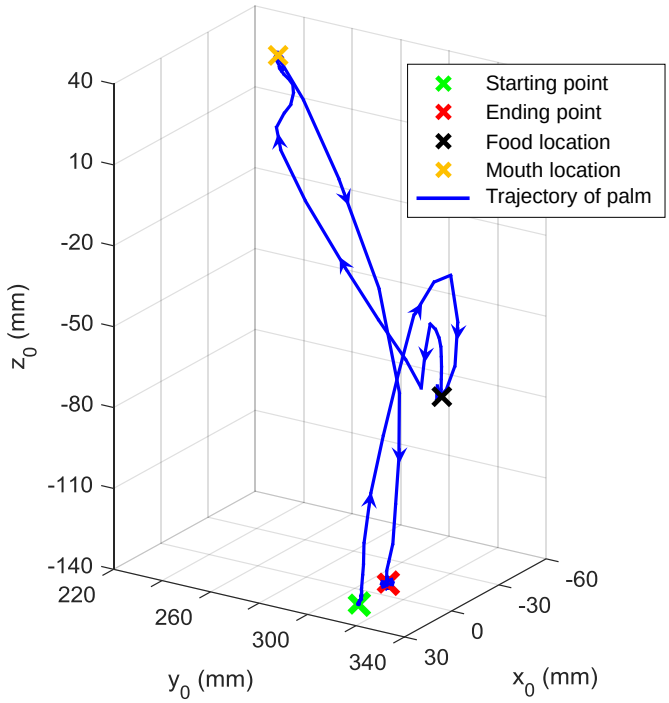

Figure 3.13: Task space trajectory of the macaque palm for one trial. The palm was initially placed on the primate table, and the macaque started to reach the food, grasped and fed itself when some food was placed in front of it, and finally placed its palm back on the table. The coordinate system $O_0{-}x_0y_0z_0$ follows the convention in Fig. 2.3, and the macaque sat facing the positive direction of the y_0 axis.

Chapter 4

Design and Control of a Cable-Driven Series Elastic Actuator

4.1 Introduction

The actuation system plays a key role in the development of an actuated exoskeleton. The safety issue is far more critical than non-continuous-contact subject-robot applications since the user's body segments are embedded in the exoskeleton. Compared with the actuation systems used in traditional industrial robots, soft or compliant actuation will be considered for this continuous contact application. Compliant actuation refers to the robot's ability to adjust its motion and interaction force by the states of the environment with which it interacts. Generally speaking, compliant actuation can be achieved at both the hardware and the software/algorithm level.

On the hardware level, the actuator should be designed to be backdrivable, force/torque-reflecting, compact and lightweight. The series elastic actuator (SEA) proposed in [69] is a nice candidate which meets the backdrivable and torque-reflecting requirements. It decouples the motor side and the load side by an elastic component which introduces an intrinsic compliance in the actuator. Thus with an appropriately selected elasticity, an SEA can be regarded as backdrivable even if the motor is geared with a high reduction reducer. Moreover, the output force/torque of an SEA can be evaluated by Hooke's law based on position sensor measurements on both sides. For applications of SEAs in upper/lower extremity exoskeleton designs, most SEAs impose the motor on the user's body [39, 70, 38, 75], which will increase the inertia of the overall system and also reduce the system compactness on the user's side. To achieve a lightweight and compact design, [84] proposes a Bowden cable driven SEA which is able to avoid attaching the geared motors on the user's body. In this case, the geared motor can be installed on a fixed base and the driving force is transmitted through the Bowden cable to the actuator's load side. One challenge with this design is to account for the variable friction on the Bowden cable [40].

On the algorithm level, the impedance controller proposed in [28] provides a systematic

method to regulate the robot force and motion in the form of virtual mechanical impedance. Since "compliance" can also be understood as the inverse of impedance, this approach enables a way to create the user-defined virtual compliance accommodating to different tasks. Most existing literature on impedance control of SEA use the proportional-derivative form (PD form) impedance controllers to regulate the SEA output force and the deviation of the robot's actual position from the desired virtual reference [68, 81, 62, 6], instead of regulating the interaction force to the target impedance. They work well for applications where robots interact with high stiffness environment (e.g., the ground). However, in applications where the robots interact with humans, impedance controllers which regulates the interaction force to the target impedance can generate more accurate haptic sensation of the desired impedance to the users. Hogan introduced an impedance control approach for contact tasks in [27]. Based on this work, an interactive impedance control algorithm of the cable-driven SEA will be proposed in this chapter to realize direct regulation of the interaction torque to a desired mechanical impedance.

This chapter presents the development of a cable-driven SEA which will be used for motion actuation of the actuated exoskeleton. The cable-driven mechanism in the proposed actuator helps achieve a more compact subject side design, and the interactive impedance control algorithm helps realize a safe motion actuation when the user is in the loop.

4.2 Mechanical Design of Cable-Driven SEA

Fig. 4.1 shows the hardware setup of the proposed cable-driven SEA. The joint side mechanism (Fig. 4.1a) is attached to the subject elbow joint, and the driving torque generated by the geared motor (Fig. 4.1b) is transmitted to the joint side through a Bowden cable to affect the joint side motion. The torsional spring between the motor side and the joint side acts as an energy buffer and a torque sensor.

The cable-driven mechanism helps avoid attaching the motor to the subject, and thus helps achieve a compact and lightweight actuator design. The motor is installed on a stationary base and the driving force from the motor is transmitted through the cables to the subject joint. The Bowden cable, which is difficult to extend but easy to wind, is selected for our application. To reduce backlash, a pair of barrel adjusters are used for adjusting the preload cable tension. One big challenge of introducing the Bowden cable is to deal with the variable friction between its tendon and sheath [40], and this will be detailed in Section 4.4.

4.3 System Modeling and Interactive Impedance Control

Interactive impedance control regulates the interaction torque τ_{int} between the robot and the user with respect to their motions as a form of virtual mechanical impedance. In impedance control there is always a desired virtual reference θ_d that specifies the desired load side

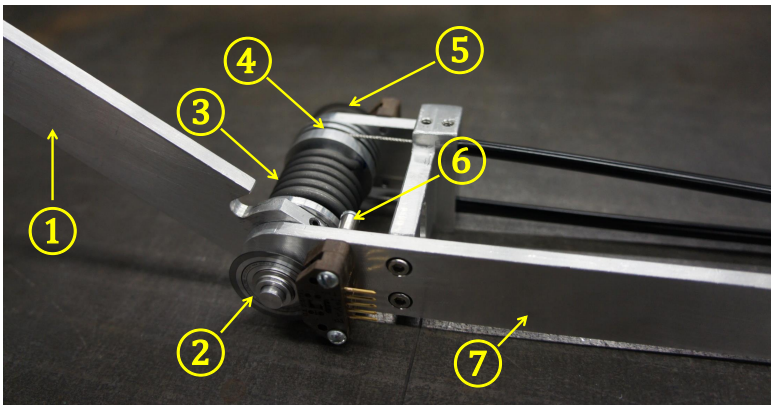

(a) Joint load side design consisting of: ① moving linkage, ② load side encoder, ③ torsional spring, ④ joint side pulley, ⑤ joint pulley side encoder, ⑥ mechanical stop, ⑦ fixed linkage.

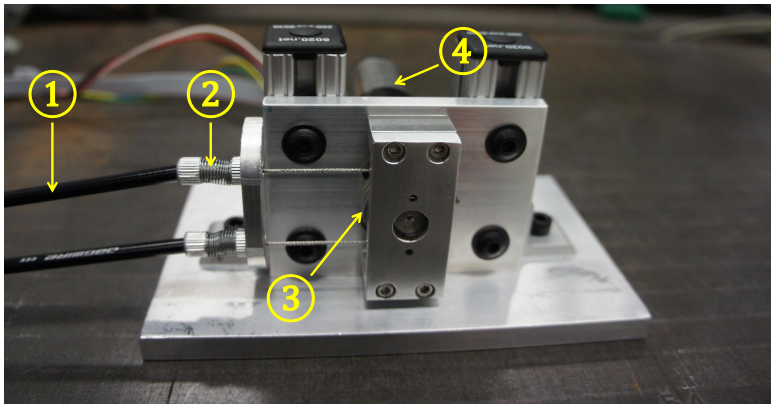

(b) Motor side design consisting of: ① Bowden cable, ② barrel adjuster, ③ gearbox pulley, ④ geared motor with optical encoder.

Figure 4.1: Hardware setup of the proposed Bowden cable-driven SEA.

trajectory, and deviation in the actual robot load side trajectory θ_ℓ from this virtual reference will result in interactive torque τ_{int}. Thus the target interactive impedance is generally in the following form [68]:

$$\tau_{\text{int}} = J^d(\ddot{\theta}_d - \ddot{\theta}_\ell) + B^d(\dot{\theta}_d - \dot{\theta}_\ell) + K^d(\theta_d - \theta_\ell) + \tau^d_{\text{offset}}, \tag{4.1}$$

where J^d, B^d, K^d and τ^d_{offset} are virtual impedance parameters representing the desired virtual inertia, virtual damping, virtual stiffness, and virtual offset torque, respectively. Fig. 4.2 shows an illustration of a subject interacting with a virtual impedance.

In this section, system modeling of the proposed actuator and the subject it interacts with will be first presented, and then follows the overall architecture of the interactive impedance control system.

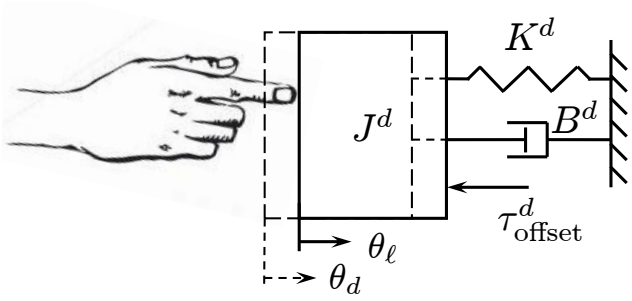

Figure 4.2: Illustration of interacting with a virtual impedance.

4.3.1 System Modeling

Fig. 4.3 shows a schematic of the cable-driven SEA labeled with key kinematic and kinetic quantities. The equations of motion of the system are:

Geared motor side:

$$J_m\ddot{\theta}_m + \tau_{fr,m} + \tau_{fr,gm} = u - \tau_{\text{gear,in}}, \tag{4.2}$$

$$J_g\ddot{\theta}_g + \tau_{fr,gb} + \tau_{\text{cable,in}} = \tau_{\text{gear,out}}, \tag{4.3}$$

$$\tau_{\text{gear,out}} = N \cdot \tau_{\text{gear,in}}, \tag{4.4}$$

$$\theta_m = N \cdot \theta_g, \tag{4.5}$$

where J_m, J_g are the inertia of the motor and the gearbox; $\tau_{fr,m}$, $\tau_{fr,gm}$ and $\tau_{fr,gb}$ are the friction torque of the motor, the gear meshing and the bearing on the gearbox side, respectively; $\tau_{\text{gear,in}}$ and $\tau_{\text{gear,out}}$ are the gearbox input and output torque; $\tau_{\text{cable,in}}$ is Bowden cable torque at the motor side before cable transmission; θ_m and θ_g are the angular displacements of the motor and the gearbox; u is the input torque command to the current-controlled motor, and N is the gearbox reduction ratio.

Cable transmission:

$$\tau_{\text{cable,in}} = \tau_{\text{cable,out}} + \tau_{fr,\text{cable}}, \tag{4.6}$$

$$\tau_{\text{cable,out}} = \tau_{\text{SEA}} + \tau_{fr,\text{pulley}}, \tag{4.7}$$

$$\tau_{\text{SEA}} = k_{\text{spring}}(\theta_{jp} - \theta_\ell), \tag{4.8}$$

$$\theta_{jp} = (r_{gp}/r_{jp}) \cdot \theta_g, \tag{4.9}$$

where $\tau_{\text{cable,out}}$ is Bowden cable torque at the joint side after cable transmission; $\tau_{fr,\text{cable}}$ is the friction torque on the Bowden cable which highly depends on the curvature of the cable sheath (i.e., bend radius) [34]; $\tau_{fr,\text{pulley}}$ is the friction torque at the joint-side pulley; τ_{SEA} is the actuator's output torque to the joint load side by the torsional spring; θ_{jp} and θ_ℓ are the angular displacements of the joint side pulley and the joint load side; r_{jp} and r_{gp} are the radii of the joint-side pulley and the gearbox pulley, and k_{spring} is the spring stiffness coefficient.

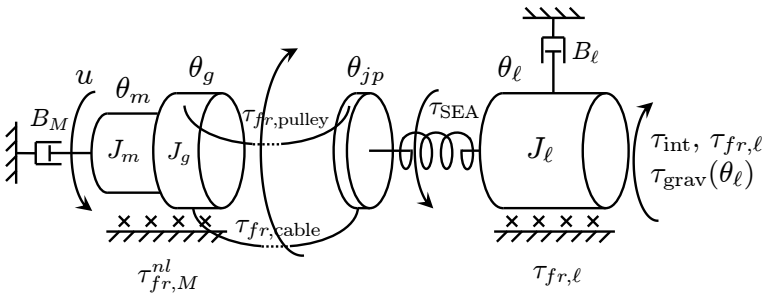

Figure 4.3: Schematic representation of the actuator.

Joint load side:

$$J_\ell \ddot{\theta}_\ell + B_\ell \dot{\theta}_\ell + \tau_{\text{grav}}(\theta_\ell) + \tau_{fr,\ell} = \tau_{\text{SEA}} - \tau_{\text{int}}. \tag{4.10}$$

where J_ℓ, B_ℓ, θ_ℓ, $\tau_{\text{grav}}(\theta_\ell)$, $\tau_{fr,\ell}$, and τ_{int} are the joint load side inertia, damping, angular displacement, gravity torque, Coulomb friction torque, and the interaction torque with the subject, respectively.

Subject side:

$$J_s \ddot{\theta}_s + B_s \dot{\theta}_s + \tau_{\text{grav}}(\theta_s) = \tau_s - \tau_{\text{int},s}. \tag{4.11}$$

where J_s and B_s are general forms of the subject body segment inertia and damping; θ_s, $\tau_{\text{grav}}(\theta_s)$ and τ_s are the subject angular displacement, gravity torque and muscle torque, respectively; and $\tau_{\text{int},s}$ is the interaction torque reflected on the subject joint.

Eq. (4.2) $\sim$ (4.5) yield

$$J_M \ddot{\theta}_m + \tau_{fr,M} = u - \frac{1}{N}\tau_{\text{cable,in}}, \tag{4.12}$$

where $J_M := J_m + J_g/N^2$ and $\tau_{fr,M} := \tau_{fr,gb}/N + \tau_{fr,m} + \tau_{fr,gm}$ represent the equivalent inertia of the geared motor and the equivalent friction torque referred to the motor side, respectively. Considering the feasibility of implementation, it is reasonable to group several friction torques together as an equivalent one reflected on the motor side for modeling and estimation [12]. To characterize the friction torque, the following model is used [2]

$$\tau_{fr,M} = B_M \dot{\theta}_m + \tau_{fr,M}^{nl}, \tag{4.13}$$

where B_M is the damping coefficient with respect to the motor speed $\dot{\theta}_m$, and $\tau_{fr,M}^{nl}$ includes all the nonlinear friction.

Fig. 4.4 shows the block diagram of the actuator system including the external interaction torque. u is the driving force of the motor side loop (denoted as L_1), and the resultant torque $\tau_{\text{SEA}} - \tau_{\text{int}}$ is the driving force of the joint load side loop (denoted as L_2); the two loops are connected by the torsional spring. $\tau_{fr,M}^{nl}$ and $\tau_{fr,\text{cable}} + \tau_{fr,\text{pulley}}$ can be regarded as the disturbances to the system, which should be rejected by the controllers.

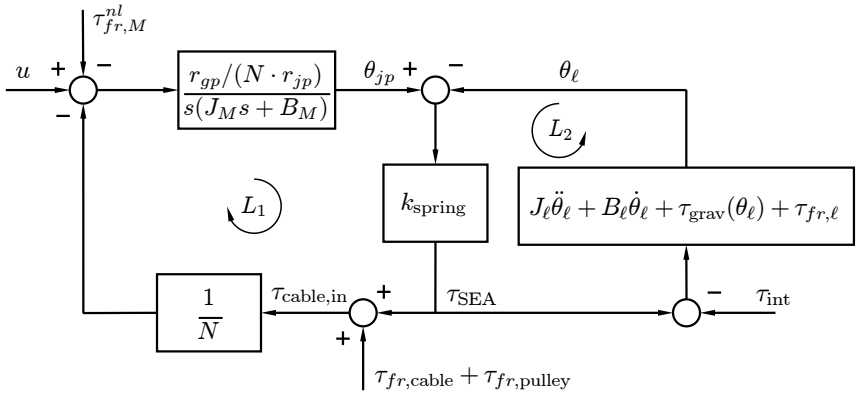

Figure 4.4: Block diagram of the actuator's coupled motor side and load side.

4.3.2 Interactive Impedance Control Architectures

Generally there are two ways of regulating the interaction torque τ_{int} under the interactive impedance control framework.

One approach is to control the load side position (θ_ℓ) first, and then feedback the measured joint torque (τ_{SEA}) to the impedance controller[1] to produce a desired position deviation ($\Delta\theta$) between the desired virtual trajectory and the robot's current position states, and finally realize the desired robot position feeding into the position controller by comparing the desired position deviation and the desired virtual trajectory (θ_d), as shown in Fig. 4.5a. This is a position based impedance control framework, and requires the inner position control loop to have sufficiently large bandwidth. However, SEA load side position is subject to external disturbance due to the inclusion of a compliant element between the load side and the motor side. High fidelity position control typically needs a high gain controller, but SEAs tend to become unstable under direct high gain position control [25]. Thus the bandwidth of such inner loop position control will be limited.

Another method uses a fast torque controller in the inner loop to reject the disturbance torques and control the joint torque (τ_{SEA}) to the desired value (τ_d), and then feedback the robot's current position (θ_ℓ) into an outer impedance controller to generate the desired torque, as shown in Fig. 4.5b. Throughout this dissertation, this torque based architecture will be adopted for implementation. For cascade controller design, typical rule of thumb is to make the inner loop have a bandwidth five times larger than the outer loop such that the two loops can be designed separately to avoid the difficulty of tuning both controllers simultaneously. Considering that application of the actuator is for motion actuation in a BMI system, in which motion frequency is much slower than that of typical human or macaque monkey's natural motion, a 2Hz bandwidth[2] for the outer interactive impedance control loop

[1] In this case, the impedance controller is also called an *admittance controller*.

[2] In fact the outer loop is a nonlinear system, and the *bandwidth* here is a generalized concept.

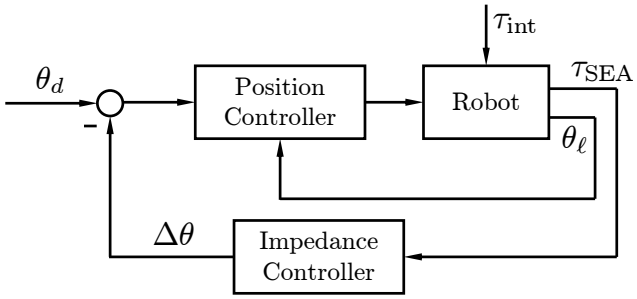

(a) Position based impedance control.

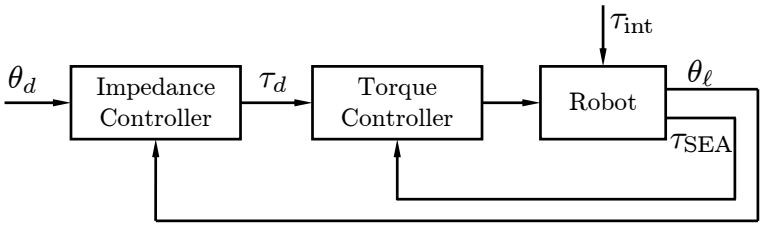

(b) Torque based impedance control.

Figure 4.5: Two types of impedance control frameworks.

is aimed at, and thus the designed bandwidth for the inner torque control loop will be 10Hz.

Fig. 4.6 shows the overall control system of the actuator, where

$$d := -\tau_{fr,M}^{nl} - \frac{1}{N}\left(\tau_{fr,\text{cable}} + \tau_{fr,\text{pulley}}\right) \tag{4.14}$$

is the equivalent disturbance, and

$$G(s) := \frac{NP(s)}{k_{\text{spring}}P(s) + N} \tag{4.15}$$

is the equivalent plant to be controlled with $P(s) := \frac{r_{gp}/(N \cdot r_{jp})}{s(J_M s + B_M)}$. The inner loop corresponds to the L_1 loop in Fig. 4.4, and the outer loop corresponds to the L_2 loop.

4.4 Torque Controller Design

Per the discussions in last section, the inner torque control loop in Fig. 4.6 needs to be designed much faster than the outer impedance control loop. Thus the L_2 loop can be regarded as cut open, and θ_ℓ can be treated as a known external reference to the L_1 loop. The goal of designing a torque controller is to realize the fast tracking of τ_{SEA} to τ_d.

Since the friction on the Bowden cable is significant and sheath profile dependent [34, 40], as well as the cable is mobile in practical applications, the rejection of such variable friction is challenging to achieve high fidelity torque control of the cable-driven SEA. Disturbance

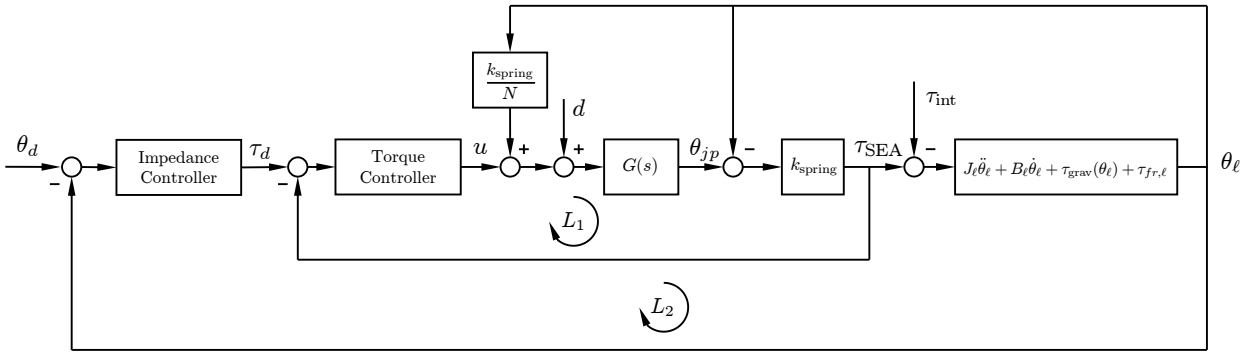

Figure 4.6: Block diagram of the overall control system.

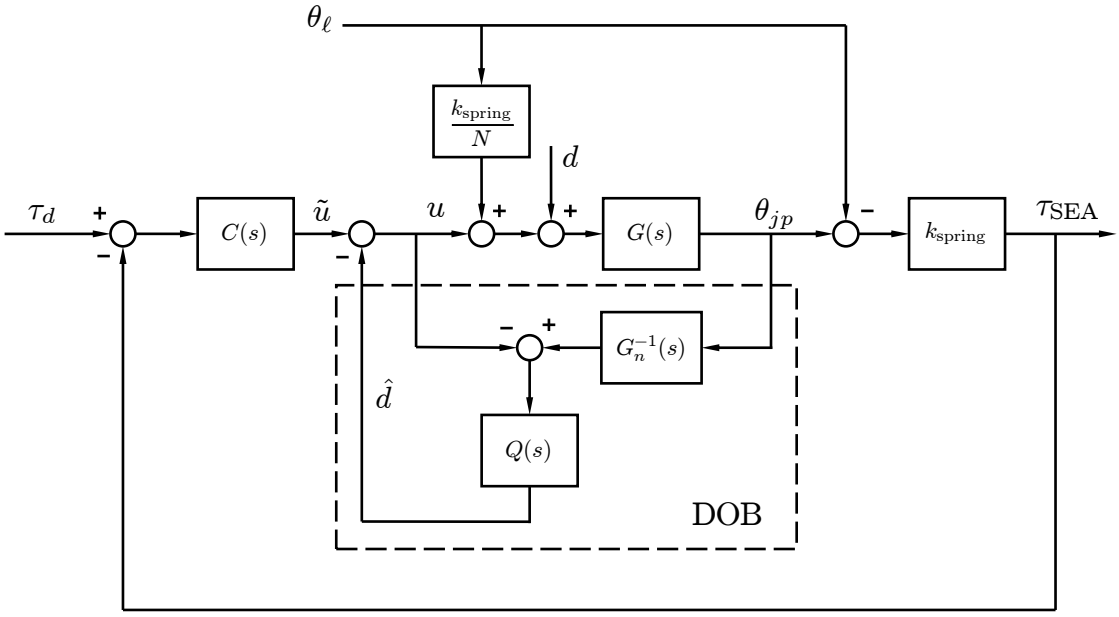

Figure 4.7: Block diagram of the DOB based torque-mode control system.

observer (DOB) has the nice properties of robust disturbance rejection and the ability of shaping the actual plant to the nominal plant model at specific frequency range[61, 35], thus a DOB based torque control algorithm is proposed in this work.

4.4.1 DOB Based Torque Controller

Fig. 4.7 shows the block diagram of the proposed DOB based torque-mode control system where $Q(s)$ is a low-pass filter to be designed, and the nominal plant model to be controlled

is defined as

$$G_n(s) = \frac{NP_n(s)}{k_{\text{spring}}P_n(s) + N} = \frac{Nr_{gp}}{N^2 r_{jp} J_M s^2 + N^2 r_{jp} B_M s + k_{\text{spring}} r_{gp}}, \tag{4.16}$$

where $P_n(s)$ is the nominal model of $P(s)$, and $G_n(s)$ is directly invertible since it is stable and minimum phase.

Note that the load side motion $\theta_\ell k_{\text{spring}}/N$ also enters the equivalent plant $G(s)$ in the disturbance channel. Since θ_ℓ is measurable, the effect of $\theta_\ell k_{\text{spring}}/N$ can be compensated using a feedforward compensation. Thus we now have

$$G_{\tilde{u}\theta_{jp}}(s) = \frac{GG_n}{G_n + Q(s)\,(G - G_n)}, \tag{4.17}$$

$$G_{d\theta_{jp}}(s) = \frac{GG_n\,(1 - Q(s))}{G_n + Q(s)\,(G - G_n)}. \tag{4.18}$$

In the low frequency region where $Q(s) \approx 1$, we have $G_{\tilde{u}\theta_{jp}}(s) \approx G_n(s)$ and $G_{d\theta_{jp}}(s) \approx 0$, which indicates that the DOB makes the dynamics from $\tilde{u}$ to θ_{jp} behave like the nominal plant and rejects low frequency disturbances. The DOB loop (from $\tilde{u}$ to θ_{jp}) was then stabilized by an outer controller $C(s)$ to meet the performance requirements such as bandwidth.

To investigate the stability robustness of the DOB loop, assume that there is a multiplicative uncertainty $\Delta(s)$ between the actual and the nominal equivalent plant

$$G(s) = G_n(s)\,(1 + \Delta(s))\,. \tag{4.19}$$

By small gain theorem, the DOB loop will be stable if [35]

$$||\Delta(j\omega)Q(j\omega)||_\infty < 1. \tag{4.20}$$

4.4.2 Identification of Geared Motor Damping

We know from (4.13) that the geared motor damping can be included in the equivalent friction torque $\tau_{fr,M}$, and thus the identification of B_M is turned into a problem of friction torque identification of the geared motor. (4.12) shows that $\tau_{fr,M}$ will exactly be equal to the input torque command of the motor u if the unloaded geared motor is running at a constant speed. Fig. 4.8 plots the experimentally measured friction torques (reflected to the motor side before gearbox) at different motor side speeds which well matches the static friction model with the Stribeck effect [1] as follows

$$\tau_{fr,M} = \sigma\dot{\theta}_m + \left(\tau_{CL} + (\tau_{st} - \tau_{CL})e^{-(\dot{\theta}_m/\dot{\theta}_{SB})^2}\right)\text{sgn}(\dot{\theta}_m), \tag{4.21}$$

where σ, τ_{CL}, τ_{st} and $\dot{\theta}_{SB}$ represent the damping coefficient, the Coulomb friction, the static friction and the Stribeck speed, respectively; and $\text{sgn}(\cdot)$ is the signum function.

Table 4.1: Identified parameters with different step input levels.

Step input level ($\times 10^{-3}$N·m)	J_M (kg·m^2)	β_M (N·m·sec/rad)
$1.22 \rightarrow 1.94$	1.85×10^{-6}	5.50×10^{-6}
$1.22 \rightarrow 2.19$	1.86×10^{-6}	5.31×10^{-6}
$1.22 \rightarrow 2.43$	1.85×10^{-6}	5.53×10^{-6}

By applying a nonlinear least squares fitting, the identified parameters are $\sigma = 8.022 \times 10^{-7}$N·m·sec/rad, $\tau_{CL} = 2.384 \times 10^{-3}$N·m, $\tau_{st} = 1.425 \times 10^{-3}$N·m, $\dot{\theta}_{SB} = 130.75$rad/sec. This friction model cannot be directly used for friction compensation since this approach is not able to satisfactorily identify τ_{st} and $\dot{\theta}_{SB}$; however, the estimation of σ is generally of high quality [1, 12]. Moreover, considering the reduction ratio $N = 132$, the nonlinear friction torque after the gearbox will be approximately 0.3N·m, which is significant in our application. This is also why the nonlinear friction term is treated as a disturbance and the DOB is used to reject such friction as discussed in previous sections.

The damping of the geared motor B_M can be directly assigned to be σ as identified above. However, when taking a close look at Fig. 4.8 it can be noticed that σ matches the geared motor damping in the high speed region (> 200rad/sec, known as *quasi-linear domain at hight speed* [1]) well rather than that in the low speed region (< 200rad/sec). In this case, one natural way would be gain scheduling, which adjusts the damping coefficient in the nominal model according to the speed region. This however introduces the controller complexity and stability issue during parameter switching. Alternatively, a uniform damping value as a trade-off between the low and high speed regions can be adopted, although model mismatch would occur accordingly. Further discussions about the selection of damping will be detailed in Section 4.4.4.

4.4.3 Identification of the Inertia of the Geared Motor

The inertia of the geared motor J_M is identified by investigating the step responses from the input torque u to the unloaded motor side speed $\dot{\theta}_m$. To overcome the static friction τ_{st}, the step responses were collected by starting at $u = 1.22 \times 10^{-3}$N·m and ending at 1.94×10^{-3}, 2.19×10^{-3}, 2.43×10^{-3}N·m, respectively. Then J_M was identified by estimating the transfer function $1/(J_M s + \beta_M)$ using the `tfest` function in the MATLAB System Identification Toolbox [54].

Table 4.1 shows the identified inertia and damping of the geared motor with different step input levels. It turns out that the identified inertia values are quite consistent. Since the step input levels are selected to generate a steady-state speed in the low motor speed region, the identified dampings match Fig. 4.8 well.

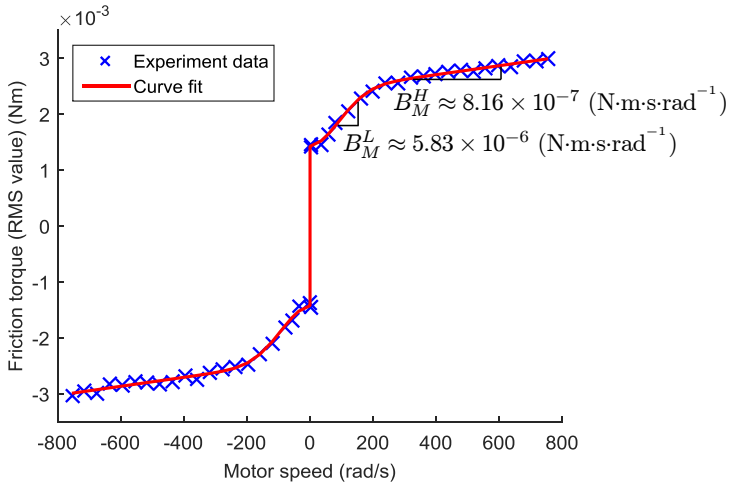

Figure 4.8: Steady-state speed-friction characteristic of the geared motor (reflected to the motor side before gearbox).

4.4.4 Controller Design and Stability Analysis

Design of $C(s)$

Generally the controller $C(s)$ is designed before the Q-filter based on the nominal model $G_n(s)$. In this work the $C(s)$ is selected as a PD controller. To ensure the requirements of robust stability and bandwidth, the PD gains are set to be $K_P = 0.052$, and $K_D = 0.023$. The controller is digitally implemented using the LabVIEW Real-Time Operating System (National Instrument) with a sampling rate of 1kHz.

Design of Q-filter

The low-pass filter $Q(s)$ is selected to be a third-order binomial filter [43]

$$Q(s) = \frac{3(\tau s) + 1}{(\tau s)^3 + 3(\tau s)^2 + 3(\tau s) + 1}, \tag{4.22}$$

where $\tau = 2\pi/w_c$ with ω_c being its desired cutoff frequency.

To guarantee the stability of the DOB loop, it is required by (4.20) that the magnitude of the Q-filter should always be smaller than that of the inverse of the multiplicative uncertainty. In this work we assume that the only source of uncertainty is introduced by the difference of the damping value B_M in the low motor speed region and in the high speed region, as is discussed in Section 4.4.2. Under this assumption, the multiplicative uncertainty $\Delta(s)$ can be expressed as

$$\Delta(s) = \frac{N^2 r_{jp}(B_M^n - B_M^{[\cdot]})s}{N^2 r_{jp} J_M s^2 + N^2 r_{jp} B_M^{[\cdot]} s + k_{\text{spring}} r_{gp}}, \tag{4.23}$$

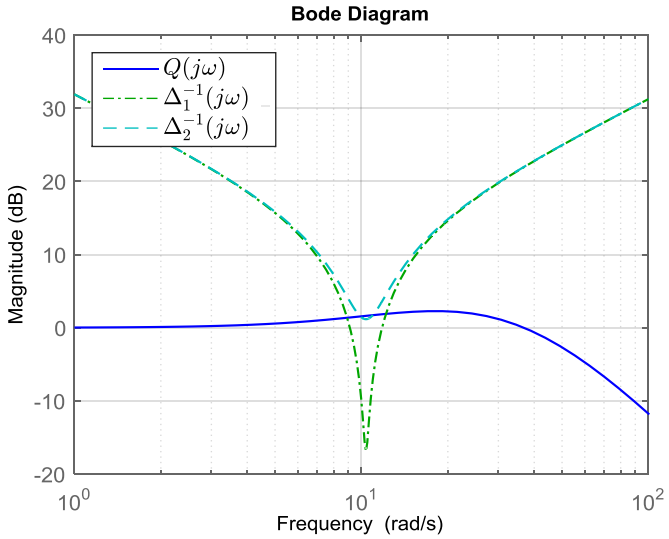

(a) Using either B_M^L or B_M^H

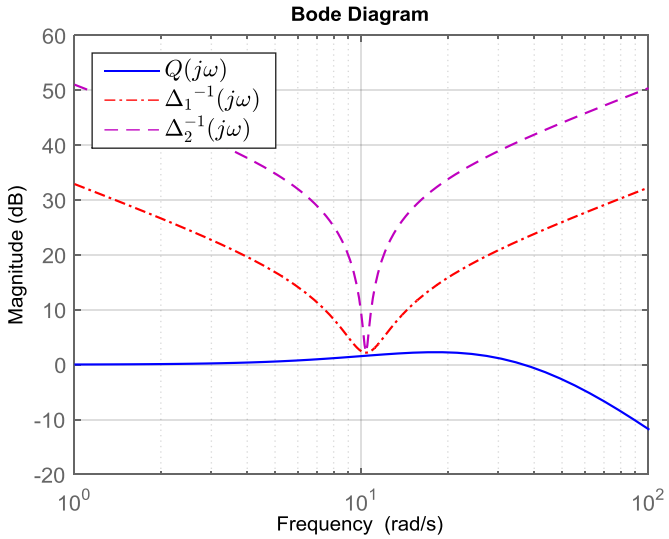

(b) Using an intermediate B_M

Figure 4.9: Multiplicative uncertainty and Q-filter (cutoff frequency selected as 5Hz).

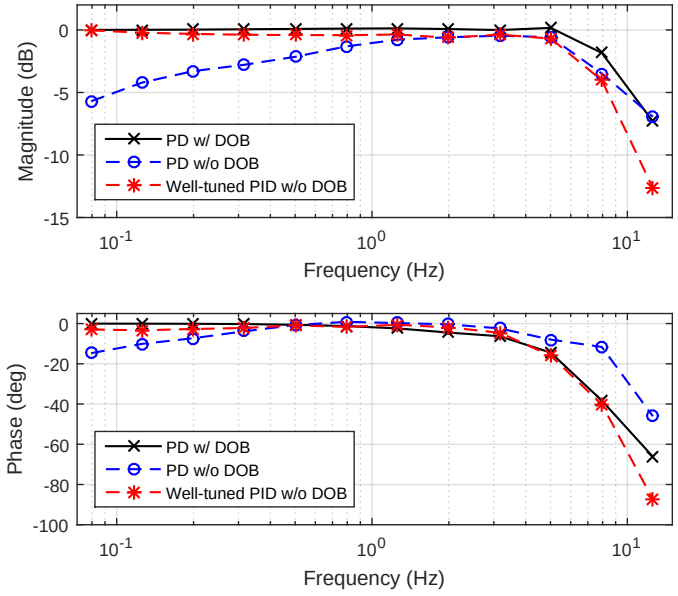

Figure 4.10: Comparison of frequency responses of closed-loop transfer function $\tau_{\text{SEA}}(s)/\tau_d(s)$ (straight cable).

where B_M^n is the selected nominal damping coefficient, and $B_M^{[\cdot]}$ represents the damping coefficient either in the low speed region (B_M^L) or in the high speed region (B_M^H).

Fig. 4.9a shows the relationship between $||Q(j\omega)||$ and $||\Delta^{-1}(j\omega)||$ in the case of directly using either B_M^L or B_M^H. It can be noticed that when $B_M^n = B_M^L$, the resulting $\Delta_1^{-1}(j\omega)$ due to B_M^H already crosses the Q-filter curve; if we assign $B_M^n = B_M^H$, the resulting $\Delta_2^{-1}(j\omega)$ overlaps with the Q-filter as well. Then an intermediate value is selected as $B_M^n = 1.37 \times 10^{-6}\text{N·m·s·rad}^{-1}$, and the relationship between $||Q(j\omega)||$ and $||\Delta^{-1}(j\omega)||$ is shown in Fig. 4.9b, from which we can see that the stability condition is satisfied.

4.4.5 Performance Analysis of Torque Controller

In order to verify if the proposed torque controller meets the design requirements, the closed-loop frequency responses from the desired torque reference to the actual SEA output $\tau_{\text{SEA}}(s)/\tau_d(s)$ (fixing θ_ℓ at a constant angle) are identified with the proposed DOB based PD controller, PD controller (using the same gain) without DOB, and a well-tuned proportional-integral-derivative controller (PID controller) without DOB when the cable was straight, respectively. Fig. 4.10 indicates that compared with the two non-DOB based controllers, the proposed DOB based approach produced improved performance due to its enhanced ability of suppressing disturbances, and the bandwidth was also increased to around 9Hz which can be regarded as having met the design goal.

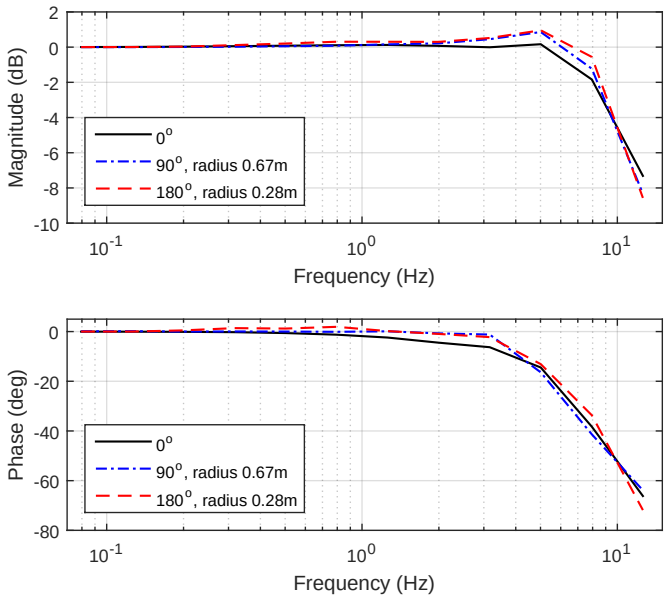

Figure 4.11: Frequency responses of closed-loop transfer function $\tau_{\text{SEA}}(s)/\tau_d(s)$ under different cable bent angles with DOB based torque controller.

To investigate the effect of different cable profiles on the torque controller performance, frequency responses of $\tau_{\text{SEA}}(s)/\tau_d(s)$ were identified under different cable bend angles (and radii) with the same proposed DOB based controller. Fig. 4.11 shows that system performances were slightly degraded in the high frequency domain due to the changed cable curvature, while remained similar performance to the straight cable situation in the low frequency domain, which supports the effectiveness of the proposed torque controller.

4.5 Impedance Controller Design

Now that a fast inner loop torque controller with sufficiently large bandwidth has been developed, τ^d_{SEA} can be considered as the direct control input to the outer interactive impedance control loop, i.e., $\tau_{\text{SEA}} = \tau^d_{\text{SEA}}$. The goal is to directly regulate the interaction torque between the actuator's load side and the human, as well as to achieve a 2Hz position tracking bandwidth when there is no interaction.

4.5.1 Interactive Impedance Controller

Remember that the outer loop dynamics is described in Eq. (4.10), and applying feedback linearization to Eq. (4.10) with Eq. (4.1) yields the interactive impedance control law [27]

$$\tau_{\text{SEA}} = \left(1 - J_\ell (J^d)^{-1}\right) \tau_{\text{int}} + J_\ell (J^d)^{-1} \Big[J^d \ddot{\theta}_d + B^d (\dot{\theta}_d - \dot{\theta}_\ell) + K^d (\theta_d - \theta_\ell) + \tau^d_{\text{offset}} \Big] + B_\ell \dot{\theta}_\ell + \tau_{\text{grav}}(\theta_\ell) + \tau_{fr,\ell}. \tag{4.24}$$

When there is no interaction, i.e., $\tau_{\text{int}} = 0$, Eq. (4.24) indeed is the well-known *computed torque* controller which realizes position control to track the reference trajectory θ_d. However, in general interaction control scenarios, since there is no force sensor feeding back τ_{int} at the interface between the actuator's load side and the user, a force sensor-less approach is needed. One way to get rid of the τ_{int} term in Eq. (4.24) is to set the desired virtual inertia $J^d = J_\ell$, and then the interactive impedance control law reduces to

$$\tau_{\text{SEA}} = J^d \ddot{\theta}_d + B^d (\dot{\theta}_d - \dot{\theta}_\ell) + K^d (\theta_d - \theta_\ell) + \tau^d_{\text{offset}} + B_\ell \dot{\theta}_\ell + \tau_{\text{grav}}(\theta_\ell) + \tau_{fr,\ell}, \tag{4.25}$$

where $J^d = J_\ell$.

Compared with the PD-form impedance controller adopted by [68, 81, 62, 6], i.e.,

$$\tau_{\text{SEA}} = B^d (\dot{\theta}_d - \dot{\theta}_\ell) + K^d (\theta_d - \theta_\ell) + \tau_{\text{grav}}(\theta_\ell), \tag{4.26}$$

the interactive impedance controller Eq. (4.25) has a virtual inertia term with which to realize interface force sensor-less control, as well as the term $B_\ell \dot{\theta}_\ell + \tau_{fr,\ell}$ to compensate the load side damping and Coulomb friction in a feedforward manner. In this way, Eq. (4.25) makes it possible to directly regulate the interaction torque. Note that since Eq. (4.25) includes feedforward terms $B_\ell \dot{\theta}_\ell + \tau_{\text{grav}}(\theta_\ell) + \tau_{fr,\ell}$, this approach needs the load side dynamics to be well identified during implementation.

4.5.2 Stability Analysis

When there is no interaction between the robot and the subject, asymptotic tracking stability of the proposed controller can be guaranteed if $J^d, B^d, K^d > 0$ and $\tau^d_{\text{offset}} = 0$ [76]. However, when there is interaction between the robot and the subject, the stability analysis of the coupled system is generally difficult since the subject's dynamics is complicated. Without loss of generality, let us consider the most interactive scenario where the actuator is attached to the subject body and shares the same motion with the subject, for example, in the exoskeleton application. In this case, we have $\theta_s = \theta_\ell$ and $\tau_{\text{int},s} = -\tau_{\text{int}}$. Assume the desired offset impedance compensates the gravity torque of the subject body segment nicely (i.e., $\tau^d_{\text{offset}} = \tau_{\text{grav}}(\theta_s)$) and the subject inertia and damping coefficient are time-invariant, then Eq. (4.10), (4.11) and (4.25) yield

$$J_s \ddot{\theta}_s + B_s \dot{\theta}_s = J^d (\ddot{\theta}_d - \ddot{\theta}_s) + B^d (\dot{\theta}_d - \dot{\theta}_s) + K^d (\theta_d - \theta_s) + \tau_s, \tag{4.27}$$

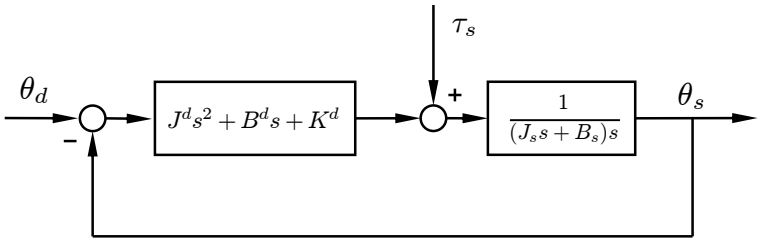

Figure 4.12: Block diagram of the coupled subject-actuator system under impedance control.

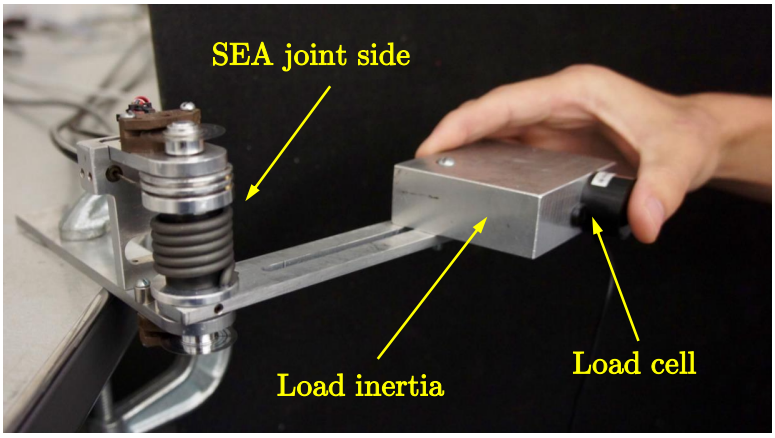

Figure 4.13: Experiment scene of human interacting with the actuator.

which is illustrated in Fig. 4.12. The closed-loop transfer function from subject muscle torque τ_s to the shared position θ_s is

$$\Phi_{\tau_s \theta_s} = \frac{1}{(J^d + J_s)s^2 + (B^d + B_s)s + K^d}, \tag{4.28}$$

which indicates that the coupled system is always stable if τ_s is bounded, and B^d and K^d are positive ($J^d = J_\ell$).

4.6 Experimental Results and Analysis

To verify the effectiveness of the proposed interactive impedance controller, a load inertia was attached to the moving linkage, and the damping and Coulomb friction torque of the load side were experimentally identified. Table 4.2 lists the parameters that were used in the experiments, and Fig. 4.13 shows the scene of a male human subject interacting with the actuator. One load cell was attached at the interaction interface which only provided contact force measurements for verification rather than for feedback controls. Experiments were

Table 4.2: Parameters used in interactive impedance control.

Parameter	Value	Unit
J_M	1.85×10^{-6}	kg·m^2
B_M	1.37×10^{-6}	N·m·sec/rad
k_{spring}	3.49	N·m/rad
N	132	unitless
r_{jp}	0.0254	m
r_{gp}	0.0254	m
K_P	0.052	N·m/rad
K_D	0.023	N·m·sec/rad
τ	0.2	sec
J_ℓ	7.9×10^{-3}	kg·m^2
B_ℓ	0.0355	N·m·sec/rad
$\tau_{fr,\ell}$	4.4×10^{-3}	N·m

conducted running the actuator in three interactive control modes: moderate impedance control interacting with human, zero impedance control interacting with human, and impedance control without interaction.

4.6.1 Moderate Impedance Control

Fig. 4.14 shows the experimental result of a constant desired virtual reference tracking under human disturbance. We can notice that at the onset of human disturbance, the load side angle θ_ℓ started deviating from the reference, and the SEA output torque τ_{SEA} started increasing at the same time due to position deviation; after the subject released the load side, θ_ℓ recovered to the reference again. Meanwhile, the inner loop torque controller was able to accurately generate the desired SEA output torque.

4.6.2 Equivalent Position Control

Fig. 4.15 shows the sine signal tracking results with 1Hz and 2Hz, respectively. No human interaction was applied, and the proposed impedance controller enforced position control. It can be noticed that after transient behaviors, both cases have stabilized tracking performance. The RMS tracking error of the 1Hz signal tracking was 1.2deg under moderate impedance gains. For the 2Hz signal tracking, the ratio of the output-input signal magnitude was 0.763 (-2.35dB), which indicates that the outer loop impedance controller satisfies the bandwidth design requirement.

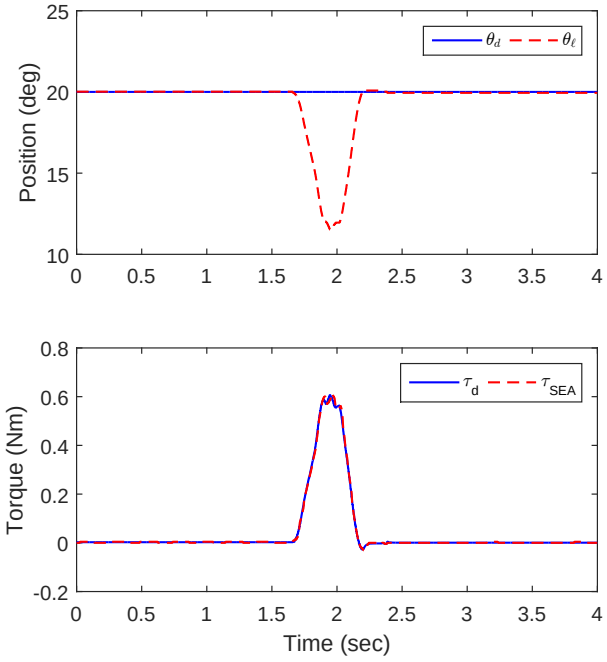

Figure 4.14: Interaction control with subject under moderate impedance control ($J^d = J_\ell$, $B_d = 0.1$N·m·sec/rad, $K_d = 4.0$N·m/rad, $\tau^d_{\text{offset}} = 0$).

4.6.3 Zero Impedance Control

Fig. 4.16 presents the zero impedance controlled load side interacting with the subject using two different outer impedance controllers. Both two approaches use the same inner torque controller. Since there was no gravity force to compensate, the PD-form controller became $\tau^d_{\text{SEA}} = 0$, and the proposed controller $\tau^d_{\text{SEA}} = B_\ell \dot{\theta}_\ell + \tau_{fr,\ell}$, i.e., in both cases, the impedance controller reduces to a torque controller. The subject applied arbitrary motion moving the load side with increasing motion frequencies. The RMS SEA output torques were 0.0278N·m and 0.0447N·m for the PD-form controller and the proposed controller, respectively. However, the RMS contact force measured by the load cell at the interaction interface were 0.183N and 0.082N, respectively, which meant that the proposed approach regulated the interaction impedance much closer to zero than the conventional one with an improvement of 55%. This is because with the feedforward compensation term, the subject did not have to overcome the damping and Coulomb friction at the load side on his own, which also indicates that the PD-form impedance controller does not directly regulate the interaction torque.

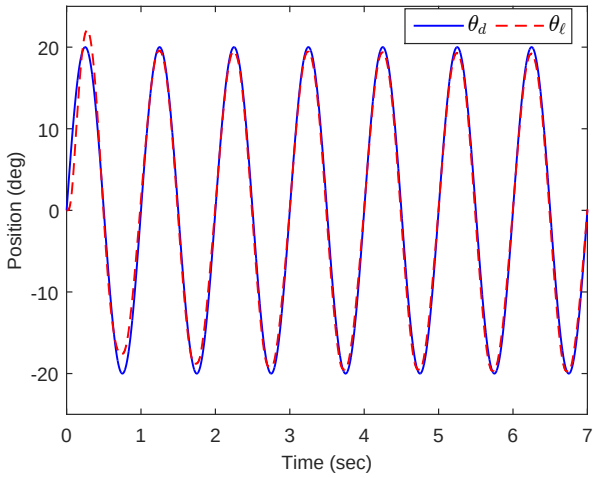

(a) 1Hz signal tracking.

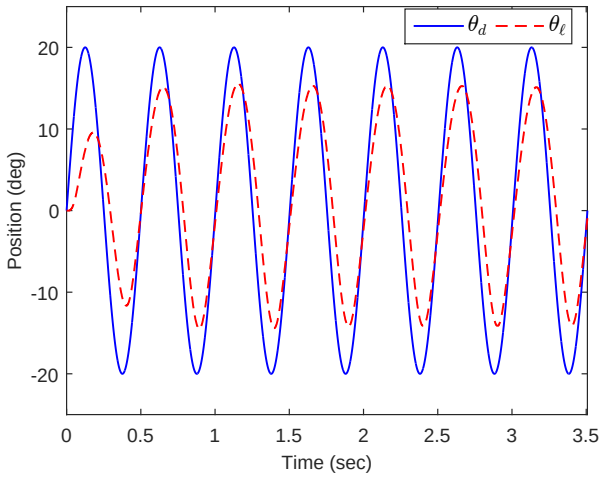

(b) 2Hz signal tracking.

Figure 4.15: Equivalent position control under no interaction ($J^d = J_\ell$, $B_d = 0.05$ N·m·sec/rad, $K_d = 1.5$ N·m/rad, $\tau^d_{\text{offset}} = 0$).

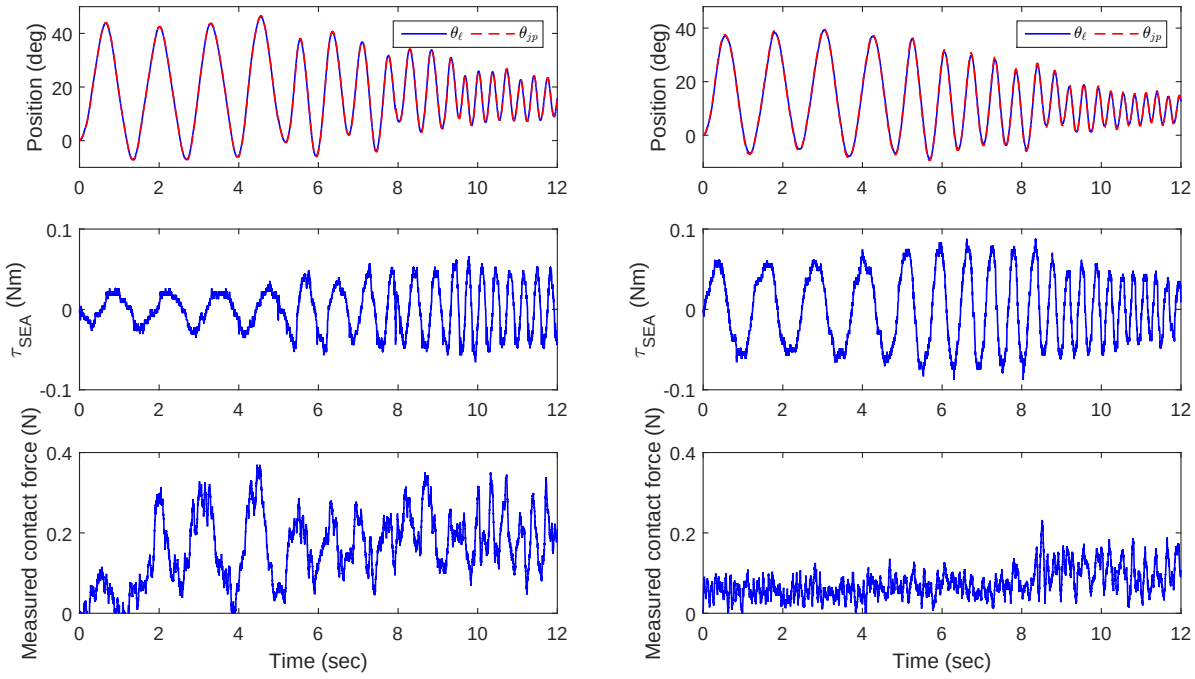

(a) PD-form controller (Eq. (4.26)).

(b) Proposed controller (Eq. (4.25)).

Figure 4.16: Zero impedance control with two different controllers.

4.7 Chapter Summary

This chapter presented a torque based interactive impedance control algorithm of a cable-driven SEA interacting with a subject. Torque-mode control is fundamental to SEA, but the introduction of the cable-driven transmission makes it more challenging due to the presence of variable cable friction. A DOB based torque controller was proposed and successfully rejected the friction at the motor side and on the cable transmission simultaneously. Compared with conventional approach, the proposed algorithm significantly improved torque tracking performance and exhibited large system bandwidth. Based on such fast inner loop torque control, an outer loop interactive impedance controller was designed to regulate the interaction torque between the actuator's load side and the subject. Considering that the conventional PD-form impedance controller only regulates the SEA output torque, the proposed approach has the advantage of being able to directly characterize the impedance behavior between the interaction torque and the load side motion. The effectiveness of the proposed control algorithm was verified by a series of experiments with and without the interaction with a human subject.

The proposed torque based impedance control approach is also applicable to the non-

cable-driven scenarios, and the entire controller design process does not depend on the information from the subject side. Besides, under different conditions, the impedance controller may reduce to a position controller or a torque controller. Specifically, the impedance controller becomes a position controller when there is no interaction between the robot and the environment, and becomes a torque controller when the virtual impedance parameters are all zeros.

Chapter 5

Development of an Actuated Upper Limb Exoskeleton for Rhesus Macaques

5.1 Introduction

On top of the development of the passive exoskeleton and the cable-driven SEA presented in the previous chapters, this chapter investigates the development of an actuated upper limb exoskeleton for rhesus macaques.

The functionalities of the upper limb exoskeleton in the BMI system include both data acquisition and motion actuation. Apart from the design requirements of biomorphic joints, compactness, light weight, and firm attachment that are listed in Chapter 3, the following requirements also need to be addressed:

- Shoulder joint design with unlikely singularity in workspace: as previously discussed, the shoulder joint of an upper limb exoskeleton should be designed with unlikely internal singularities (i.e., singular configurations not due to reaching joint limits) in the workspace for both large joint ROM and safety considerations.
- High power-to-weight ratio: the exoskeleton should be lightweight while capable of providing sufficient output torque to complete the designed tasks, which means that the exoskeleton should have a high power-to-weight ratio.
- Backdrivability: considering that the target users in this project are macaques which cannot explicitly communicate with the researchers during operations, backdrivability would allow the ease of subject-induced motion when the device is unpowered or reaching to a posture that is not safe or comfortable to the subject.
- Safe and comfortable: the exoskeleton should be designed safe and comfortable for the subject. Safety needs to be guaranteed on both hardware level and software level.

The hardware design of an exoskeleton consists of the kinematic structural design and the actuation system design. The kinematic structural design will mainly follow the passive

exoskeleton proposed in Chapter 3, and the motion actuation of each joint will be provided by the series elastic actuators proposed in Chapter 4.

Guided by the above mentioned design requirements, the development of an actuated multi-DOF upper limb exoskeleton for macaques will be presented in this chapter. Compared with the non-human primate exoskeleton KINARM, the proposed exoskeleton allows for freedom of task space movement in additional dimensions. The mechanical design will be discussed in terms of kinematic structural design and actuation system development. Finally the system integration of the BMI with a macaque subject will be introduced, and pilot animal test results will be provided to support the effectiveness of the proposed exoskeleton system.

5.2 Mechanical Design

5.2.1 Kinematic Structural Design

The kinematic structural design mainly follows the passive exoskeleton design proposed in Chapter 3, the feasibility of which has been demonstrated by animal tests. Three DOFs are assigned at the shoulder complex for the actuated exoskeleton corresponding to the shoulder's horizontal rotation, flexion/extension, and internal/external rotation motion. Together with one DOF for the elbow's flexion/extension and one DOF for the forearm's internal/external rotation, the actuated exoskeleton has a total of five DOFs. Fig. 5.1 shows the hardware design of the proposed actuated upper limb exoskeleton.

Compared with the passive exoskeleton proposed in Chapter 3 which has four DOFs at the shoulder complex, no joint is dedicatedly designed to execute the shoulder's abduction/adduction motion in the actuated exoskeleton design, and the shoulder's abduction /adduction motion needs to be realized by the combined motion of Joint 1 and Joint 2. This is because the BMI study task for the macaque has been finalized to be mainly in front of its coronal plane which is similar to the reach-grasp-feed task in Chapter 3, and it can be noticed from Fig. 3.9 and Table 3.3 that the shoulder's abduction/adduction motion (corresponding to the second DOF in Fig. 3.9 and Table 3.3) is not obvious in this kind of tasks. For simplicity of mechanical design and control algorithm implementation, the shoulder joint is designed to be of three DOFs. In this case, the kinematic singularity of the shoulder joint occurs when the axis of Joint 1 aligns with the axis of Joint 3, which corresponds to the situation in which the upper arm rests pointing downward and perpendicular to the ground. However, this cannot actually happen due to the space constraint of the primate chair on which the macaque sits to perform the BMI task (see Section 5.3 for more details). Thus it is considered that the proposed shoulder joint design of the actuated exoskeleton is singularity-free in its workspace.

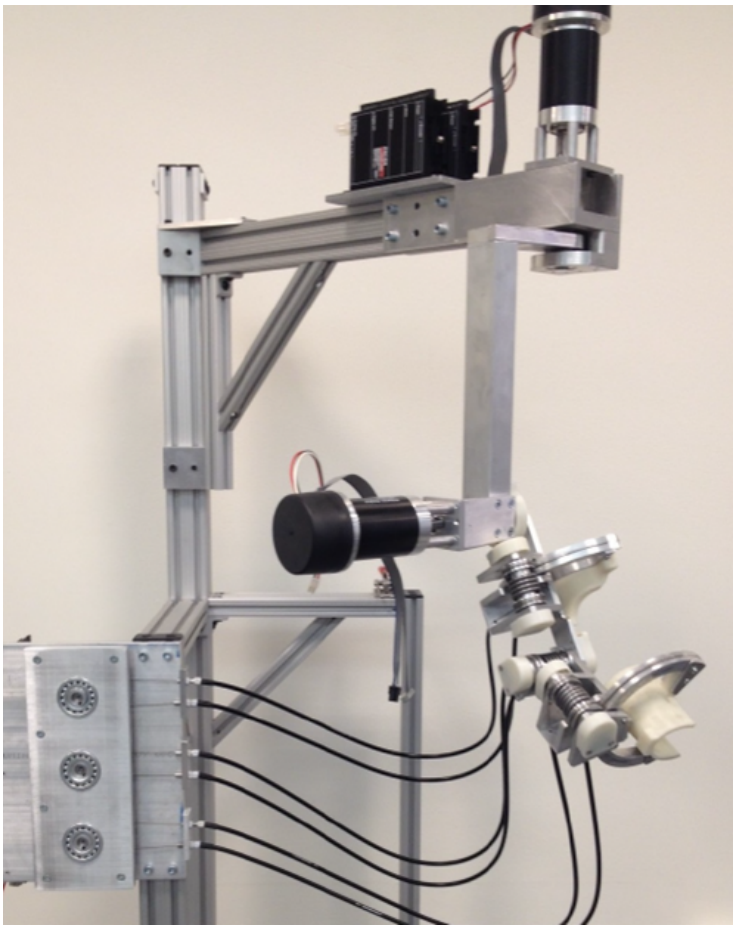

Figure 5.1: The proposed actuated upper limb exoskeleton for rhesus macaques.

5.2.2 Actuation System Design

Per the discussions of the design and control of a cable-driven SEA in Chapter 4, the proposed cable-driven SEA satisfies the requirements of high power-to-weight ratio, backdrivable, safe and comfortable motion actuation. In this section, in order to provide sufficient output force and velocity, the selections of geared motors, torsional springs and power transmissions will be discussed based on the kinematic and dynamic characteristics of each macaque upper limb joints.

Selection of Geared Motors

DC motors will be used to provide the actuation to the system, and should be selected based on the characteristics of the macaque's motion, among which joint torque and speed are the major factors. Table 5.1 shows the kinematic and dynamic characteristics of the macaque's upper limb. Measuring the joint torques of an animal is complicated and time-consuming,

Table 5.1: Kinematic and dynamic characteristics of macaque's upper limb.

	Shoulder	Elbow
Peak muscle torque[a] (N·m)	15.7	9.4
Maximum speed in BMI tasks[b] (rad/sec)	2.1	3.8

[a] data from [23].
[b] data from animal tests in Section 3.5.

Table 5.2: Physical information of BMI macaques.

		Body	Length (cm)			Circumference (cm)	
Subjects	Sex	weight (kg)	Upper arm	Forearm[a]	Hand	Upper arm	Forearm
Macaque G	M	10	14.5	15.2	6	23.2	16.2
Macaque J	M	13.3	13.7	16.2	9	24.5	18.0
Macaque W	M	10.5	14.2	16.3	9	23.5	17.1
Human	-	-	37.4[b]	48.8[b]	-	31.8[c]	24.2[c]

[a] from elbow to hand.
[b] average of male and female data from [29].
[c] data from [77].

thus the peak muscle torques obtained from existing literature are used. The maximum joint speeds were measured during the reach-grasp-feed animal tests in Section 3.5.

Generally joint torques at high speed should be relatively small. Thus, a maximum muscle torque of 15N·m at a maximum speed of 2rad/s is assumed for the shoulder joint, which results in a maximum power of 30W. Similarly, a typical muscle torque of 4N·m at a maximum speed of 3.5rad/s is assumed for the elbow joint, which results in a maximum power of 15W. A 30% power transmission efficiency is assumed for both the shoulder and the elbow joint considering the efficiency of the motor (70%), the gearbox (70%) and the transmission efficiency of other motion transmission mechanisms (for example, assumed to be 60% due to friction loss for a cable transmission). Thus the rated motor power should be approximately 100W for the shoulder joint and 50W for the elbow joint, respectively. Table 5.2 shows the physical information of the three macaques we have for the BMI studies, and based on these data, the estimated body segment mass and inertia of the BMI macaques are listed in Table 5.3 using the approach proposed in [13]. Table 5.4 shows the estimated mass of each mechanical link of the actuated exoskeleton. Taking the mass and inertia which also need to be compensated by the motors into consideration, the selected motors and gear reduction ratios of each joint are presented in Table 5.5. Note that the nominal torques, stall torques, and nominal speeds are calculated after the gear reduction. It can be noticed that the selected hardware can provide sufficient power for the exoskeleton actuation.

Table 5.3: Estimated body segment mass and inertia of the BMI macaques.

	Upper arm	Forearm + Hand
Segment mass (g)	410.57 ± 61.17	336.92 ± 448.2
Inertia about center of gravity (g·cm^2)	$(4.98 \pm 0.45) \times 10^3$	$(1.21 \pm 0.15) \times 10^4$
Inertia about proximal joint center (g·cm^2)	$(2.54 \pm 0.23) \times 10^4$	$(3.52 \pm 0.47) \times 10^4$

Table 5.4: Estimated mass of mechanical links.

Link	1	2	3	4	5
Mass (kg)	1.8	0.4	0.4	0.3	0.2

Table 5.5: Design of each joint for the actuated exoskeleton.

Joint	Motion	Motor	Reduction	Nominal torque (N·m)	Stall torque (N·m)	Nominal speed (rad/sec)	Power transmission
1	Shoulder horizontal rotation	Maxon EC60 Flat	91 : 1	20.7	380	4.4	Collocated
2	Shoulder flexion/extension	Maxon EC60 Flat	91 : 1	20.7	380	4.4	Collocated
3	Shoulder internal/external rotation	Maxon EC45 Flat	143 : 1	11.9	112	3.8	Non-collocated
4	Elbow flexion/extension	Maxon EC60 Flat	91 : 1	20.7	380	4.4	Non-collocated
5	Forearm internal/external rotation	Maxon EC45 Flat	125 : 1	10.4	98	4.4	Non-collocated

Selection of Torsional Springs

The elastic element plays an important role in the SEA design. On one hand, it introduces compliance in the actuation mechanism, which can accommodate the low intrinsic stiffness of the subject body and thus ensure the safety during the subject-robot interaction; on the other hand, it serves as a torque sensor which can save the space and cost of a dedicated one. The considerations on interaction safety and torque resolution require a more compliant elastic component in the SEA. However, compliant elasticity in the elastic component cannot provide sufficiently large output force/torque, and also may reduce the large force bandwidth of the SEA [71]. Therefore, a balance should be made among all these factors. So far a heuristic way of selecting the elasticity of the elastic component for an SEA is utilized with tests of springs with different stiffness.

Thus, a collection of torsional springs with the stiffness of 3.49, 7.61, 8.82, 16.43 and 27.03N·m/rad was examined, and in the end we chose the stiffness of 8.82N·m/rad such that the linearity of the torsional springs can be maintained at a high level within their feasible working ranges.

Selection of Power Transmission

Most SEAs impose the motor on the subject body [38, 39, 70, 75], which will increase the inertia of the overall system and also reduce the system compactness on the subject side. A comparison of the macaque upper limb dimensions and those of humans is shown in Table 5.2, which suggests that the space around the macaque upper limb is quite limited. As a result, the mechanical components of the exoskeleton should be kept sufficiently compact, and some complex designs good for adult humans may not be applicable to the exoskeleton for macaques. To achieve a lightweight and compact design, [84] proposes a Bowden cable-driven SEA which is able to avoid attaching the motors on the subject body. In this case, the geared motor can be installed on a fixed base and the driving force is transmitted through the cable to the actuator's load side. Thus the three distal joints of the exoskeleton (i.e., Joint 3, Joint 4 and Joint 5) are designed to be cable-driven by SEAs. Considering that the first two joints can be supported by the frame of the exoskeleton, these two proximal joints are designed to be collocated with conventional SEAs, as shown in Fig. 5.1.

5.3 System Integration

5.3.1 Overview of the Integrated BMI System

Fig. 5.2 shows a rendering of the designed 3D BMI task with a macaque subject. The macaque is seated in a primate chair with its collar and torso constrained, and the proposed actuated upper limb exoskeleton is attached to the macaque's right upper limb. By decoding the monkey's neural signal, the exoskeleton realizes the task of using the end point of the bar extend from the exoskeleton to touch the target plate positioned by the 3D presenting

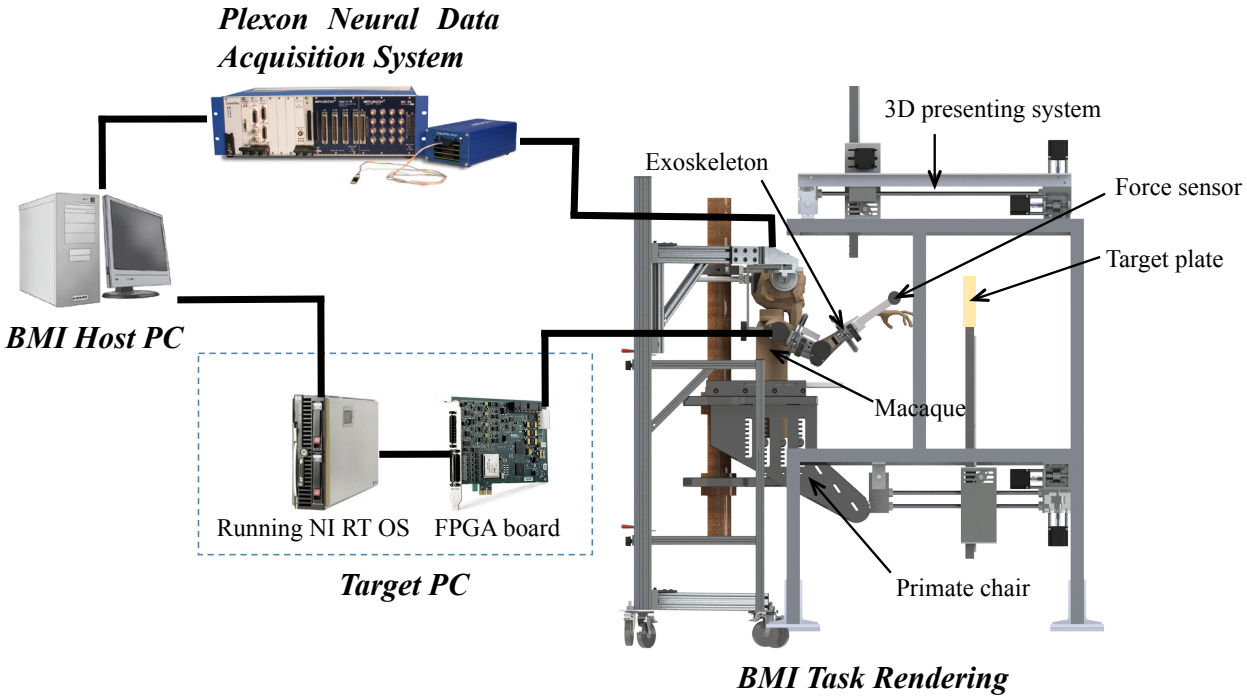

Figure 5.2: Overview of the designed 3D BMI task with a macaque subject.

system. One force sensor is installed on the tip of the bar indicating whether the task has been completed in one trial. Specifically, the Plexon neural data acquisition system collects the neural spikes measured by the electrodes that are implanted on the macaque's motor cortex, and sends the neural data to the BMI host PC. The host PC runs the neural decoder which translates the brain signal into the upper limb motion, and sends the decoded motion commands to the target PC. The control algorithms are implemented in the target PC to realize the decoded upper limb motion.

5.3.2 Control System Architecture

Compared with conventional neural decoders for the 2D task space motion decoding, neural control of a redundant kinematic chain has been investigated by Gowda in [22], which enables motion decoding in the joint space. In this work, it is assumed that the decoded joint space trajectory can be provided by the neural decoder, and the exoskeleton will enforce the corresponding motion. Considering that the system dynamics become highly complicated when the macaque is in the loop, and that modeling of the higher order dynamics inherent in a multi-DOF series elastic robot is difficult [62], a decentralized control approach can be used by regarding each joint as an independent system. The decentralized control approach is also feasible because the motion speed in a BMI task is generally low, and thus the coupling effects between joints due to varying configurations during motion is not obvious. In this case, the

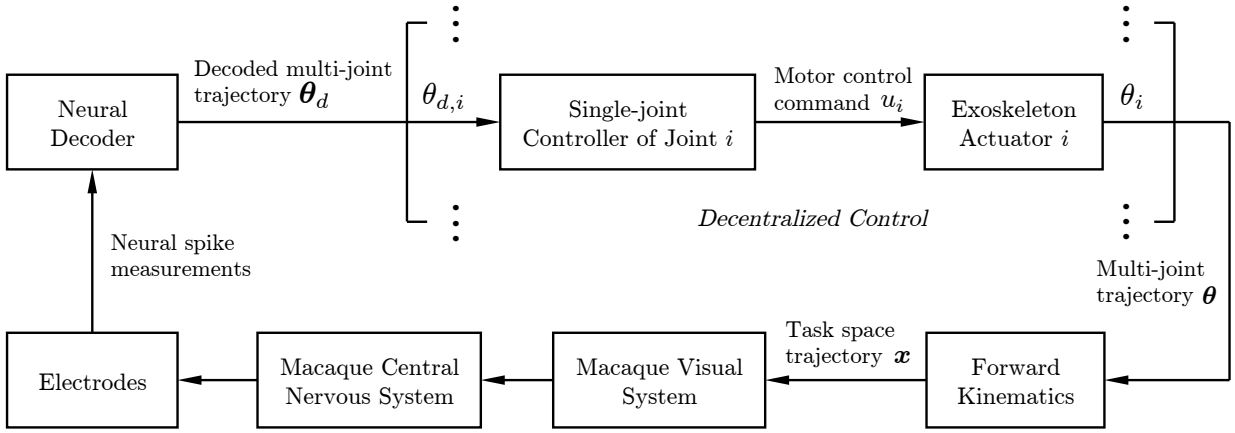

Figure 5.3: Block diagram of the integrated BMI system.

decoded joint space trajectory will be allocated to a set of single-joint controllers each of which uses a single-input single-output control algorithm to realize the joint-level trajectory, as shown in Fig. 5.3. Then the single-joint impedance control architecture proposed in Chapter 4 can be utilized to achieve the joint-level control goal. A detailed block diagram of such controller is presented in Fig. 5.4.

5.4 Experimental Results of Animal Test

Animal tests were conducted operating the actuated exoskeleton to complete the reach and touch task with one able-bodied adult male rhesus macaque in the loop. All procedures were conducted in compliance with the National Institute of Health Guide for Care and Use of Laboratory Animals and were approved by the University of California, Berkeley Institutional Animal Care and Use Committee.

At the animal training stage, the exoskeleton will be first computer controlled to realize a designed joint space trajectory (rather than commanded by a neural decoder), then gradually will be operated in a shared control manner between a computer and a neural decoder, and finally will be only controlled by a neural decoder. At the initial phase, considering the complexity of the joint space neural decoder development, only the first four joints were actuated leaving the forearm's internal/external motion being fixed. Fig. 5.5 shows the joint space trajectory of the subject side positions in one trial of computer controlled reach and touch task. The macaque has been well trained and no obvious resisting motion was applied to the exoskeleton by the macaque. The corresponding task space trajectory is illustrated in Fig. 5.6, which matched the actual motion well and supported the effectiveness of the proposed actuated exoskeleton system.

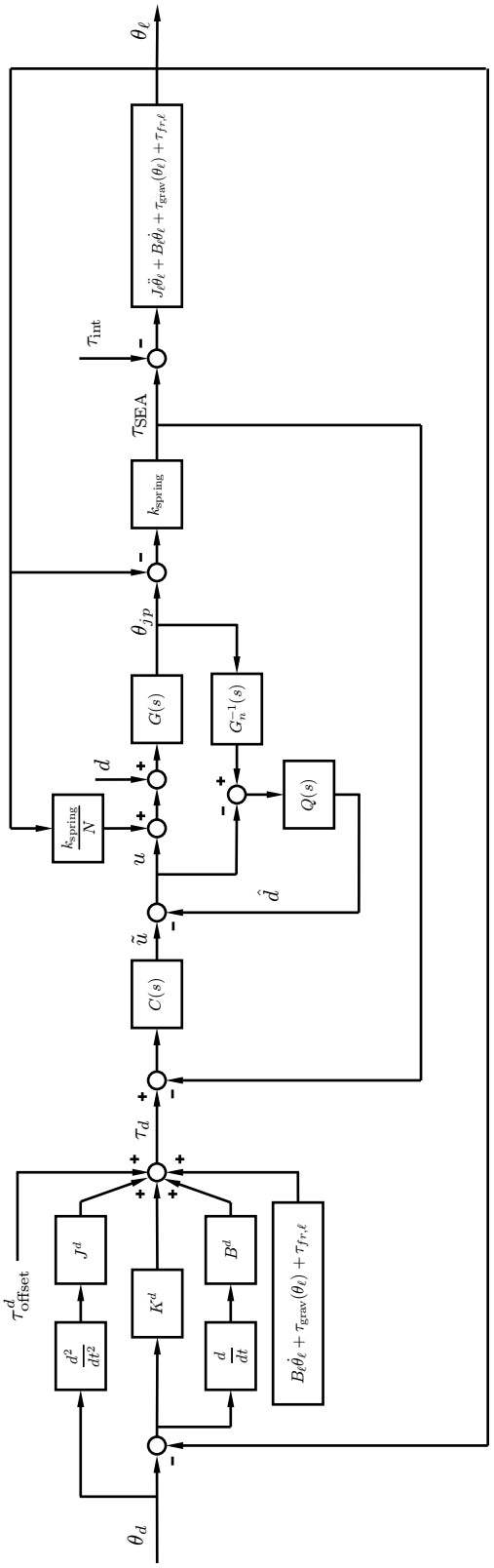

Figure 5.4: Single-joint control system proposed in Chapter 4.

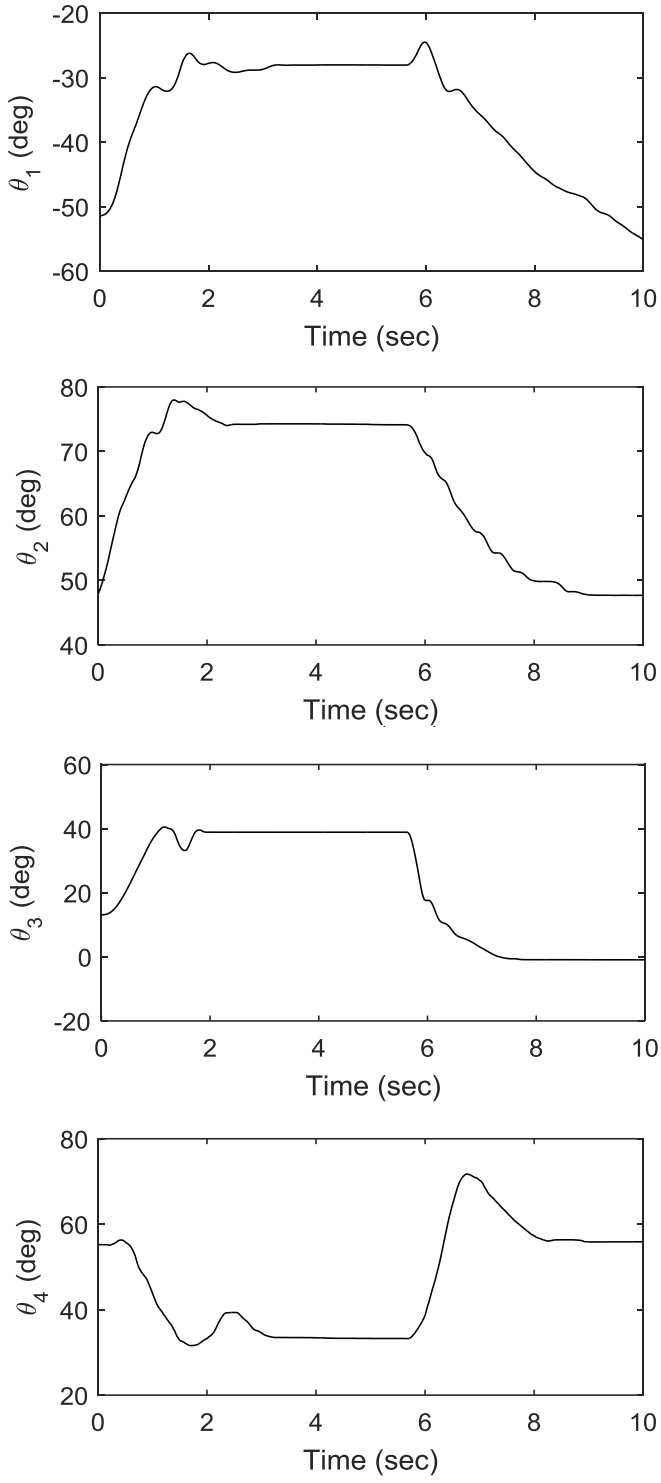

Figure 5.5: Joint space trajectories of one trial.

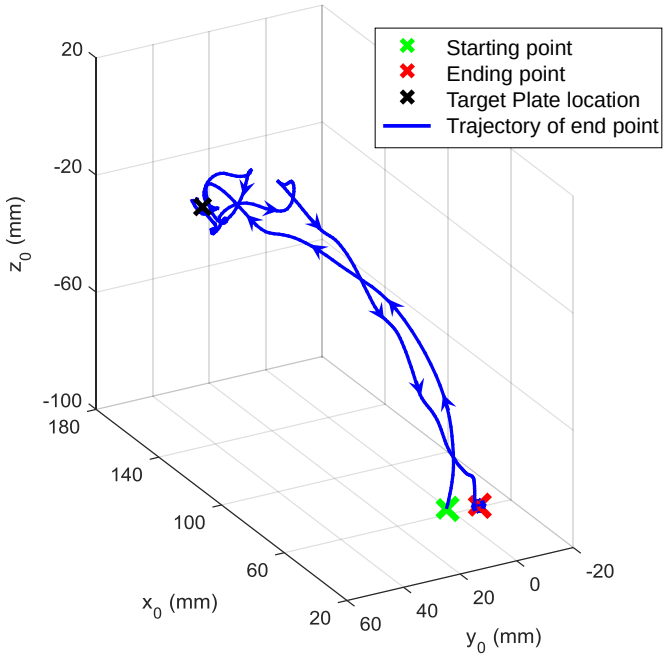

Figure 5.6: Task space trajectory of the exoskeleton distal end point at which the force sensor was attached. The macaque's right arm initially rested on the primate table, and then was driven by the exoskeleton to let the distal end point touch the target plate. Once the force sensor detected the touching, the exoskeleton paused at the current posture for a while. Finally the macaque's arm was driven to recover to the initial posture. The origin of the coordinate system O_0–$x_0y_0z_0$ locates at the macaque shoulder center, and z_0-axis points upright and x_0-axis points the front direction of the macaque.

5.5 Chapter Summary

In this chapter, the development of an actuated upper limb exoskeleton for rhesus macaques was presented in terms of design requirements, mechanical design, and system integration. In the aspect of mechanical design, the kinematic structure of the actuated exoskeleton mainly followed the passive exoskeleton design proposed in Chapter 3; and the drivetrain selections were based on the kinematic upper limb motion data by the passive exoskeleton. System integration was presented by combining the neural interface, the neural decoder, and the exoskeleton together. A decentralized control architecture was then introduced, and the single-joint impedance control algorithm proposed in Chapter 4 can be utilized to achieve the joint-level control goal. Finally the effectiveness of the proposed actuated exoskeleton was supported by pilot animal test results.

Chapter 6

Concluding Remarks and Open Issues

6.1 Concluding Remarks

This dissertation investigates the mechatronic considerations of developing an upper limb exoskeleton for rhesus macaques, including two major aspects: 1) the kinematic modeling and structural design, and 2) the actuator design and control. The contributions of this dissertation are summarized as follows:

A Kinematic Upper Limb Exoskeleton Model with a Redundant Shoulder Joint Design for Rhesus Macaques

Based on the analysis of the primate upper limb anatomical structure, a 6-DOF upper limb exoskeleton model for rhesus macaques was first proposed in this dissertation. Four DOFs were assigned at the shoulder complex to achieve more flexible manipulation of the mechanism. The kinematic characteristics of the proposed redundant shoulder model were quantitatively investigated based on the manipulability metric comparison with three other types of designs. The results showed that the proposed shoulder joint model had the ability to avoid entering the system's singular configuration by appropriately planning the joint space trajectories. And the gradient projection method based kinematic control could be utilized for the redundant shoulder joint trajectory planning. Simulation results demonstrated the feasibility of the proposed approach. This work was published in [46].

A Passive Upper Limb Exoskeleton for Motion Characterization and Animal Training

A passive upper limb exoskeleton with position sensors was fabricated following the proposed kinematic model, which aimed at serving as a motion sensing device and a safe pilot facility for animal training prior to the development of an actuated exoskeleton system. A two millimeter position sensing accuracy of the end point was achieved by the motion capture system based kinematic calibration, which was sufficient for the neurophysiology applica-

tions. Finally the animal tests were conducted in the scenario of a reach-grasp-feed task. The effectiveness of the proposed exoskeleton system was demonstrated by both joint space measurements and task space trajectory visualization. The collected kinematic motion data from each macaque upper limb joint was then used to provide guidance for the actuation system design of the actuated exoskeleton. This work was published in [48, 50].

A Cable-Driven Series Elastic Actuator for Compliant Motion Actuation

In order to obtain a compact, powerful, backdrivable and torque-reflecting actuator for the exoskeleton motion actuation, a cable-driven series elastic actuator (SEA) was proposed, and the torque based interactive impedance control algorithm was developed to enhance safe actuation. Torque-mode control is fundamental to an SEA. A big challenge to achieve high fidelity torque control of a cable-driven SEA is to suppress the friction disturbance introduced by the cable-driven transmission. A disturbance observer based torque controller was proposed and successfully rejected the friction at the motor side and on the cable transmission simultaneously. Compared with conventional approach, the proposed algorithm significantly improved torque tracking performance and exhibited large system bandwidth. Then an outer loop interactive impedance controller was designed to regulate the interaction torque between the actuator's load side and the subject. Compared with the conventional proportional-derivative form impedance controller, the proposed approach has the advantage of being able to directly characterize the impedance behavior between the interaction torque and the load side motion. The proposed impedance control architecture is also applicable to the non-cable-driven scenarios. Besides, under different conditions, the impedance controller will reduce to a position controller or a torque controller. Specifically, the impedance controller becomes a position controller when there is no interaction between the robot and the environment, and becomes a torque controller when the virtual impedance parameters are all zeros. The effectiveness of the proposed control algorithm was verified by a series of experiments with and without the interaction with a subject. This work has been reported in [49, 47].

An Actuated Upper Limb Exoskeleton for a Brain-Machine Interface with Rhesus Macaque Subjects

On top of the development of the passive exoskeleton and the impedance-controlled actuator, an actuated multi-degree of freedom upper limb exoskeleton was finally developed and integrated with a brain-machine interface for macaques. In the aspect of mechanical design, the kinematic structure of the actuated exoskeleton mainly followed the proposed passive exoskeleton design, and the actuator specifications were selected based on the macaque kinematic motion data collected by the passive exoskeleton. System integration was then presented by combining the neural interface, the neural decoder, and the exoskeleton together. A decentralized control architecture was then introduced, and the proposed single-joint impedance control algorithm can be utilized to achieve the joint-level control goal.

Finally the effectiveness of the proposed actuated exoskeleton was supported by pilot animal test results.

6.2 Open Issues

Although a number of aspects on the development of an upper limb exoskeleton for rhesus macaques have been discussed in this dissertation, there are still many issues left open for further investigation:

Modeling of the Rhesus Macaque Upper Limb

In order to achieve an exoskeleton design which can well match the macaque upper limb motion, an accurate model of the macaque upper limb is first needed. Since the upper limb anatomy of rhesus macaques is not identical with that of humans, the existing studies on human upper limbs cannot provide comprehensive information for the macaque upper limb exoskeleton development. However, the macaque upper limb anatomy are not as widely studied as that of human's. Thus the modeling of the macaque upper limb needs to be further investigated, especially the upper limb morphology, the shoulder complex anatomy, and the angle between the upper arm and the forearm when the elbow is fully extended.

Criterion of Virtual Impedance Parameter Selection

In this dissertation, the criterion of the virtual impedance parameter selection is not fully discussed. To the author's best knowledge, there is also no existing literature working on the virtual impedance parameter selection for an impedance-controlled exoskeleton system. However, these parameters should be carefully determined according to the user's haptic sensation as well as different applications. For the exoskeleton systems, generally it can be considered that the user's limb motion is the same as the exoskeleton's load side. In this case oscillation may cause discomfort to the user and thus the transient motion should be well-damped. One big challenge is that the user's body dynamics are hard to model, which makes it difficult to propose a systematic way to design the virtual impedance parameters.

Integration of Force Sensors at the Points of Interaction

For the sake of reducing the development cost and design complexity, no dedicated force sensor is installed at the points of interaction between the proposed exoskeleton and the user body segments. The only force/torque feedbacks are the joint torques estimated from the SEAs by its deflection angles and the spring stiffness. One problem is that the performance of the impedance controller is limited due to the lack of force feedback from the interaction points, and the integration of force sensors at the points of interaction helps enforce the interaction force to a more general forms of virtual impedance with higher accuracy. One challenge is that mounting force sensors to the appropriate places on an exoskeleton is

difficult, and the mechanical design complexity will also be increased. Besides, the torque measurements from the SEAs should be consistent with the measurements from the force sensor, which requires the elastic element of the SEAs to have high linearity.

Stability of the User-In-the-Loop System in Presence of Time Delay

In the integrated BMI system with the user wearing the exoskeleton in the loop, the position commands to the exoskeleton are decoded from the user's neural signal. Generally decoding the neural signal into the body segment motions takes some computation time, and data transmitting between the neural decoder and the exoskeleton controller also takes some time. Thus there will be time delay between the received motion commands by the exoskeleton and the user's actual thoughts which is based on user's instant visual feedback. If the time delay is significant, it is highly possible that the exoskeleton's motion cannot follow the user's mind, and in turn the subject tends to adjust its intention. For applications in which the subject still some residual mobility, the exoskeleton's motion may conflict with the user's own motion intension, which could cause the coupled user-exoskeleton system to be "unstable". This issue needs to be further investigated to help the user better learn how to use an exoskeleton device, and realize safe and comfortable motion actuation.

Bibliography

[1] Friedhelm Altpeter. "Friction modeling, identification and compensation". PhD thesis. Lausanne, Switzerland: Ecole Polytechnique Federale de Lausanne, 1999.

[2] Brian Armstrong-Helouvry, Pierre Dupont, and Carlos Canudas de Wit. "A survey of models, analysis tools and compensation methods for the control of machines with friction". In: *Automatica* 30.7 (1994), pp. 1083–1138.

[3] S. Balasubramanian et al. "RUPERT: An exoskeleton robot for assisting rehabilitation of arm functions". In: *Virtual Rehabilitation, 2008*. 2008, pp. 163–167.

[4] S. Ball, I. Brown, and S. Scott. "MEDARM: a rehabilitation robot with 5DOF at the shoulder complex". In: *Proc. IEEE/ASME Int. Conf. on Advanced Intelligent Mechatronics (AIM)*. 2007, pp. 1–6.

[5] B. E. Bishop and M. W. Spong. "Control of Redundant Manipulators Using Logic-Based Switching". In: *Proc. The 37th IEEE Conference on Decision and Control (CDC)*. Vol. 2. 1998, pp. 1488–1493.

[6] A. Calanca, R. Muradore, and P. Fiorini. "A Review of Algorithms for Compliant Control of Stiff and Fixed-Compliance Robots". In: *IEEE/ASME Trans. Mechatronics* PP.99 (2015), pp. 1–1.

[7] D.G. Caldwell, C. Favede, and N. Tsagarakis. "Dextrous exploration of a virtual world for improved prototyping". In: *Proc. IEEE Int. Conf. on Robotics and Automation (ICRA)*. Vol. 1. 1998, 298–303 vol.1.

[8] C. Carignan, J. Tang, and S. Roderick. "Development of an exoskeleton haptic interface for virtual task training". In: *Intelligent Robots and Systems, 2009. IROS 2009. IEEE/RSJ International Conference on*. 2009, pp. 3697–3702.

[9] Craig Carignan, Michael Liszka, and Stephen Roderick. "Design of an Arm Exoskeleton with Scapula Motion for Shoulder Rehabilitation". In: *Proc. of Int. Conf. on Advanced Robotics (ICAR)*. 2005.

[10] Jose M. Carmena. "Advances in Neuroprosthetic Learning and Control". In: *PLoS Biol* 11.5 (May 2013), e1001561.

[11] Sherwin S. Chan and Daniel W. Moran. "Computational model of a primate arm: from hand position to joint angles, joint torques and muscle forces". In: *J. Neural Eng.* 3.4 (2006), pp. 327–337.

[12] Wenjie Chen, Kyoungchul Kong, and M. Tomizuka. "Dual-Stage Adaptive Friction Compensation for Precise Load Side Position Tracking of Indirect Drive Mechanisms". In: *IEEE Trans. Control Syst. Technol.* 23.1 (2015), pp. 164–175.

[13] Ernest J. Cheng and Stephen H. Scott. "Morphometry of macaca mulatta forelimb. I. Shoulder and elbow muscles and segment inertial parameters". In: *J. Morphol.* 245.3 (2000), pp. 206–224.

[14] Marianne I. Christel and Aude Billard. "Comparison between macaques' and humans' kinematics of prehension: the role of morphological differences and control mechanisms". In: *Behav. Brain Res.* 131.1-2 (2002), pp. 169–184.

[15] Bryan Christie. Image used courtesy of Bryan Christie. From *How to Control a Prosthesis With Your Mind, IEEE Spectrum*. March, 2012.

[16] H. P. Van Cott and R. G. Kinkade. *Human Engineering Guide to Equipment Design*. Revised. Washington D. C., U.S.A.: McGraw-Hill, 1972.

[17] Peter Donelan. "Kinematic Singularities of Robot Manipulators". In: *Advances in Robot Manipulators*. Ed. by Ernest Hall. InTech, 2010. Chap. 20.

[18] Mehmet Alper Ergin and Volkan Patoglu. "ASSISTON-SE: A self-aligning shoulder-elbow exoskeleton". In: *Proc. IEEE Int. Conf. on Robotics and Automation (ICRA)*. 2012, pp. 2479–2485.

[19] Vikash Gilja et al. "A high-performance neural prosthesis enabled by control algorithm design". In: *Nat Neurosci* 15.12 (Dec. 2012), pp. 1752–1757. URL: `http://dx.doi.org/10.1038/nn.3265`.

[20] R. A. R. C. Gopura and K. Kiguchi. "Development of a 6DOF Exoskeleton Robot for Human Upper-Limb Motion Assist". In: *Information and Automation for Sustainability, 2008. ICIAFS 2008. 4th International Conference on*. 2008, pp. 13–18.

[21] R. A. R. C. Gopura and Kazuo Kiguchi. "Mechanical designs of active upper-limb exoskeleton robots: State-of-the-art and design difficulties". In: *IEEE Int. Conf. on Rehabilitation Robotics*. 2009, pp. 178–187.

[22] Suraj Raju Gowda. "Design of control algorithms for redundant neuroprosthetic brain-machine interfaces". PhD thesis. Berkeley, U.S.A.: University of California, Berkeley, 2015.

[23] Kirsten M. Graham and Stephen H. Scott. "Morphometry of macaca mulatta forelimb. III. moment arm of shoulder and elbow muscles". In: *J. Morphol.* 255.3 (2003), pp. 301–314. ISSN: 1097-4687. DOI: `10.1002/jmor.10064`.

[24] A. Gupta and M. K. O'Malley. "Design of a haptic arm exoskeleton for training and rehabilitation". In: *IEEE/ASME Transactions on Mechatronics* 11.3 (2006), pp. 280–289.

[25] K. Haninger, J. Lu, and M. Tomizuka. "Motion control of series-elastic actuator". In: *American Control Conference (accepted)*. 2016.

[26] Leigh R. Hochberg et al. "Reach and grasp by people with tetraplegia using a neurally controlled robotic arm". In: *Nature* 485 (2012), pp. 372–375.

[27] N. Hogan. "Stable execution of contact tasks using impedance control". In: *Proc. 1987 IEEE Int. Conf. Robotics Autom.* Vol. 4. 1987, pp. 1047–1054. DOI: 10.1109/ROBOT.1987.1087854.

[28] Neville Hogan. "Impedance control: an approach to manipulation: Part II-Implementation". In: *ASME J. Dyn. Sys., Meas., Control* 107.1 (1985), pp. 8–16.

[29] Ronald Huston. *Principles of Biomechanics*. Ed. by L. L. Faulkner. Taylor & Francis CRC Press, 2009.

[30] Image used courtesy of BKIN Technologies. URL: http://www.bkintechnologies.com/.

[31] Image used courtesy of Dan Vergano from National Geographic. URL: http://www.nationalgeographic.com/.

[32] Image used courtesy of Medical Multimedia Group LLC. URL: http://www.eorthopod.com/.

[33] G. Johnson et al. "The design of a five-degree-of-freedom powered orthosis for the upper limb". In: *Proc Inst Mech Eng H.* Vol. 215. 3. 2001, pp. 275–284.

[34] M. Kaneko, T. Yamashita, and K. Tanie. "Basic considerations on transmission characteristics for tendon drive robots". In: *Proc. 5th Int. Conf. Adv. Robotics (ICAR).* Vol. 1. 1991, pp. 827–832. DOI: 10.1109/ICAR.1991.240572.

[35] C.J. Kempf and S. Kobayashi. "Disturbance observer and feedforward design for a high-speed direct-drive positioning table". In: *IEEE Trans. Control Syst. Technol.* 7.5 (1999), pp. 513–526. ISSN: 1063-6536. DOI: 10.1109/87.784416.

[36] Jin-Oh Kim and Pradeep K. Khosla. "Dexterity measures for design and control of manipulators". In: *Proc. IEEE/RSJ Int. Workshop on Intelligent Robots and Systems (IROS).* Vol. 2. 1991, pp. 758–763.

[37] H. Kobayashi and K. Hiramatsu. "Development of muscle suit for upper limb". In: *Robotics and Automation, 2004. Proceedings. ICRA '04. 2004 IEEE International Conference on.* Vol. 3. 2004, pp. 2480–2485.

[38] Kyoungchul Kong, Joonbum Bae, and Masayoshi Tomizuka. "A Compact Rotary Series Elastic Actuator for Human Assistive Systems". In: *IEEE/ASME Trans. Mechatronics* 17.2 (2012), pp. 288–297. ISSN: 1083-4435. DOI: 10.1109/TMECH.2010.2100046.

[39] Kyoungchul Kong, Joonbum Bae, and Masayoshi Tomizuka. "Control of Rotary Series Elastic Actuator for Ideal Force-Mode Actuation in Human-Robot Interaction Applications". In: *IEEE/ASME Trans. Mechatronics* 14.1 (2009), pp. 105–118. ISSN: 1083-4435. DOI: 10.1109/TMECH.2008.2004561.

[40] Kyoungchul Kong, Joonbum Bae, and Masayoshi Tomizuka. "Torque Mode Control of a Cable-Driven Actuating System by Sensor Fusion". In: *ASME J. Dyn. Sys., Meas., Control* 135.3 (2013), pp. 031003–1 –031003–7.

[41] Donghan Koo et al. "Shoulder mechanism design of an exoskeleton robot for stroke patient rehabilitation". In: *Proc. IEEE Int. Conf. on Rehabilitation Robotics*. 2011, pp. 1–6.

[42] Hermano I. Krebs et al. "Rehabilitation robotics: pilot trial of a spatial extension for MIT-Manus". In: *J Neuroengineering Rehabil* 1.5 (2004).

[43] Ho Seong Lee and M. Tomizuka. "Robust motion controller design for high-accuracy positioning systems". In: *IEEE Trans. Ind. Electron.* 43.1 (1996), pp. 48–55. ISSN: 0278-0046. DOI: 10.1109/41.481407.

[44] J. Lenarcic and M. Stanisic. "A humanoid shoulder complex and the humeral pointing kinematics". In: *Robotics and Automation, IEEE Transactions on* 19.3 (2003), pp. 499–506. ISSN: 1042-296X. DOI: 10.1109/TRA.2003.810578.

[45] P. Letier et al. "SAM: A 7-DOF portable arm exoskeleton with local joint control". In: *Proc. IEEE/RSJ Int. Conf. on Intelligent Robots and Systems (IROS)*. 2008.

[46] Junkai Lu, Wenjie Chen, and Masayoshi Tomizuka. "Kinematic Design and Analysis of a 6-DOF Upper Limb Exoskeleton Model for a Brain-Machine Interface Study". In: *Proc. 6th IFAC Symposium on Mechatronic Systems*. 2013, pp. 293–300.

[47] Junkai Lu, Kevin Haninger, and Masayoshi Tomizuka. "Interactive Impedance Control of a Cable-Driven Series Elastic Actuator for Human-Robot Interaction". In: *IEEE/ASME Trans. Mechatronics* (under review).

[48] Junkai Lu et al. "A passive upper limb exoskeleton for macaques in a BMI study – kinematic design, analysis, and calibration". In: *Proc. ASME Dyn. Syst. Control Conf. (DSCC)*. 2014.

[49] Junkai Lu et al. "Design and torque-mode control of a cable-driven rotary series elastic actuator for subject-robot interaction". In: *2015 IEEE/ASME International Conference on Advanced Intelligent Mechatronics (AIM)*. 2015, pp. 158–164. DOI: 10.1109/AIM.2015.7222525.

[50] Junkai Lu et al. "Design of a Passive Upper Limb Exoskeleton for Macaque Monkeys". In: *ASME J. Dyn. Sys., Meas., Control* (2016).

[51] J. Y. S. Luh, M. W. Walker, and R. P. C. Paul. "Resolved-Acceleration Control of Mechanical Manipulators". In: *IEEE Trans. Automat. Contr.* AC-25.3 (1980), pp. 468–474.

[52] F. Martinez et al. "Design of a Five Actuated DoF Upper Limb Exoskeleton Oriented to Workplace Help". In: *Proc. IEEE/RAS-EMBS Int. Conf. on Biomedical Robotics and Biomechatronics*. 2008, pp. 169–174.

[53] MathWorks. *Optimization Toolbox*. 2012. URL: `http://www.mathworks.com/products/optimization/`.

[54] MathWorks. *System Identification Toolbox*. 2014. URL: `http://www.mathworks.com/products/sysid/`.

[55] Matjaz Mihelj, Tobias Nef, and Robert Riener. "ARMin - Toward a six DoF upper limb rehabilitation robot". In: *Proc. IEEE/RAS-EMBS Int. Conf. on Biomedical Robotics and Biomechatronics*. 2006, pp. 1154–1159.

[56] Matjaz Mihelj, Tobias Nef, and Robert Riener. "ARMin II - 7 DoF rehabilitation robot: mechanics and kinematics". In: *Proc. IEEE Int. Conf. on Robotics and Automation (ICRA)*. 2007, pp. 4120–4125.

[57] M. Mistry, P. Mohajerian, and S. Schaal. "An exoskeleton robot for human arm movement study". In: *Intelligent Robots and Systems, 2005. (IROS 2005). 2005 IEEE/RSJ International Conference on*. 2005, pp. 4071–4076.

[58] T. Nef, M. Guidali, and R. Riener. "ARMin III - arm therapy exoskeleton with an ergonomic shoulder actuation". In: *Applied Bionics and Biomechanics* 6.2 (2009), pp. 127–142.

[59] T. Nef and R. Riener. "Shoulder Actuation Mechanisms for Arm Rehabilitation Exoskeletons". In: *Proc. IEEE/RAS-EMBS Int. Conf. on Biomedical Robotics and Biomechatronics*. 2008, pp. 862–868.

[60] T. Nef et al. "ARMin - Exoskeleton for Arm Therapy in Stroke Patients". In: *Rehabilitation Robotics, 2007. ICORR 2007. IEEE 10th International Conference on*. 2007, pp. 68–74.

[61] K. Ohnishi, M. Shibata, and T. Murakami. "Motion control for advanced mechatronics". In: *IEEE/ASME Trans. Mechatronics* 1.1 (1996), pp. 56–67. ISSN: 1083-4435. DOI: `10.1109/3516.491410`.

[62] Nicholas Paine et al. "Actuator control for the NASA-JSC Valkyrie humanoid robot: a decoupled dynamics approach for torque control of series elastic robots". In: *Journal of Field Robotics* 32.3 (2015), pp. 378–396.

[63] Hyung-Soon Park, Yupeng Ren, and Li-Qun Zhang. "IntelliArm: An exoskeleton for diagnosis and treatment of patients with neurological impairments". In: *Proc. IEEE RAS & EMBS Int. Conf. on Biomedical Robotics and Biomechatronics*. 2008, pp. 109–114.

[64] Malcolm Peat. "Functional Anatomy of the Shoulder Complex". In: *Phys Ther* 66.12 (1986), pp. 1855–1865.

[65] J. Perry, J. Rosen, and S. Burns. "Upper-Limb Powered Exoskeleton Design". In: *IEEE/ASME Trans. Mechatronics* 12.4 (2007), pp. 408–417.

[66] Joel C. Perry, Janet M. Powell, and Jacob Rosen. "Isotropy of an upper limb exoskeleton and the kinematics and dynamics of the human arm". In: *Applied Bionics and Biomechanics* 6.2 (2009), pp. 175–191.

[67] PhaseSpace Inc. *The IMPULSE X2 Motion Capture System Catalog*. 2012. URL: `http://www.phasespace.com/products/ImpulseProductDoc.pdf`.

[68] G.A. Pratt et al. "Late motor processing in low-impedance robots: impedance control of series-elastic actuators". In: *Proc. 2004 Amer. Cont. Conf.* Vol. 4. 2004, pp. 3245–3251.

[69] Gill A. Pratt and Matthew M. Williamson. "Series elastic actuators". In: *Proc. IEEE/RSJ Int. Conf. Intell. Robots Syst. (IROS)*. Vol. 1. 1995, pp. 399–406. DOI: `10.1109/IROS.1995.525827`.

[70] D. Ragonesi et al. "Series elastic actuator control of a powered exoskeleton". In: *Proc. 33rd Annu. IEEE Int. Conf. on Eng. in Med. and Biol. Soc.* 2011, pp. 3515–3518.

[71] David William Robinson. "Design and Analysis of Series Elasticity in Closed-loop Actuator Force Control". PhD thesis. Cambridge, MA: Massachusetts Institute of Technology, 2000.

[72] Douglas P. Romilly et al. "A Functional Task Analysis and Motion Simulation for the Development of a Powered Upper-Limb Orthosis". In: *IEEE Trans. Rehabil. Eng.* 2.3 (1994), pp. 119–129.

[73] J. Rosen et al. "A myosignal-based powered exoskeleton system". In: *IEEE Transactions on Systems, Man, and Cybernetics - Part A: Systems and Humans* 31.3 (2001), pp. 210–222.

[74] R. J. Sanchez et al. "A pneumatic robot for re-training arm movement after stroke: rationale and mechanical design". In: *Rehabilitation Robotics, 2005. ICORR 2005. 9th International Conference on*. 2005, pp. 500–504.

[75] W.M. dos Santos, G.AP. Caurin, and AAG. Siqueira. "Torque control characterization of a rotary series elastic actuator for knee rehabilitation". In: *Proc. 16th Int. Conf. Adv. Robotics (ICAR)*. 2013, pp. 1–6. DOI: `10.1109/ICAR.2013.6766567`.

[76] Shankar Sastry. *Nonlinear Systems: Analysis, Stability, and Control*. New York, NY: Springer-Verlag, 1999.

[77] Kathleen Schell et al. "Clinical Comparison of Automatic, Noninvasive Measurements of Blood Pressure in the Forearm and Upper Arm". In: *Am. J. Crit. Care* 15.2 (2006), pp. 196–205.

[78] Stephen H. Scott. "Apparatus for measuring and perturbing shoulder and elbow joint positions and torques during reaching". In: *Journal of Neuroscience Methods* 89.2 (1999), pp. 119–127.

[79] Maryam M. Shanechi, Amy L. Orsborn, and Jose M. Carmena. "Robust Brain-Machine Interface Design Using Optimal Feedback Control Modeling and Adaptive Point Process Filtering". In: *PLoS Comput Biol* 12.4 (2016), e1004730. DOI: 10.1371/journal.pcbi.1004730. URL: http://dx.doi.org/10.1371%2Fjournal.pcbi.1004730.

[80] B. Siciliano et al. *Robotics: Modelling, Planning and Control*. 2nd. Springer, 2009.

[81] N.L. Tagliamonte, D. Accoto, and E. Guglielmelli. "Rendering viscoelasticity with Series Elastic Actuators using cascade control". In: *Proc. 2014 IEEE Int. Conf. Robotics Autom. (ICRA)*. 2014, pp. 2424–2429.

[82] Nikolaos G. Tsagarakis and Darwin G. Caldwell. "Development and Control of a 'Soft-Actuated' Exoskeleton for Use in Physiotherapy and Training". In: *Journal of Autonomous Robots* 15.1 (2003), pp. 21–33.

[83] Meel Velliste et al. "Cortical control of a prosthetic arm for self-feeding". In: *Nature* 453 (2008), pp. 1098–1101.

[84] J.F. Veneman et al. "A Series Elastic- and Bowden-Cable-Based Actuation System for Use as Torque Actuator in Exoskeleton-Type Robots". In: *Int. J. Robotics Research (IJRR)* 25.3 (2006), pp. 261–281.

[85] Eric T. Wolbrecht, David J. Reinkensmeyer, and James E. Bobrow. "Pneumatic Control of Robots for Rehabilitation". In: *Int. J. Robotics Research (IJRR)* 29.1 (2010), pp. 23–38.

[86] Ge Wu et al. "ISB recommendation on definitions of joint coordinate systems of various joints for the reporting of human joint motion - Part II: shoulder, elbow, wrist and hand". In: 38 (2005), pp. 981–992.

[87] J. Yang, K. Abdel-Malek, and K. Nebel. "Reach Envelope of a 9-Degree-of-Freedom Model of the Upper Extremity". In: *International Journal of Robotics & Automation* 20.4 (2005), pp. 240–259.

[88] T. Yoshikawa. "Manipulability of Robotic Mechanisms". In: *The International Journal of Robotics Research* 4.2 (1985), pp. 3–9.

[89] A. B. Zoss, H. Kazerooni, and A. Chu. "Biomechanical design of the Berkeley lower extremity exoskeleton (BLEEX)". In: *IEEE/ASME Transactions on Mechatronics* 11.2 (2006), pp. 128–138.